Observation of Excited B Mesons in $p\bar{p}$ Collisions at $\sqrt{s} = 1.8\,\textbf{TeV}$.

by

Dejan Vučinić

Submitted to the Department of Physics
in partial fulfillment of the requirements for the degree of

Doctor of Philosophy

at the

MASSACHUSETTS INSTITUTE OF TECHNOLOGY

February 1999

© Dejan Vučinić, MCMXCIX. All rights reserved.

Author . . . .
Department of Physics
September 30, 1998

Certified by . . . . . .
Paraskevas A. Sphicas
Professor
Thesis Supervisor

Accepted by . . . .
Thomas J. Greytak
Professor, Associate Department Head for Education
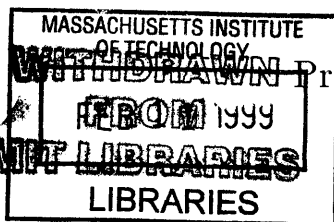
Observation of Excited B Mesons in $p\bar{p}$ Collisions at $\sqrt{s} = 1.8\,\mathrm{TeV}$.

by

Dejan Vučinić

Submitted to the Department of Physics
on September 30, 1998, in partial fulfillment of the
requirements for the degree of
Doctor of Philosophy

Abstract

Production of orbitally excited ($L = 1$) states of B mesons, B^{**}, is studied using a sample of nearly ten thousand partially reconstructed B mesons collected with the CDF detector from $p\bar{p}$ collisions at $\sqrt{s} = 1.8\,\mathrm{TeV}$. Ambiguities in the reconstruction of the B flavor and momentum are resolved. The fraction of b quarks that hadronize into an $L = 1$ state is measured to be $0.28 \pm 0.06(\mathrm{stat}) \pm 0.03(\mathrm{syst})$, and the collective mass of the B^{**} states is measured to be $\mathrm{m}(B_1) = 5.71 \pm 0.02\,\mathrm{GeV}/c^2$ given the mass splittings between the four states.

Thesis Supervisor: Paraskevas A. Sphicas
Title: Professor

Acknowledgments

On the path to this thesis I interacted with many great people.

None of it would have been possible without the guidance, insight and energy of my advisor, Paris Sphicas, whose standards are higher even than my own. He is undoubtedly one of the greatest minds working in high-energy physics today.

On more than one occasion I followed in the footsteps of Petar Maksimović, whose star is rising. Ken Kelley made vital contributions to the analysis, and I borrowed a crucial idea from Bob Mattingly. Discussions with Tushar Shah were varied and always fascinating, and Troy Daniels, Wasiq Bokhari, Baber Farhat, Paul Ngan, Steve Tether, Gerry Bauer, Sham Sumorok and Jeff Tseng made it an honor to be a part of the MIT-CDF group.

Joe Kroll, Barry Wicklund, Pat Lukens, Jonathan Lewis, Fritz DeJongh, Manfred Paulini, William Trischuk, Simona Rolli, Fumi Ukegawa and numerous other members of the CDF collaboration contributed time and effort. Rowan Hamilton and Steve Hahn supplied me with fine literature, and Randy Herber is a true wizard.

I am indebted to Jerry Friedman and Larry Rosenson for being the nicest people at MIT. Steve Pavlon is a true friend, and Peggy Berkowitz is always there to help. Bruno, Joost and Han supplied distraction when I needed it most.

Gratitude beyond words is reserved for my parents, Nada and Željko, who imposed few constraints, and for baba Savka, deda Branko, deda Mirko and Nana for giving me love, strength, wisdom and curiosity.

This work is dedicated to Sandra and Vanja, who flourished where most would have withered.

Contents

List of Figures

8

List of Tables

Chapter 1

Introduction

This thesis arose from a search for orbitally excited states of B mesons produced in collisions of hadrons. Seemingly straightforward at the outset, this task proved to require putting numerous pieces together to get the whole picture.

The spectroscopy of B mesons is, to the extent of our present knowledge, fully described by the best theory of fundamental interactions we have at hand, the Standard Model [1]. A study of this spectrum, then, is not done with the intent of probing for unknown phenomena (the glorious "New Physics" that is the holy grail of every self-respecting physicist nowadays); the utility of such a study lies mostly in learning about the bound states of quarks that are notoriously difficult to describe theoretically because of the non-perturbative nature of the strong interactions which govern their properties. An additional motivation is the possibility of using the decays of these excited states to reveal the properties of the long-lived ground states at the time of their production—a pathway into the study of CP violation we describe below.

The purpose of this first chapter is to lay the groundwork by describing the most important features of the production and decay of B (and D) mesons. Chapter 2 describes the experimental apparatus, while chapter 3 explains the selection of data for the measurement. The most significant experimental backgrounds are discussed in chapter 5, and chapter 6 elaborates the procedure for extracting the signal. The results are presented in chapter 7. A summary of the work accomplished can be found

in chapter 8.

1.1 The Standard Model

The twentieth century has seen the consolidation of all our knowledge about the fundamental particles and interactions into an amazingly successful theory we now call the Standard Model [1]. Apart from gravitation, to this date there is no significant evidence of any phenomena that lie outside the context of this theory.

The Standard Model describes the dynamics of the fundamental particles of matter, quarks and leptons, through the exchange of particles that mediate interactions: photons for the electromagnetic force, $W^{\pm}$ and Z^0 for the weak force, and gluons for the strong force. Quarks, unlike leptons, carry color charge, and so do not appear "bare" in the nature, but are always combined with other quarks or antiquarks to form color-neutral hadrons.

All these particles can conveniently be thought of as excitations of a vacuum described by the Standard Model lagrangian—given a chance, they will decay into states of lower energy.

There are three generations of quarks and leptons, differring only in the masses of the particles. The visible universe consists mostly of the first generation of particles, the u and d quarks, the electron and its neutrino. Particles from higher generations decay into the ones from the first generation, so in order to study them we have to produce them in collisions.

The b quark is the analog of the d quark from the third generation, and is especially interesting for study because it is the heaviest quark that forms hadrons—the recently discovered top quark decays too swiftly to hadronize. The hadrons containing the b quark decay through weak interaction, as that is the only possible way to change the flavor of the b quark in a decay. A common way to think about this transition is that the b quark itself decays weakly, and the other quarks making up the hadron are merely spectators in the process.

In this analysis we are concerned mostly with the *mesons* containing b quarks. These are bound states of a b quark and a light antiquark: a $\bar{d}$ completes a $\bar{B}^0$ meson, a $\bar{u}$ a B^-. A bound state of a b quark and an s antiquark also forms a neutral B meson, which we denote $\bar{B}^0_s$ to distinguish it from the $\bar{B}^0_d$.[1]

Weak interactions appear to affect leptons and quarks in a radically different way. While each lepton can become its own neutrino through the emission of a W boson, quarks can undergo a rich set of transitions both within each generation and between them. In the Standard Model this is dealt with by introducing a flavor basis for weak interactions that is different from the one for strong interactions, *i.e.* by rotating three quarks of the same electroweak charge with a unitary matrix:

$$
\begin{pmatrix} d' \\ s' \\ b' \end{pmatrix}_L = V \begin{pmatrix} d \\ s \\ b \end{pmatrix}_L
\tag{1.1}
$$

The weak transitions viewed from the new (d', s', b') basis occur only within each "generation". The unitary transformation matrix V is called the Cabibbo-Kobayashi-Maskawa (CKM) [2] matrix, and can be empirically parametrized in the following way [3]:

$$
V = \begin{pmatrix} V_{ud} & V_{us} & V_{ub} \\ V_{cd} & V_{cs} & V_{cb} \\ V_{td} & V_{ts} & V_{tb} \end{pmatrix} = \begin{pmatrix} 1 - \lambda^2/2 & \lambda & A\lambda^3(\rho - i\eta) \\ -\lambda & 1 - \lambda^2/2 & A\lambda^2 \\ A\lambda^3(1 - \rho - i\eta) & -A\lambda^2 & 1 \end{pmatrix} + \mathcal{O}(\lambda^4)
\tag{1.2}
$$

The last form of the CKM matrix shows explicitly that we can express it using three real numbers and one complex phase: A, λ and $\sqrt{\rho^2 + \eta^2}$ are real, and the complex phase is $\arg(\rho, \eta)$. A, λ and ρ turn out to be of the order of unity, and the complex phase is discussed in section 1.1.2.

---

[1] B_c^-, the bound state of a b and a $\bar{c}$, has recently been discovered [26] as well.

1.1.1 $B^0 - \bar{B}^0$ Mixing

The two neutral B mesons, B^0 and $\bar{B}^0$, can spontaneously transform into one another through the higher-order diagrams shown in figure 1-1. This is a consequence of the fact that all their quantum numbers except flavor are the same: weak interactions do not conserve flavor, so they provide a mechanism for this transformation. This phenomenon is called "oscillation" or "mixing," and is not a peculiarity of the B mesons. It was first observed with the $K^0 - \bar{K}^0$ mesons in 1956 [4, 5], and in 1987 with the $B^0 - \bar{B}^0$ as well [6].
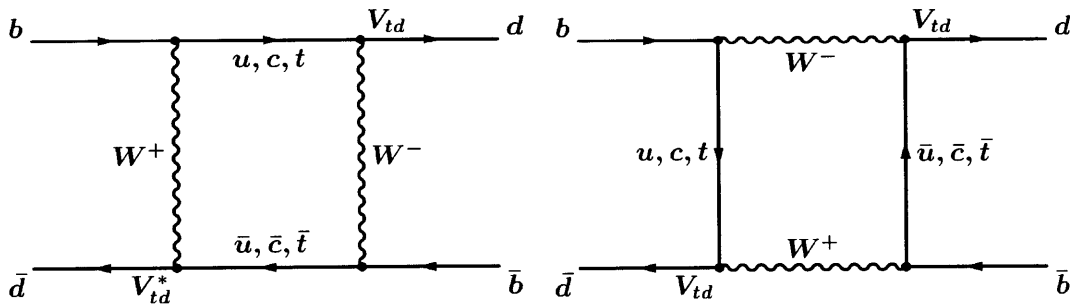
Figure 1-1: Processes that transform B^0 into $\bar{B}^0$ and vice versa.

The time evolution of a neutral B state is given by the following phenomenological Hamiltonian:

$$H \begin{pmatrix} |B^0\rangle \\ |\bar{B}^0\rangle \end{pmatrix} = \begin{pmatrix} m - \frac{1}{2}i\Gamma & m_{12} - \frac{1}{2}i\Gamma_{12} \\ m_{12}^* - \frac{1}{2}i\Gamma_{12}^* & m - \frac{1}{2}i\Gamma \end{pmatrix} \begin{pmatrix} |B^0\rangle \\ |\bar{B}^0\rangle \end{pmatrix} \qquad (1.3)$$

Here $|B^0\rangle$ and $|\bar{B}^0\rangle$ are the eigenstates of strong interactions (i.e., every B meson is produced as a pure $|B^0\rangle$ or $|\bar{B}^0\rangle$ in $p\bar{p}$ collisions), the diagonal elements describe the evolution and decay of strong eigenstates in absence of mixing (m being their mass and Γ their width), and the off-diagonal elements describe the mixing. The m_{12} and Γ_{12} can be calculated from the diagrams in figure 1-1; m_{12} correspond to virtual $B^0 - \bar{B}^0$ transitions, while Γ_{12} describes real transitions due to decay modes common to both the B^0 and the $\bar{B}^0$ (such as $\pi^+\pi^-$) which comprise only a tiny fraction of all

B decays so Γ_{12} can be safely ignored in this discussion.

Diagonalizing the Hamiltonian in 1.3 gives us the CP eigenstates (neglecting CP violation)

$$|B_1\rangle = \frac{1}{\sqrt{2}}(|B^0\rangle + |\bar{B}^0\rangle) \qquad (1.4)$$

$$|B_2\rangle = \frac{1}{\sqrt{2}}(|B^0\rangle - |\bar{B}^0\rangle) \qquad (1.5)$$

which are linear combinations of the strong eigenstates. Their masses and widths are

$$m_{1,2} = m \pm \frac{\Delta m}{2} \qquad (1.6)$$

$$\Gamma_{1,2} = \Gamma \pm \frac{\Delta\Gamma}{2} \qquad (1.7)$$

where the splittings are

$$\Delta m = 2Re\sqrt{\left(m_{12} - \frac{\Gamma_{12}}{2}\right)\left(m_{12}^* - \frac{\Gamma_{12}^*}{2}\right)} \qquad (1.8)$$

$$\Delta\Gamma = -4Im\sqrt{\left(m_{12} - \frac{\Gamma_{12}}{2}\right)\left(m_{12}^* - \frac{\Gamma_{12}^*}{2}\right)} \qquad (1.9)$$

To explicitly see the effect of mixing, we start from a pure B^0 meson and calculate the probability of finding a B^0 or a $\bar{B}^0$ after it has lived a time t:

$$P_{B^0 \to B^0}(t) = \frac{1}{4}\left[e^{-\Gamma_1 t} + e^{-\Gamma_2 t} + 2e^{-\Gamma t}\cos(\Delta m \cdot t)\right] \qquad (1.10)$$

$$P_{B^0 \to \bar{B}^0}(t) = \frac{1}{4}\left[e^{-\Gamma_1 t} + e^{-\Gamma_2 t} - 2e^{-\Gamma t}\cos(\Delta m \cdot t)\right] \qquad (1.11)$$

The mass difference Δm, expressed in appropriate units, is just the frequency of oscillation of a neutral B meson into its antimeson: by measuring this frequency we can measure Δm, and through that get a handle on the value of the CKM matrix element V_{td} (since $V_{tb} = 1$ in the Wolfenstein's parametrization, eq. 1.2). Such a measurement was first done in 1993 [7]. Obviously, to perform this kind of measurement we need to know the flavor of the B meson at the time of its decay, which we can

deduce from its decay products, *and* at the time of its production, which is a much more difficult task. The latter was one of our main motivations for searching for the excited states of B mesons—an excited state would decay into a B^0 and one or more additional particles, and from the properties of those other decay products we could tell the flavor of the B^0 at the time of its production.

Turning this discussion around, B^0-$\bar{B}^0$ mixing plays a significant role in looking for the excited B mesons, since it disturbs the correlation of the detected neutral B meson and the other decay products of the excited state. A quantity of interest for us is the *time-integrated* probability that a neutral B produced as one flavor decayed as the other flavor:

$$\chi = \int_0^\infty P_{B^0 \to \bar{B}^0}(t)\, dt. \qquad (1.12)$$

1.1.2 Symmetries and CP Violation

The single most important concept in physics of elementary particles today is probably that of *symmetry.* Laws of conservation of energy and momentum can be thought of as manifestations of certain symmetries of spacetime; the entire dynamics of electroweak interactions in the Standard Model is described as a consequence of an abstract symmetry requirement, that of local gauge-invariance. A symmetry can dramatically simplify an otherwise intractable problem, so it is no wonder that the understanding of symmetries is one of the cornerstones of modern physics.

Some of the most intuitive symmetries in Nature turn out to be quite complex at the particle level. The parity transformation, P, is akin to looking at the world in a mirror—it reverses all three spatial directions. The laws of the macroworld do not change perceptibly when looked at in the mirror, and neither do strong nor electromagnetic interactions. It came as a surprise when experiments in 1954 [8] uncovered that weak interactions are maximally asymmetric with respect to the parity transformation: the left-handed neutrino exists, but the right-handed one does not.

It was expected, however, that the weak interactions will stay symmetric under the

CP transformation, the combination of the parity transformation and charge conjugation, C, which exchanges every particle with its antiparticle. A CP transformation makes a left-handed neutrino into a right-handed antineutrino which exists. This combined symmetry was also shown [9] to be violated in weak interactions, but at a very small level.

It is still expected that the CPT transformation, a combination of CP and the time reversal T, leaves the weak interactions unchanged, since the violation of this combined symmetry cannot be accomodated by any known quantum field theory. This means that the time reversal symmetry has to be violated in weak interactions to balance the CP violation, *i.e.* Nature distinguishes between past and future and between left and right at the most fundamental level. Experiments to date have not been able to detect any violation of the CPT symmetry [10].

In the Standard Model, CP violation is introduced as the complex phase in the CKM matrix—if η were zero in eq. 1.2, CP symmetry would hold in weak interactions. Note that this doesn't mean that the Standard Model *explains* CP violation, it just *allows* its existence, but places no constraints on its magnitude. The Standard Model also doesn't explain why there are exactly three generations of particles or why their masses are what they are. The CKM formalism that describes the interplay of different generations, while allowed by the framework of the theory, is added in an *ad hoc* way. For all these reasons, it is generally accepted that there exists an underlying theory, of which the Standard Model is an approximation, that describes these and many other open parameters from first principles. The ultimate goal of elementary particle physics is to find a doorway to testing candidates for such an underlying theory, and one of the promising areas of research is the CP violation in weak interactions, which is technically covered well enough, but conceptually remains a mystery.

To date the CP violation in weak interactions has been observed only in the K^0–$\bar{K}^0$ system. Its effect is expected to be much larger in the B^0–$\bar{B}^0$ system, and the first pieces of experimental evidence are appearing [12, 11] at this time. These analyses
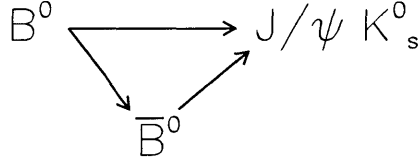
Figure 1-2: Two paths for the decay $B^0 \to J/\psi K_S^0$.

rely on finding neutral B mesons that decay into a CP eigenstate $J/\psi K_S^0$. This decay can proceed via the two paths shown in figure 1-2, and the interference between these two paths results in a *time-dependent asymmetry*:

$$\frac{N_{\bar{B}^0 \to J/\psi K_S^0}(t) - N_{B^0 \to J/\psi K_S^0}(t)}{N_{\bar{B}^0 \to J/\psi K_S^0}(t) + N_{B^0 \to J/\psi K_S^0}(t)} = \sin 2\beta \ \sin \Delta m t \qquad (1.13)$$

where t is the time the B meson lived before decaying, $\tan \beta = \frac{\eta}{1-\rho}$ (η and ρ are the CKM parameters from equation 1.2), and Δm is the mass splitting defined in equation 1.8. In other words, of all the neutral B mesons that decay into $J/\psi K_S^0$ after having lived a time t, more (or less, depending on the value of t) than a half could have been produced as B^0 (as opposed to $\bar{B}^0$), hence the term "asymmetry." The magnitude of the CP violation determines the amplitude of this asymmetry through the $\sin 2\beta$ term, so by measuring this amplitude we get a measurement of the angle β. Obviously, such a measurement relies on determining the flavor of the neutral B meson at the time of its production, lending importance to the understanding of excited B states.[2]

---

[2] $B^0 \to J/\psi K_S^0$ is by no means the only decay with large manifest CP violation effects, it is just the most experimentally accessible one at the moment. Many other final states which are CP eigenstates can be used to measure the magnitude of CP violation; in particular, the $B^0 \to \pi^+\pi^-$ decay has received a lot of attention recently as a handle on the angle α, where $\tan \alpha = \eta/(\eta^2 - \rho(1 - \rho))$. B flavor tagging plays a crucial role in these measurements regardless of the decay chain.

1.2 Heavy-Light Mesons and Heavy Quark Symmetry

The spectrum of B mesons is determined by the properties of strong interactions, which are described in the Standard Model by Quantum Chromodynamics (QCD), the theory we get by requiring that the observed world stay unaffected by an SU(3) group of local gauge transformations.

The carriers of strong interactions in QCD are gluons which, unlike photons, carry themselves the color charge they couple to. This peculiar nature of strong interactions, combined with the ratio of the number of colors to the number of quark flavors, results in effective anti-screening of the color charge of the source, so the strong interaction constant, α_s, is of the order of unity at low energies, and then *decreases* as the momentum transfer of the interaction increases. In other words, while perturbative expansion in powers of $1/\alpha_s$ works in the high-energy regime, low-energy QCD problems are notoriously difficult to solve analytically, and are usually handled by invoking some symmetry of QCD rather than by doing dynamical calculations (*e.g.* the strong isospin symmetry).

Recent theoretical advances have made use of another such symmetry, called the Heavy Quark Symmetry [13], to predict the spectra of heavy-light mesons—the mesons containing one heavy quark Q, with mass m_Q that is much greater than the scale Λ_{QCD} of strong interactions.

Because of its high mass, the heavy quark in the meson is not significantly affected by the light quark and the associated gluonic cloud, so we can treat the heavy quark as a static color source located at the origin, and solve the QCD equations for the light quark in its field. Note that this solution does not depend on the flavor of the heavy quark, so the spectrum of all heavy-light mesons is expected to be the same to first order. Moreover, the spin of the heavy quark (S_Q) decouples from the gluonic field, so every orbitally excited state (*i.e.* the one with the angular momentum of the light degrees of freedom different from zero) is expected to be a near-degenerate

doublet in total spin. It is interesting to note that the heavy flavor symmetry is analogous to different isotopes of a given element having the same chemistry, and the spin near-degeneracy is analogous to the hyperfine levels in atoms which arise from weak nuclear magnetic moment.

Of course, Heavy Quark Symmetry holds exactly only in the $m_Q \to \infty$ limit; in reality we have to take into account the Λ_{QCD}/m_Q corrections which break the degeneracy of hyperfine levels and make the spectra dependent on the mass of the heavy quark.

The total angular momentum of the light degrees of freedom is $\mathbf{J}_q = \mathbf{L} \oplus \mathbf{S}_q$, where $\mathbf{L}$ is the "orbital" angular momentum of the light quark and $\mathbf{S}_q$ is its spin. The spin of the meson is then $\mathbf{J} = \mathbf{J}_q \oplus \mathbf{S}_Q$.

In the L = 0 case there are two states, with anti-parallel and parallel spins of the two quarks. These are respectively B and B^* in the radial ground state, B' and B'^* in the first radially excited state, etc. The "radial" here refers to the radial wavefunction of the light quark. The properties of the radial ground states are well understood. The B' and B'^* states have negative parity, so they decay through two pions and cannot be used for flavor tagging; we do not consider them any further in this analysis. The states we are looking for are the positive-parity, orbitally excited (L = 1), radial ground states,[3] collectively labelled the B^{**}.

We expect to see four B^{**} resonances, illustrated in figure 1-3. In the commonly used $N^{2S+1}L_J$ spectroscopic notation, 2^3P_0 and 2^3P_2 states correspond to B_0^* and B_2^* mass eigenstates, whereas 2^1P_1 and 2^3P_1 are linear combinations of B_1 and B_1^* and are not mass eigenstates. By virtue of heavy flavor symmetry, the same discussion holds for K^{**} and D^{**} states, where the heavy quark is an s or a c respectively; the former are of no importance to us, the latter we return to in chapter 4.

The early predictions of the properties of the B^{**} states [14] relied on the Heavy

---

[3]Note that, because of the increasing-with-distance nature of the strong interaction between the two quarks, the first orbitally excited states actually lie *below* the first radially excited ones, in stark contrast with atomic spectra; this has caused some confusion in the literature: the B^{**} states are sometimes labelled 1P and sometimes 2P.
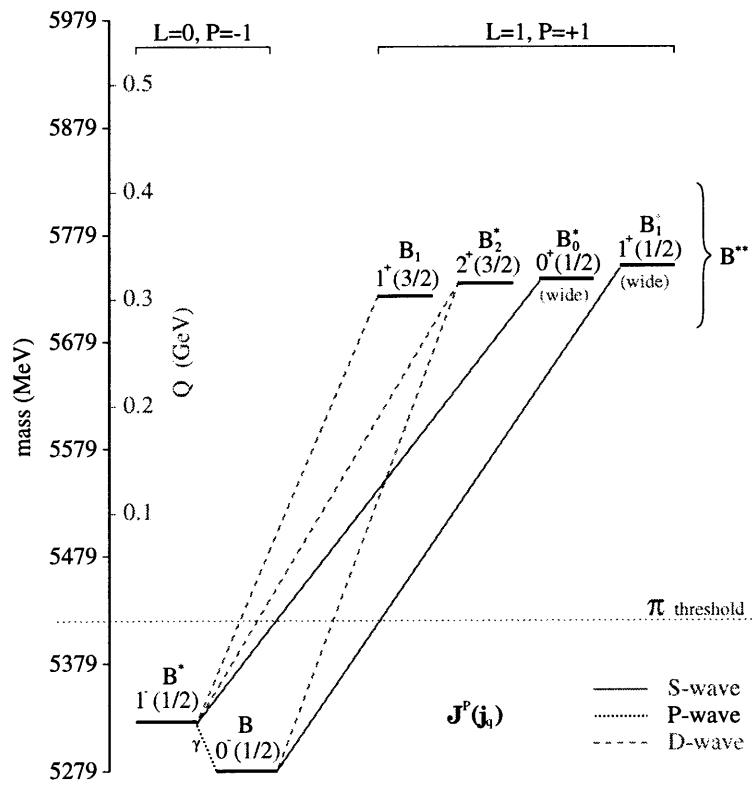
Figure 1-3: Predicted spectrum and dominant decays of lowest-lying B meson states.

Quark Symmetry and on the observed properties of the analogous K^{**} and D^{**} states. Recently calculations in the nonrelativistic valence quark approximantion [15] and the fully relativistic light quark model [16] have become available. The latter model is in good agreement with the properties of the observed heavy-light mesons, as well as heavy quarkonia, so we give its synopsis below. The predictions of all three models are given in table 1.1.

By extrapolation from the observed properties of the K^{**} and D^{**} systems (reference [14]), we set the widths of the two narrow B^{**} states to 20 MeV (J = 1) and 24 MeV (J = 2). Lacking a good prediction for the widths of the two broad resonances, we set them to 100 MeV guided by [17]. (The results presented in chapter 7 indicate that the properties of the broad resonances have relatively little bearing on the numbers we measure.)

Name	J	J_q	Mass (GeV/c^2)			Width	Decays
			EHQ [14]	ref. [15]	EGF [16]		
B_0^*	0	$\frac{1}{2}$	5.650	5.870	5.738	broad	$(B\pi)_{L=0}$
B_1^*	1	$\frac{1}{2}$	5.650	5.875	5.757	broad	$(B^*\pi)_{L=0}$
B_1	1	$\frac{3}{2}$	5.759	5.700	5.719	narrow	$(B^*\pi)_{L=2}$
B_2^*	2	$\frac{3}{2}$	5.771	5.715	5.733	narrow	$(B\pi, B^*\pi)_{L=2}$

Table 1.1: Predicted properties of B^{**} mesons.

The first evidence for the existence of the narrow B^{**} resonances was obtained by the LEP experiments [18, 19, 20, 21]. The rate of B mesons originating from B^{**} decays is found (by all four LEP experiments) to be $\approx 30\%$. In addition, the LEP experiments have reconstructed B^* mesons via the decays $B^* \rightarrow B\gamma$; they find, in agreement with spin-counting statistics, that 3/4 of the 1S states are produced as B^*. The narrow D^{**} states have also been observed [22], but there still is no conclusive evidence for the wide D^{**} resonances.

1.2.1 Relativistic Quark Model

Heavy quark symmetry places strict constraints on the spectrum of heavy-light mesons, but to get quantitative predictions it is necessary to combine it with dynamical non-perturbative models. The recently developed relativistic quark model [16] is one such model. This is a potential model, meaning that the dynamics of the two quarks is described by a quasipotential, which is postulated on the basis of some phenomenological observations. This chapter summarizes its predictions relevant to this analysis.

The advantage of the relativistic quark model over the earlier approaches [14, 15] lies in treating the light quark fully relativistically, and doing the expansion only in inverse powers of the heavy quark mass. This is a significant improvement, as the velocity of the light quark in the meson is estimated at 70–80% of the speed of light.

The bound states of the heavy-light system Qq in the relativistic quark model are the solutions of the following quasipotential equation:

$$\left(\frac{b^2(M)}{2\mu_R} - \frac{\mathbf{p}^2}{2\mu_R}\right)\Psi_M(\mathbf{p}) = \int \frac{d^3q}{(2\pi)^3} V(\mathbf{p}, \mathbf{q}; M)\Psi_M(\mathbf{q}). \qquad (1.14)$$

Here M is the mass of the meson, $b(M)$ is the relative momentum on mass shell in the center-of-mass system

$$b^2(M) = \frac{[M^2 - (m_q + m_Q)^2][M^2 - (m_q - m_Q)^2]}{4M^2}, \qquad (1.15)$$

μ_R is the relativistic reduced mass

$$\mu_R = \frac{E_q E_Q}{E_q + E_Q} = \frac{M^4 - (m_q^2 - m_Q^2)^2}{4M^3}, \qquad (1.16)$$

and E_q and E_Q are

$$E_q = \frac{M^2 - m_Q^2 + m_q^2}{2M}, \quad E_Q = \frac{M^2 - m_q^2 + m_Q^2}{2M}. \qquad (1.17)$$

Obviously, in this approach the entire QCD is hidden in the kernel $V(\mathbf{p}, \mathbf{q}; M)$.

30

The kernel can be written as the sum of the one-gluon exchange term, and a suitably chosen mixture of the scalar and vector linear confining potentials:

$$
\begin{aligned}
V(\mathbf{p}, \mathbf{q}; M) \;=\; & \bar{u}_q(p)\bar{u}_Q(-p)\{\tfrac{4}{3}\alpha_S D_{\mu\nu}(\mathbf{k})\gamma_q^\mu\gamma_Q^\nu \;+ \\
& V_{\text{conf}}^V(\mathbf{k})\Gamma_q^\mu\Gamma_{Q,\mu} + V_{\text{conf}}^S(\mathbf{k})\}u_q(q)u_Q(-q)
\end{aligned}
\tag{1.18}
$$

where α_S is the strong coupling constant, $D_{\mu\nu}$ is the gluon propagator in the Coulomb gauge, V_{conf} is the linear confining potential

$$
V_{\text{conf}} \;=\; Ar + B, \tag{1.19}
$$

$$
V_{\text{conf}}^V \;=\; (1 - \epsilon)(Ar + B), \tag{1.20}
$$

$$
V_{\text{conf}}^S \;=\; \epsilon(Ar + B), \tag{1.21}
$$

and $\Gamma_\mu(\mathbf{k})$ is the effective long-range vector vertex

$$
\Gamma_\mu(\mathbf{k}) \;=\; \gamma_\mu + \frac{i\kappa}{2m}\sigma_{\mu\nu}k^\nu \tag{1.22}
$$

with κ being the Pauli interaction constant characterizing the anomalous chromo-magnetic moment of quarks.

In the $m_Q \to \infty$ limit the heavy quark Dirac spinors have only the upper component different from zero, so the kernel reduces to

$$
\begin{aligned}
V_{m_Q \to \infty}(\mathbf{p}, \mathbf{q}; M) \;=\; & \bar{u}_q(p)\{-\tfrac{4}{3}\alpha_S\frac{4\pi}{\mathbf{k^2}}\gamma_q^0 \;+ \\
& V_{\text{conf}}^V(\mathbf{k})\Big[\gamma_q^0 + \frac{\kappa}{2m_q}\gamma_q^0(\gamma\mathbf{k})\Big] + V_{\text{conf}}^S(\mathbf{k})\}u_q(q)
\end{aligned}
\tag{1.23}
$$

After several further approximations the kernel can be made local in the configuration space, so equation 1.14 becomes

$$
\left(\frac{E_q^2 - m_q^2}{2E_q} - \frac{\mathbf{p^2}}{2E_q}\right)\Psi_M(r) = V_{m_Q \to \infty}(r)\Psi_M(r) \tag{1.24}
$$

31

where E_q is the total energy of the light degrees of freedom, $M = m_Q + E_q$.

This equation can be solved numerically to get the eigenvalues of E_q and the wave functions Ψ_M. The solutions for B and D mesons are shown in table 1.2.1. In the $m_Q \to \infty$ limit the spin of the heavy quark decouples from the light degrees of freedom, so we get degenerate doublets as predicted by the heavy quark symmetry. An interesting feature of heavy-light systems is already apparent at this point in the calculation: the 2P states lie below the 2S states, and the $j_q = \frac{3}{2}$ 2P doublet lies below the $j_q = \frac{1}{2}$ doublet, unlike the atomic spectra.

Similarly to the derivation of equation 1.23, the first order of expansion in inverse powers of heavy quark mass can be treated as a small additional potential δV, such that the total quasipotential is $V_{m_Q \to \infty} + \delta V$. This combined potential can then be treated using perturbation theory to get the predictions for the masses of the excited states at $1/m_Q$ order; the results are also shown in table 1.2.1.

state	D meson		B meson	
$N^{j_q} L_J$	$m_Q \to \infty$	$1/m_Q$	$m_Q \to \infty$	$1/m_Q$
$1^{\frac{1}{2}} S_0$	2.047	1.875	5.394	5.285
$1^{\frac{1}{2}} S_1$		2.009		5.324
$2^{\frac{1}{2}} P_0$	2.436	2.438	5.778	5.738
$2^{\frac{1}{2}} P_1$		2.501		5.757
$2^{\frac{3}{2}} P_1$	2.350	2.414	5.680	5.719
$2^{\frac{3}{2}} P_2$		2.459		5.733
$2^{\frac{1}{2}} S_0$	2.490	2.579	5.835	5.883
$2^{\frac{1}{2}} S_1$		2.629		5.898

Table 1.2: Mass spectrum of B and D mesons predicted by the relativistic quark model. The predictions are given in the $m_Q \to \infty$ limit and after the $1/m_Q$ corrections are applied. All masses are in GeV/c^2.

1.3 Production of B Mesons in $p\bar{p}$ Collisions

1.3.1 Structure Functions

Protons are composite particles. This fact has serious implications for production of particles in $p\bar{p}$ collisions. A proton can be imagined as a collection of three "valence" quarks (two u and one d) swimming in a sea of virtual particles. All these particles, valence and virtual, are called "partons," and each carries a certain fraction x of the proton's momentum.

At TeVatron energies, the collisions occur at the momentum scale such that the colliding partons are essentially free for the duration of the reaction, so to a very good approximation all hard processes can be described as collisions of single partons. This means that the cross-section for production of a certain final state with a given momentum can be found by integrating the parton-level cross-section throughout all the available parton momenta. The distribution of momentum fraction x of parton i inside a composite particle a is called a "structure function" (or "parton distribution function") and denoted as $f_i^a(x)$. The cross-section for production of b quarks in $p\bar{p}$ collisions can therefore be expressed as

$$\frac{d^2\sigma}{dp_\mathrm{T}^b dy^b}(p\bar{p} \to b\mathrm{X}) = \sum_{i,j} \int \frac{d^2\hat{\sigma}}{dp_\mathrm{T}^b dy^b}(ij \to b\mathrm{X}) f_i^p(x_i) f_j^{\bar{p}}(x_j) dx_i dx_j$$

where $\frac{d^2\hat{\sigma}}{dp_\mathrm{T}^b dy^b}(ij \to b\mathrm{X})$ is the parton-level cross-section. The average x of a parton inside a proton is about 10%.

1.3.2 Hadronization of b Quarks

Bare b quarks are colored objects, and therefore cannot survive outside a hadron. After being produced in a collision of two partons, b quarks fly away from the vicinity of the reaction and in the process become color-neutral by pulling pairs of quarks out of the vacuum and forming hadrons with some of them. This process is called "fragmentation" or "hadronization," and is universal to all colored particles coming

33

out of collisions. This is a low-energy process, and so is beyond the reach of pertur-
bative QCD treatment; the best candidates for describing the fragmentation process
are semi-empirical models inspired by theory (see reference [24] for a review).

The entire $p\bar{p}$ collision can be treated as an interaction between free partons,
followed by consolidation of the resulting particles into color-neutral objects. The two
parts of the process happen on very different time scales, so they are factorizable to a
very good approximation. This means that we can, for example, calculate the parton-
level cross-sections using perturbative QCD, and then apply semi-empirical models of
the fragmentation process to the final-state partons to predict the properties of the
observed particles.

The hadronization process differs greatly for light and heavy quarks. The particles
produced in the hadronization of b quarks are *the* most important background in
this analysis, so we reserve the name "hadronization particles" for them alone, to
distinguish them from other fragmentation products that appear in $p\bar{p}$ collisions.

One of the main goals of this analysis was to reduce the dependence of the result
on the fragmentation model used to describe the backgrounds. Some dependence
cannot be avoided, as will become clear in chapter 6; in particular, the properties of
the hadronization particles cannot be measured independently of our result, so we
have to make some assumptions about their gross features based on a semiempirical
model. The model we use is the *string* fragmentation model, developed by the Lund
group [25]. It is based on the idea that, as the colored particles move apart, the
color field between them assumes the shape of a narrow tube ("string") whose energy
depends on its length; as the energy of the string increases, it fragments by producing
quark-antiquark (or diquark-antidiquark) pairs at the breakpoints.

Peterson Fragmentation Function

In the special case of heavy quarks, a simple argument gives us the general form of the
fraction of the momentum of the produced quark retained by the hadron containing
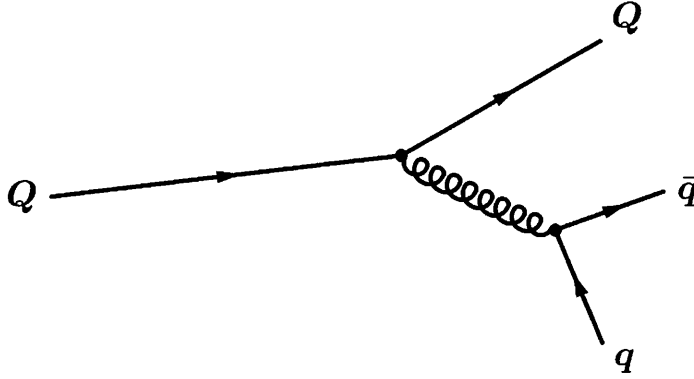
Figure 1-4: Hadronization of a heavy Q by pulling a pair of light quarks out of vacuum.

that quark after the hadronization process. We label this quantity z:

$$z = \frac{\mathrm{p}^{\|}_{hadron}}{\mathrm{P}_{quark}}$$

where $\mathrm{p}^{\|}_{hadron}$ is the projection of the momentum of the hadron on the direction of the heavy quark before the hadronization.

Consider the process shown in figure 1-4. The heavy quark Q pulls a pair $q\bar{q}$ of light quarks out of vacuum, and forms a meson $Q\bar{q}$ ($\equiv H$) with one of them, while the other light quark continues the fragmentation process. The diagram itself clearly violates the conservation of energy, but the ansatz suggested by Peterson *et al.* in [23] states that the hadronization process is completely dominated by the energy dependence of the gluon propagator: the amplitude for this "transition" behaves as

$$\text{amplitude}(Q \to H + q) \propto \Delta E^{-1}$$

where $\Delta E = E_H + E_q - E_Q$ is the energy transfer. This is a consequence of the fact that producing the light quarks slows down the heavy quark only a little.

Working in the infinite momentum reference frame ($\mathrm{p} \gg m$), and assuming

$m_H \approx m_Q$, we get

$$\Delta E = \sqrt{m_Q^2 + z^2 \mathrm{p}^2} + \sqrt{m_q^2 + (1-z)^2 \mathrm{p}^2} - \sqrt{m_Q^2 + \mathrm{p}^2}$$

$$\propto 1 - \frac{1}{z} - \frac{\epsilon_Q}{1-z}$$

where $\epsilon_Q \propto \frac{m_q^2}{m_Q^2}$ is a function of the ratio of the effective quark masses. The fragmentation function is then

$$D(a) = \frac{N}{z\left(1 - \frac{1}{z} - \frac{\epsilon_Q}{1-z}\right)^2} \tag{1.25}$$

The additional z in the denominator is the phase space factor, and the normalization factor N adjusts the area between $z = 0$ and $z = 1$ to unity.

Charge-Flavor Correlation and Flavor Tagging

The hadronization particles are expected to be correlated with the flavor of the b quark. Consider for example the naive picture of string fragmentation in figure 1-5. The $\bar{b}$ quark hadronizes into a B^0 by taking a d quark out of a $d\bar{d}$ pair. The dangling $\bar{d}$ quark hadronizes into a π^+ which signals by its charge that the flavor of the heavy quark during the hadronization process was $\bar{b}$ (i.e., a π^- would indicate a b quark). In the case depicted in diagram (b), when the $\bar{b}$ hadronizes into a B^+, the charge of the pion has the opposite meaning. We can then label all pions produced in association with B mesons as "right sign" or "wrong sign" according to their charge as shown in table 1.3.2.

This simple picture glosses over many important effects, like the production of the excited hadrons and baryons, but the conclusion is valid: we do observe fewer wrong sign than right sign particles around B mesons. This effect is at the core of the "Same-Side Tagging" (SST) technique [40], which was succesfully used to study $B^0 - \bar{B}^0$ mixing on essentially the same dataset as the one used in this analysis. The

quark	right sign	wrong sign
$\bar{b}$	$B^0\pi^+$	$B^0\pi^-$
	$B^+\pi^-$	$B^+\pi^+$
b	$\bar{B}^0\pi^-$	$\bar{B}^0\pi^+$
	$B^-\pi^+$	$B^-\pi^-$

Table 1.3: Charge-flavor correlation of hadronization particles and B mesons.
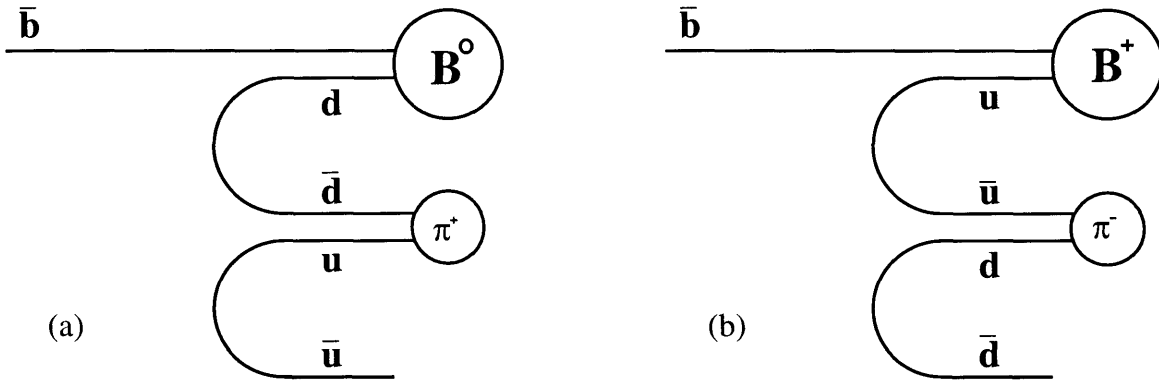
Figure 1-5: Flavor correlation of pions produced during hadronization of b quarks.

correlation tells us about the flavor of the meson at the time of production, so by comparing this information with the reconstructed flavor of the meson at the time of decay we can measure the rate of mixing. Such techniques are called "flavor tagging," and unlike the tagging methods that use the other b quark (which is usually found on the opposite side of the detector, hence the name "Opposite-Side Tagging") this one requires the reconstruction of only the one meson being measured.

While instrumental for the SST, the charge-flavor correlation is actually detrimental to this analysis, since it results in hadronization particles looking more like the signal; this is dealt with at length in chapter 6.

1.3.3 Production Mechanisms

Feynman diagrams for production of b quarks at leading order in perturbative expansion are shown in figure 1-6. At the energies of interest, the quarks and the antiquarks produced through these processes move mostly in the opposite azimuthal directions ("back-to-back"), but the center of mass of the reaction can be boosted along the original direction of protons and antiprotons since the incoming partons can carry very different fractions of (anti)proton momentum.
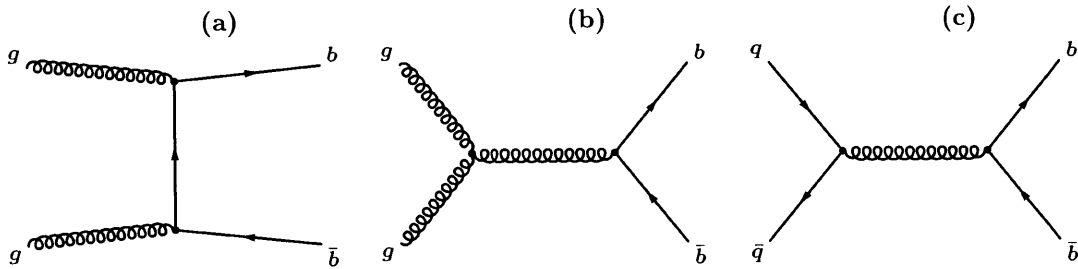
Figure 1-6: Leading order (α_s^2) processes for b production in $p\bar{p}$ collisions.

A significant portion of b quarks in this analysis, however, comes from higher-order production. Figure 1-7 shows some of the next-to-leading order processes. The diagrams (a), (b) and (c) show the final-state gluon radiation. The diagram (f)

38

("flavor excitation") is the scattering of a gluon from one incoming particle off of a virtual b from the other; in this case one of the heavy quarks is likely to continue near the original direction of the incoming particles. The processes shown in diagrams (d) and (e) ("gluon splitting") tend to produce heavy quarks that are close to each other, since the mass of their parent gluon is likely to be small; this production mechanism has a significant effect on our result, as will be explained in chapter 6.
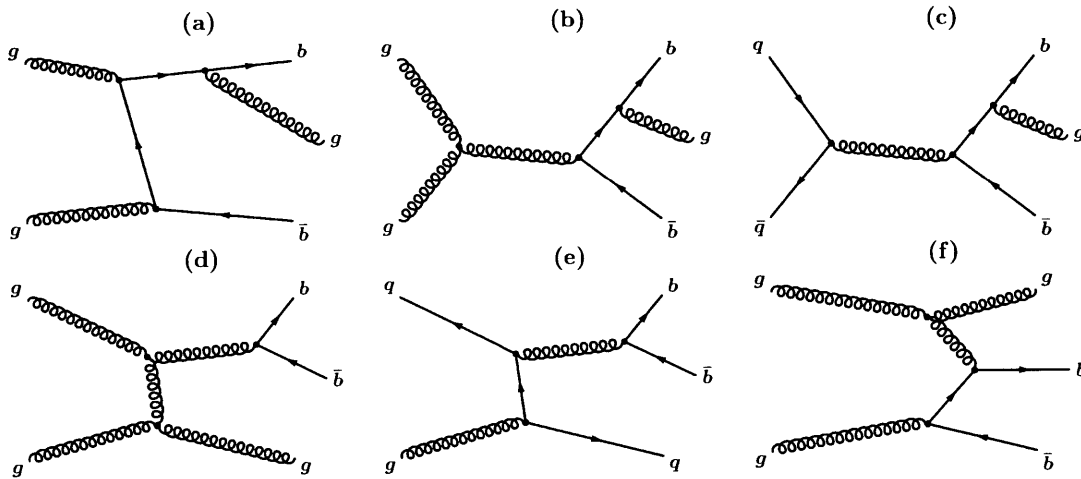
Figure 1-7: Some of the next-to-leading order (α_s^3) processes for b production in $p\bar{p}$ collisions.

Chapter 2

The CDF Experiment

The data used for this analysis was collected at the Collider Detector at Fermilab (CDF), a general purpose particle detector installed at the TeVatron collider at Fermi National Accelerator Laboratory (FNAL). The infrastructure involved in producing the data sample is immense; this chapter gives a synopsis of the accelerator and the detector, and concentrates on the components of the detector that were instrumental for this measurement. A comprehensive description of the detector can be found in [27].

2.1   The Accelerator

The TeVatron accelerator collides protons and antiprotons at a center-of-mass energy $\sqrt{s} = 1.8\,\mathrm{TeV}$. A number of steps are required to get the particles to the moment of collision (see figure 2-1).

The chain starts with hydrogen gas, which is ionized by adding electrons. The H$^-$ ions are then accelerated to 750 keV using a Cockroft-Walton electrostatic generator, and inserted into a linear accelerator (LINAC) where they are further accelerated to 200 MeV. Upon exiting LINAC, the ions pass through a carbon foil which captures the electrons, and the resulting protons are accelerated to 8 GeV in a synchroton accelerator (Booster).
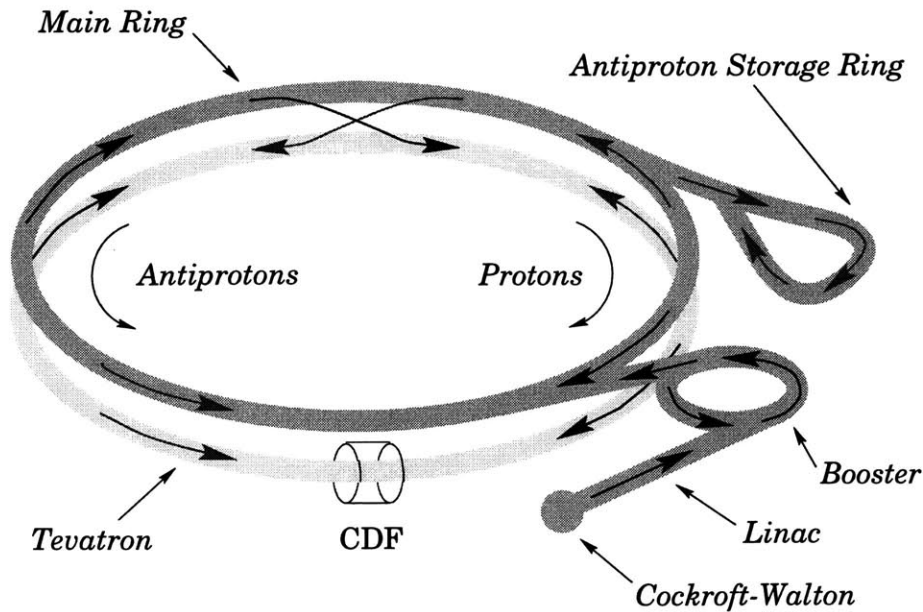
Figure 2-1: A schematic of the TeVatron collider.

From the Booster, the protons enter the Main Ring, another synchrotron accelerator, where they are accelerated to 150 GeV. From here the protons can be sent to different destinations: for fixed-target experiments they are sent directly to targets; for operation in collider mode, they are used for production of antiprotons most of the time, or are injected into the TeVatron after a large enough store of antiprotons has been accumulated.

Antiprotons are produced in collisions of protons from the Main Ring with a tungsten target—they are extracted from collision products and stochastically cooled [28] in the Debuncher before being stored in the Accumulator. The Accumulator can keep bunches of 8 GeV antiprotons circulating for a long time. When a sufficiently large number of antiprotons accumulates, they are injected back into the Main Ring (in the direction opposite that of protons) and accelerated to 150 GeV.

Protons and antiprotons enter the TeVatron from the Main Ring. Both the TeVatron and the Main Ring are located in the same 4 miles long circular tunnel. The TeVatron uses superconducting magnets and cavities, and can accelerate the particles

to 1 TeV. The TeVatron keeps the particles in 6 + 6 bunches which meet at collision points every $3.5\,\mu s$. Collisions can occur in six areas: one hosts the CDF detector, another one the D0 detector; the remaining four are not used at present.

The data for this thesis was collected during the 1992–1995 data-taking period, "Run 1," when the collider was run at 900 GeV per beam for a total center-of-mass energy $\sqrt{s} = 1.8$ TeV. Run 1 consisted of two separate runs, 1A and 1B, between which some components of the detector and the data acquisition system were upgraded. Run 1A lasted from August 1992 until May 1993, Run 1B from January 1994 until July 1995. The total integrated luminosity collected during Run 1 was approximately $110\,pb^{-1}$.

2.2 The Detector

2.2.1 Coordinates and Track Parameters

The TeVatron collides unpolarized beams of protons and antiprotons, therefore all physical observations are invariant under rotations around the beam line. Many calculations are then simplified by using a cylindrical coordinate system with the z axis pointing along the beam direction. The polar angle θ is then measured with respect to this axis, and the azimuth ϕ (by convention) with respect to a horizontal line perpendicular to the beam axis.

Since protons and antiprotons are composite particles, the interactions occur between individual partons and therefore the center of mass of an interaction at parton level can have a large momentum along the z axis in the laboratory frame of reference. To simplify calculations of cross-sections, it is customary to use a polar variable invariant under z boosts instead of the polar angle θ. We can construct such a variable by rewriting the invariant cross-section $E\frac{d^3\sigma}{(dp)^3}$ as

$$E\frac{d^3\sigma}{(dp)^3} = E\frac{d^2\sigma}{\pi \mathrm{p_T} d\mathrm{p_T} dp_z},$$

where p_T is the component of momentum transverse to the beam axis, and observing that only E and p_z change under z boosts, so we can replace them with a variable y (called "rapidity") such that

$$E\frac{dy}{dp_z} = 1.$$

Solving for y gives

$$y = \frac{1}{2}\ln\left(\frac{E + p_z}{E - p_z}\right).$$

Rapidity y is usually approximated by "pseudo-rapidity" η

$$\eta \equiv \frac{1}{2}\ln\left(\frac{p + p_z}{p - p_z}\right) = -\ln\left(\tan\frac{\theta}{2}\right)$$

which is independent of the mass of the particle and has a simple relationshihp with the polar angle. Pseudo-rapidity of a massles particle is equivalent to its rapidity; for massive particles the two are the same in the $p_T \gg m$ limit.

From the discussion above it follows that the position *and* the momentum of the track a charged particle leaves in the detector can be fully described with the following five parameters:

- p_T—the component of the momentum transverse to the beam axis ("transverse momentum"),

- η—the pseudo-rapidity,

- ϕ—the azimuth,

- d_0—the distance of closest approach to the beam line ("impact parameter"), and

- z—the position along the z axis of the point of closest approach to the beam line.

The magnitude of transverse momentum, p_T, is calculated from the observed curvature of the trajectory in the magnetic field, and is independent of the mass of the

43

particle that left the track. The distance of closest approach, d_0, is a signed quantity for the same reason: the sign depends on whether the distance is on the inside or the outside of the curve.

It is also worth noting that we only have five variables to describe the position and momentum of particles. The absence of the sixth is a consequence of the fact that we cannot see with the detector the exact point in space where a particle originated—that we have to estimate from the topology of the chain of reactions we are looking for.

The 3D opening angle between two tracks is often expressed as a boost-invariant quantity ΔR:

$$\Delta R = \sqrt{(\Delta\phi)^2 + (\Delta\eta)^2}.$$

2.2.2 Overview

A schematic of the CDF detector is shown in figure 2-2. Protons collide with antiprotons in the center of the detector (in the lower right corner of the schematic). The distribution of collisions is Gaussian along the beam axis with a width of about 30 cm. In the plane perpendicular to the beam line, the collision region is circular with a diameter of 40 μm in Run 1A, 25 μm in Run 1B.

The collision region is surrounded by tracking detectors: the Silicon Vertex Detector (SVX), the Vertex Time Projection Chamber (VTX), and the Central Tracking Chamber (CTC). These are all placed inside a superconducting solenoid, which produces a 1.412 T field covering a cylindrical region 4.8 m long and 3 m in diameter. The tracking system is effective from about 8° to 172° in polar angle, with three-dimensional coverage between 40° and 140°.

Outside the magnet are the calorimeters: the Central Electromagnetic Calorimeter (CEM) and the Central Hadronic Calorimeter (CHA). Only muons and neutrinos have a high probability of penetrating the calorimeters, so muon chambers are placed on the outside of the detector: the Central Muon Chamber (CMU) outside the CHA, and the Central Muon Upgrade outside the return yoke.
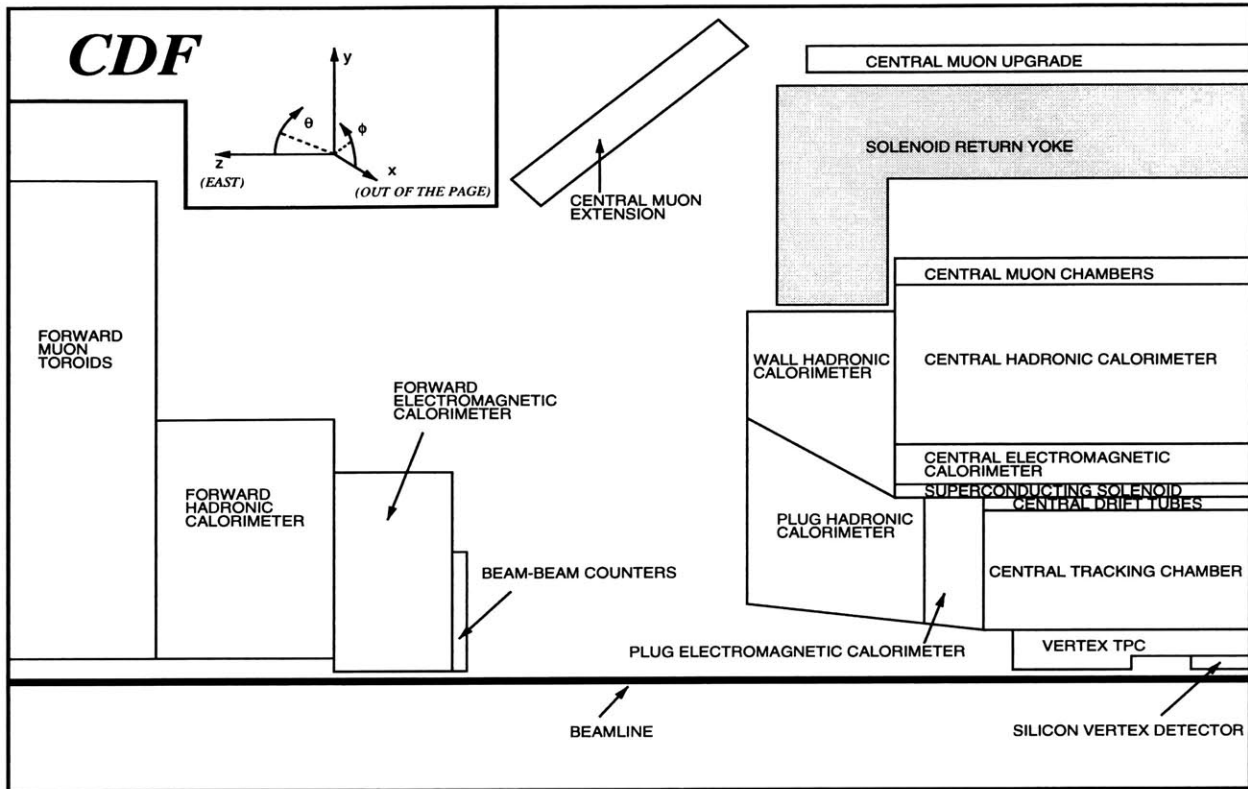
Figure 2-2: A schematic of one quarter of the CDF detector. The detector is cylindrical and forward-backward symmetric. The interaction region is in the lower right corner.

Several other detectors are placed forward and backward of the collision point, but in this analysis only the central ones are used. The following sections describe them in more detail.

2.2.3 Silicon Vertex Detector (SVX)

The SVX is a solid-state detector placed around the beam pipe. It measures the azimuthal position and transverse momentum of charged particles. The original SVX was installed at the beginning of Run 1A, and replaced with a very similar detector called SVX' at the beginning of Run 1B because of the radiation damage to the original. The differences between the two detectors are summarized in table 2.1; in this text both will be referred to as SVX.

Feature	SVX	SVX'
Channels	46080	46080
z coverage	51.1 cm	51.1 cm
Gap at z=0	2.15 cm	2.15 cm
Radius of layer 0	3.0049 cm	2.8612 cm
Radius of layer 1	4.2560 cm	4.2560 cm
Radius of layer 2	5.6872 cm	5.6872 cm
Radius of layer 3	7.8658 cm	7.8658 cm
Overlap of layer 0	-1.26°	0.17°
Overlap of layer 1	0.32°	0.32°
Overlap of layer 2	0.30°	0.30°
Overlap of layer 3	0.04°	0.04°
Silicon	one-sided	one-sided
Power	DC	AC, FOXFET bias
Passivation	none	polyimide
Atmosphere	Argon/Ethane+H_2O	Dry Nitrogen
Readout chip	SVX IC Rev. D	SVX IC Rev.H3
Sampling	quadruple	double
Noise	2200 electrons	1300 electrons
Gain	15 mV/fc	21 mV/fc
Reset/Integrate	3.5 μs	3.5 μs
Readout time	2.7 μs	2.1μs
Radiation Limit	15-20 KRad	> 1 MRad
Bad channels	2.93%	1.73%
Typical Occupancy	7-10%	5%
Max Occupancy	12-20%	25%

Table 2.1: A comparison of the SVX and the SVX'.
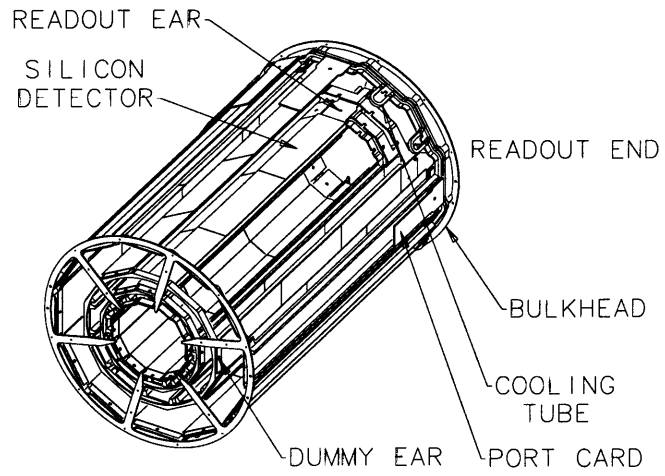
Figure 2-3: A schematic of an SVX barrel.
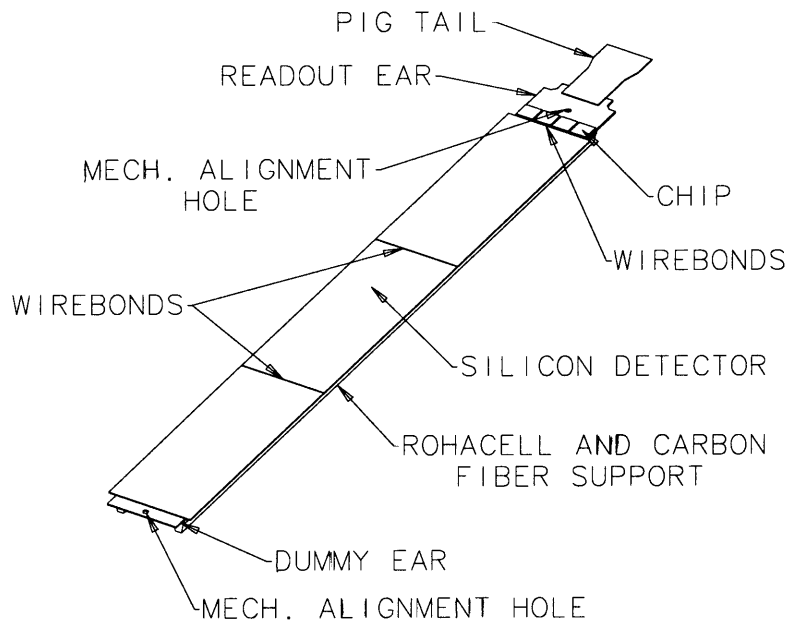
Figure 2-4: A schematic of an SVX ladder.

The SVX consists of two barrels, shown in figure 2-3. The barrels are placed along the detector axis with a 2.15 cm gap between them at $z = 0$. A barrel consists of four concentric layers of twelve "ladders" each. A ladder is shown in figure 2-4. Ladders are made up of three 8.5 cm long silicon wafers, with strips of silicon aligned with the barrel axis. The pitch of the strips is $60\,\mu m$ in the inner three layers and $55\,\mu m$ in the outermost layer. The ladders are read out in a "sparse mode," meaning that only the strips above threshold are read out for further processing. Ladders in layers 1 through 4 have 2, 3, 4 and 6 readout chips respectively, each with 128 channels, for a total of 46080 channels for the entire SVX detector. The typical readout time is about 2 ms, among the longest of all CDF detector subsystems.

The hit resolution in the transverse plane on a single wafer is about $10\,\mu m$, which translates into the impact parameter resolution shown in figure 2-6. The total length of the SVX is 51 cm and the interaction region is a 30 cm wide Gaussian, so the geometric acceptance is about 60% with $|\eta|$ coverage up to 1.9. The SVX gives no information about the z position of tracks.

2.2.4   Vertex Time Projection Chamber (VTX)

The VTX is a 3 m long time-proportional drift chamber placed around the SVX. It consists of 28 octagonal modules, each segmented into eight wedges. At the center of each module is a high-voltage grid; electrons drift away from this grid and pass through the cathode grids into the two endcaps, which contain sense wires. By measuring the drift times we get $r - z$ information about passage of particles. The z positions of $p\bar{p}$ collisions ("primary vertices") are then reconstructed from this information, and used as seeds for finding tracks in the CTC and the SVX. The typical z resolution is 1–2 mm, depending on the number of reconstructed tracks. The pseudorapidity range of VTX is $|\eta| < 3.25$.

2.2.5 Central Tracking Chamber (CTC)

The CTC is a 3.2 m long drift chamber surrounding the VTX and extending to the solenoid, covering the pseudorapidity range $|\eta| < 1.1$. It contains 84 layers of sense wires. The wires are subdivided into nine superlayers: the five "axial" layers, containing 12 wires each, alternate with the four "stereo" layers that contain 6 wires each. The wires in the axial layers are parallel to the detector axis, therefore giving only $r - \phi$ information about tracks. The wires in the stereo layers are at a 3° angle with respect to the detector axis; the combined readout from the axial and the stereo layers thus contains information about the z position of tracks as well.

A cross-sectional view of the CTC is shown in figure 2-5. Within each axial (stereo) superlayer, sense wires are placed in groups of 12 (6) along a line in the $r - \phi$ plane inclined at 45° with respect to the radial direction. Such groups, called "cells," are spaced so that the maximal drift time is 800 ns, much less than the 3.5 μs interval between bunch crossings. The 45° tilt of cells serves to compensate for the angle at which electrons drift in combined electrical and magnetic field (the "Lorentz" angle); it also helps resolve the left-right ambiguity—it is impossible to tell which side of the wire the electrons came from, so the tilt results in the wrong solution (the "ghost track") being shifted by about 70° with respect to the real track.

The CTC is the mainmast of CDF tracking. The (two different) algorithms that find tracks in the detector start from the hits in the outermost superlayer of the CTC, connecting them with the hits in the inner superlayers and trying to fit a helix compatible with one of the primary vertices found by the VTX. After a track has been found in the CTC, the search for hits continues in the SVX in a narrow region ("road") around the extrapolated track. The SVX can thus dramatically improve the resolution of the measurement of impact parameter of CTC tracks (figure 2-6), and by extending the visible part of the helix the p_T resolution as well. The resulting momentum resolution of the CTC-SVX system is

$$\frac{\delta p_T}{p_T} = \sqrt{0.0066^2 + (0.0009 p_T)^2}\, \text{GeV}^{-1}.$$

49
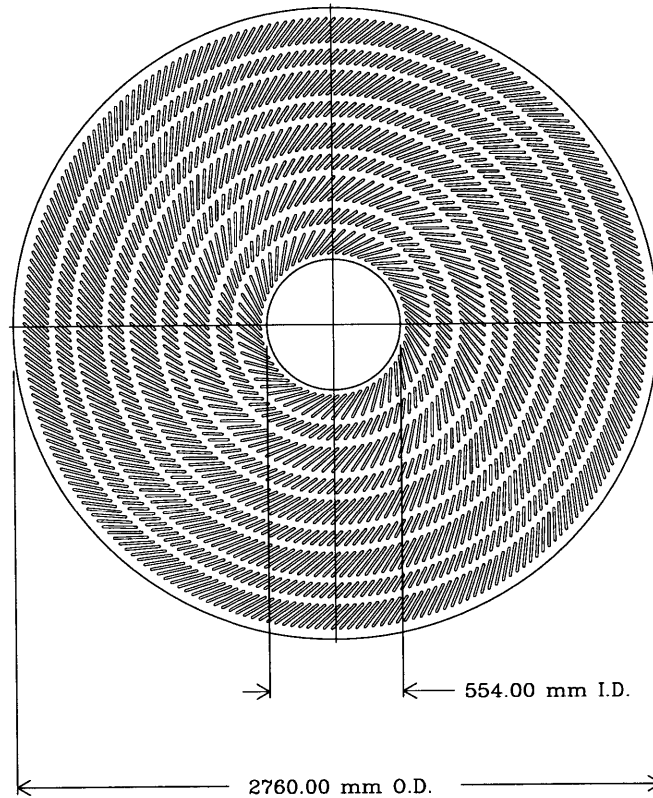
Figure 2-5: Cross-sectional view of the CTC. The slanted lines are cells made up of 12 (axial) or 6 (stereo) wires. The division into nine radial superlayers is clearly visible.

2.2.6 Calorimetry

The tracking detectors and the solenoid are surrounded by calorimeters, which measure the energy of incident particles by stopping them. Particles passing through material produce a "shower" when stopped. For example, an electron can radiate a photon which converts into an electron-positron pair; these in turn radiate more photons, and so on until the remaining electrons and photons have insufficient energy for creation of more particles. Similarly, hadrons produce showers by interacting with hadrons from the atomic nuclei in the material.

The calorimeters at CDF cover pseudorapities up to $|\eta| < 4.2$, but this analysis
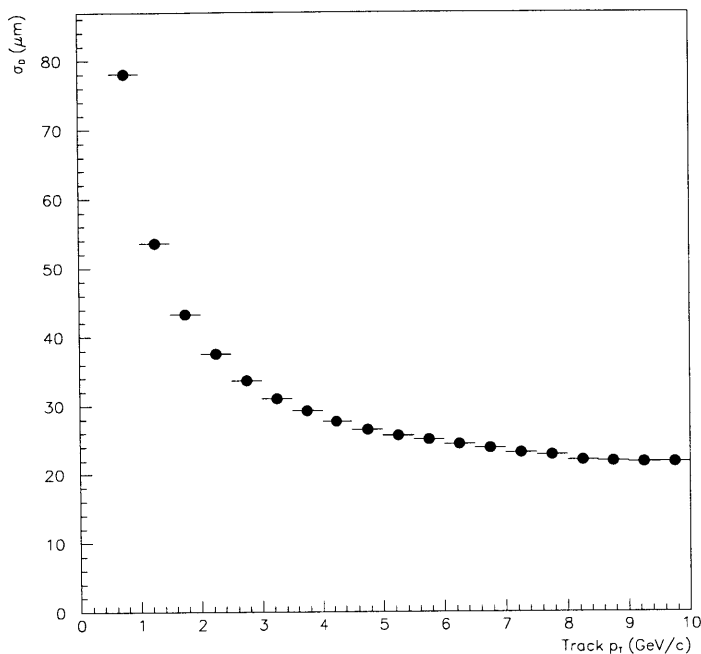
Figure 2-6: Impact parameter resolution of CTC-SVX tracks as a function of transverse momentum.

uses only the ones in the central region: the Central Electromagnetic Calorimeter (CEM) covers the $|\eta| < 1.1$ region, while the Central Hadronic Calorimeter (CHA) has $|\eta| < 0.9$ coverage. The central calorimeters consist of "towers" which point to the interaction region. Each tower covers 15° in ϕ and 0.1 in η.

The CEM is placed outside the solenoid. Its towers consist of 62 alternating layers of lead and scintillator, and a proportional chamber for measurement of the shower profile. The light produced by showers in the scintillating material is waveshifted and fed into photomultiplier tubes. The positional resolution of the CEM is about 2 mm, and the energy resolution is $\frac{\delta E_T}{E_T} = \sqrt{(13.7\%/\sqrt{E_T})^2 + (2\%)^2}$. Its thickness corresponds to about 18 radiation lengths at 90° incidence.

The CEM stops most electrons and photons, but most hadrons pass thorough it unaffected. These are stopped in the CHA, which surrounds the CEM. The CHA

51

towers consist of 64 alternating layers of steel and scintillator. The energy resolution of the CHA is $\frac{\delta E_T}{E_T} = \sqrt{(50\%/\sqrt{E_T})^2 + (3\%)^2}$, and its thickness about 4.5 interaction lengths at normal incidence.

2.2.7 Muon Chambers

From the interaction region to the outer edge of the CHA there are at least five interaction lengths of material, so almost all particles that penetrate that far are either muons or neutrinos. Neutrinos can easily sail through an entire planet without interacting with matter; they are invisible in our detector. Muons are charged and long-lived, and we can detect them by finding the ionized track they leave in their wake.

The CDF has four muon detectors: the Central Muon Chamber (CMU), the Central Muon Upgrade (CMP), the Central Muon Extension (CMX), and the Forward Muon System (FMU). This analysis makes use of only the two central detectors, CMU and CMP.

The Central Muon Chamber is placed outside the CHA, and covers the region $|\eta| < 0.6$ with 85% coverage in ϕ. The Central Muon Upgrade covers the same range of pseudorapidity, but is placed beyond the return yoke of the magnet (which stops more of the hadrons that escape through the calorimeters), and covers some gaps in ϕ in the CMU. Both are made up of four layers of drift chambers. The data used in this thesis contains only muons that were seen in both the CMU and the CMP.

Being outside the magnet, the muon chambers measure only the position and angle of passage of charged particles. To be considered a muon, a hit in the muon chambers (called a "stub") has to be matched with a track seen in the CTC, where its momentum is measured. The match has to be good in both the position and the slope caused by bending of the track in the magnetic field. For muons used in this thesis the muon chambers are almost fully efficient.

2.2.8 Triggers

Particles collide inside the CDF detector almost 300000 times a second. The detector feeds almost 140000 digitally read out channels. Recording every single collision over several years of running is clearly beyond the reach of the present technology. Also, the processes that are interesting for research comprise only a tiny fraction of all collisions at TeVatron energies (for example, tens of microbarns for production of central b quarks [30] compared to 75 millibarns of total $p\bar{p}$ cross-section at 1.8 TeV [31]). For these reasons, the data undergoes extensive filtering in the on-line data acquisition system; this process is called "triggering." The CDF detector has three levels of triggering.

The Level 1 trigger is analog. It requires either a stub in the muon chambers, or energy above a certain threshold deposited in the calorimeters. The decision time at Level 1 is well below the time between bunch crossings, so there is no "dead time" (interval when the detector cannot accept new events) incurred at this stage. About two thousand events per second pass Level 1.

Events that pass the Level 1 trigger are digitized and sent to the Level 2 trigger, which runs more complex algorithms that take more time. It looks for clusters of calorimeter towers that indicate electrons, photons or jets, and for correlation between tracks and stubs in muon chambers in search of muons. The acceptance rate of the Level 2 trigger is up to about 50 events a second (the actual rate is a function of instantaneous luminosity, and can be adjusted in the long run by changing trigger parameters to achieve the maximum utilization of the available processing power while keeping the dead time as low as possible).

If the event passes Level 2, the entire detector is read out, and all the fragments of the event are sent to a single Level 3 trigger machine through a sophisticated demultiplexer called the "event builder." The readout time is about 30 ms, which results in the total detector dead time of about 10%. The Level 3 hardware are off-the-shelf computers running the Unix operating system. The Level 3 trigger itself is a lean version of the offline reconstruction code that does a quick analysis of the entire

event and forwards it to one of several streams for storage and further processing. Fewer than ten events per second end up on tape.

The most interesting triggers for this analysis are at Level 2. Our data sample is extracted from the "inclusive lepton" datasets, the ones where the only requirement is that an event contains either a muon or an electron of high transverse momentum. These are found at Level 2 by the Central Fast Tracker (CFT), a hardware processor that looks for tracks in the CTC. The geometry of the CTC is such that every high-p_T particle passes near at least one wire in every superlayer. The charge collected on the wire nearest the track is called a "prompt" hit, because the electrons drift onto the wire very soon after the bunch crossing; similarly, the hits on the wires further away from the track are called "delayed." The CFT starts from a prompt hit in the outermost superlayer, and tries to match hits in the other axial superlayers to a pattern in a lookup table. On the first pass only the prompt hits are matched, and the second pass includes the delayed hits as well. The patterns in the lookup table are correlated with the transverse momentum of tracks, so a match is also a measurement of track p_T with the resolution $\frac{\delta p_T}{p_T} = p_T \cdot 3.5\%$ (p_T in GeV). For inclusive lepton triggers, CFT tracks that are likely to have $p_T > 7\,\text{GeV}$ are matched with stubs in the muon chamber or clusters in the electromagnetic calorimeter, so there is an implicit cut on the transverse momentum of the leptons we use caused by the necessity for triggering.

2.2.9   Monte Carlo Simulation of the Detector

There are numerous Monte Carlo generators that attempt to model the physics of $p\bar{p}$ collisions (see for example [33, 34]). These usually produce, in suitably formatted arrays, a detailed report on the particles entering and exiting the collision. In order to fully understand what these collision products will look like in our data, we need a simulation of the detector that takes the output from the Monte Carlo generators and models the response of the detector to particles passing through it. For this purpose we use the "quick" detector simulator (QFL, [37]), which doesn't calculate

54

the response of each detector component, but rather models the combined response of the whole detector and the reconstruction algorithms; the model is then tuned to agreement with the data. The output of QFL is in the same format as the processed detector data, so we use the same programs to analyze both the generated and the recorded events.

Chapter 3

Finding B Mesons

A B meson lives about 1.6 picoseconds at rest. This means that, although it decays too rapidly to be observed directly through its interaction with matter,[1] it can travel far enough away from the collision point that a sophisticated detector like the SVX can tell us that its decay products did not originate in the $p\bar{p}$ collision. Seeking out such "displaced" tracks is the most powerful known technique for finding B mesons produced in hadronic collisions.

To get a sample rich in B mesons, we start from a dataset of events that passed a certain set of triggers. The exact choice of triggers depends on the particular B decay chain we are hoping to reconstruct. Datasets containing different B decay chains also contain different types and quantities of background events—the so-called "fake" B events. The signature of a decay chain in the detector is called a "topology"; usually a number of different physical processes can have the same topology and we have to extract the one we want using cuts on various kinematic variables. To that end, we perform several passes of filtering on the original dataset, until we end up with a smaller dataset with a satisfactory signal-to-background ratio.

A favorite B dataset for many analyses is the one containing the decays $B \rightarrow J/\psi K$ and $B \rightarrow J/\psi K^*$, where the J/ψ decays into two muons. All the B decay products are detected, so these are called "fully reconstructed" B mesons. The muons

---

[1] At the present stage of detector design.

are easy to trigger on, and very few other particles can fake a muon, so this B dataset has very good signal-to-background ratio. Its main weakness is the low branching ratio for these decays, only about 1×10^{-3} and 1.7×10^{-3} respectively [32], so it contains a miniscule fraction of all B mesons that are potentially available. Two independent searches for the excited B mesons have already been performed at CDF using this dataset [41, 42], and the number of B events in the sample has proven insufficient to unambiguously establish their presence. Obviously, the only way past this hurdle, short of waiting for more data in the future, was to extract another dataset using other B decays, preferably with higher branching ratios.

3.1 Lepton+Charm Dataset

By far the largest fraction of B mesons decays through a $b \rightarrow c$ weak transition. The c quark ends up in a D meson, which decays further and we can reconstruct its decay products. The virtual W can give rise to either a quark-antiquark pair, or a lepton and its neutrino. The latter case is much more interesting to us than the former, since leptons (other than τ) are typically easier to trigger on than hadrons; such decays are called "semileptonic".

This analysis is based on the data containing the signatures of the following six semileptonic decay chains:

$$B^+ \quad \rightarrow \quad \nu \ell^+ \bar{D}^0, \ \bar{D}^0 \rightarrow K^+ \pi^- \tag{3.1}$$

$$B^+ \quad \rightarrow \quad \nu \ell^+ \bar{D}^0, \ \bar{D}^0 \rightarrow K^+ \pi^- \pi^+ \pi^- \tag{3.2}$$

$$B^0 \quad \rightarrow \quad \nu \ell^+ D^-, \ D^- \rightarrow K^+ \pi^- \pi^- \tag{3.3}$$

$$B^0 \quad \rightarrow \quad \nu \ell^+ D^{*-}, \ D^{*-} \rightarrow \bar{D}^0 \pi_s^-, \ \bar{D}^0 \rightarrow K^+ \pi^- \tag{3.4}$$

$$B^0 \quad \rightarrow \quad \nu \ell^+ D^{*-}, \ D^{*-} \rightarrow \bar{D}^0 \pi_s^-, \ \bar{D}^0 \rightarrow K^+ \pi^- \pi^+ \pi^- \tag{3.5}$$

$$B^0 \quad \rightarrow \quad \nu \ell^+ D^{*-}, \ D^{*-} \rightarrow \bar{D}^0 \pi_s^-, \ \bar{D}^0 \rightarrow K^+ \pi^- \pi^0 \tag{3.6}$$

Here, as in the rest of this text, the charge-conjugated decay chains are implicitly

accepted as well.

The topology of these decays is shown in figure 3.1. The B meson travels a discernible distance away from the point where the $p\bar{p}$ collision occured (the "primary" vertex). All its decay products, as well as the products of strong decays of excited D mesons, appear to originate at the point in space where the B meson decayed (the "secondary" vertex). The D travels a bit further, due to its picosecond lifetime, and decays into several hadrons. In all decay chains except 3.6, $D^0 \rightarrow K^+\pi^-\pi^0$, we fully reconstruct the D meson, i.e. we observe all its decay products. The lepton is our pass through the triggering system. The neutrino cannot be detected, hence we lose the information about its kinematic properties; we therefore call these the "partially reconstructed" B mesons. The loss of the neutrino degrades our measurement of the properties of the B meson, and we elaborate on that later in the chapter.
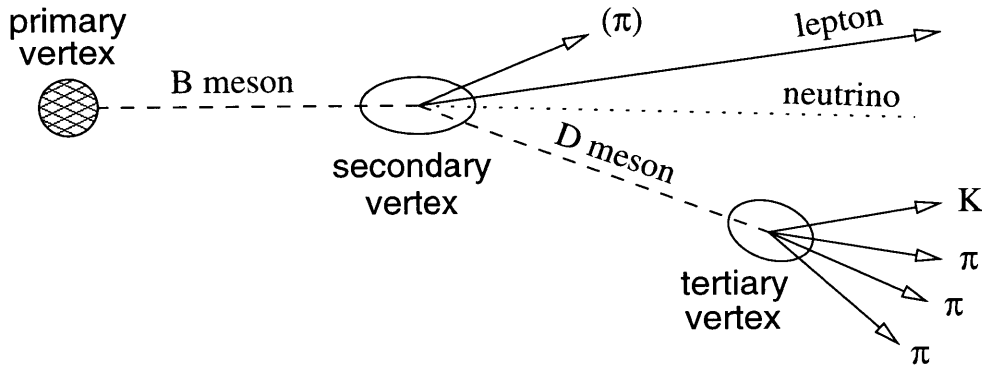
Figure 3-1: Topology of a semileptonic B decay. Visible particles are shown as solid lines. The pion(s) originating at the secondary vertex come from the decay of excited states of D mesons and $B \rightarrow \nu\ell DX$ decays.

Our sample has two other shortcomings compared to the fully reconstructed one mentioned earlier. First, single-lepton triggers have more stringent kinematic requirements than two-muon triggers because of the much higher level of background, so the gain in the number of B events is not nearly as large as two orders of magnitude we would naively expect from the ratio of branching ratios. Second, we have to deal with

strong decays of higher excited states of D mesons; we do not attempt to detect these, but they introduce flavor mixing into our sample, as will be explained in chapter 6 and appendix D.

3.1.1 Event Selection Requirements

Technically, the reconstruction of the semileptonic B decays listed above proceeds as follows.

The process starts with the single-lepton datasets, which contain events where at least one electron or muon passed a single-lepton trigger. We loop through all such events and use all electrons and muons found in the central detectors that have $p_T > 6\,\text{GeV}/c$; this requirement rejects nearly all leptons that didn't pass the trigger but ended up in the dateset.

We then try to find a $D^{(*)}$ candidate around each lepton. For this we consider only tracks that are in a cone $\Delta R < 1.0$ around the lepton; this requirement reduces the combinatorial explosion and is fully efficient for the B momenta in question. Each track has to pass a set of "quality" cuts: at least five hits in at least two axial CTC superlayers, at least two hits in at least two stereo superlayers, radius of the point of exit from the CTC greater than 130 cm (to ensure that the track is fully contained within the CTC), and passage through the SVX (except one track in the case of the $D^0 \rightarrow K\pi\pi$ signatures). The tracks also have to be compatible with the primary vertex nearest the lepton, meaning they originated less than 5 cm away from it along the z axis. Sets of tracks that conform to a particular topology are then assigned identities and masses,[2] and if their combined invariant mass is near that of a D meson the set is handed to a "vertexing" algorithm.

Vertexing consists of changing the measured track parameters within their errors so that the tracks pass through a common point—their vertex. The new track parameters are different from the measured ones, so the invariant mass of the set is

---

[2] We cannot distinguish K from π very effectively using the CDF detector, so we do not attempt to do so, but rather use the most likely mass assignment.

59

different from the "raw" mass calculated before vertexing. The resulting D vertex is then required to pass additional requirements on the maximal χ^2 of the vertexing fit and the distance from the primary vertex L_{xy} (usually relative to its uncertainty $\sigma_{L_{xy}}$). Such a D meson is then combined with the lepton (and the soft pion in the case of decays through a D^*) to form a B meson, and another vertexing is performed on all visible decay products.

The exact requirements for each signature are listed in appendix B. Figure 3.1.1 shows the invariant mass distributions seen in the data.

For the first five decay chains the quantity plotted in figure 3.1.1 is the invariant mass we get by combining all the tracks that make up the D candidate. Real D mesons show up as a peak on top of a smooth background distribution. The shape of the peak is determined by the resolution of the detector (the natural width of D mesons is much smaller than the spread from measurement errors); it is described well by a Gaussian distribution centered at the mass of D mesons, $1.8645\,\mathrm{GeV}/c^2$ for $\bar{D}^0$ and $1.8693\,\mathrm{GeV}/c^2$ for D^-. In the two decay chains that proceed through a D^*, 3.4 and 3.5, additional background rejection is achieved by exploiting the very narrowly peaking difference between the D^* and $\bar{D}^0$ masses. This difference is only about $145\,\mathrm{MeV}/c^2$ above the threshold for the $D^{*-} \to \bar{D}^0\pi$ decay, so the pion has very low momentum in the D^* frame of reference; this is why we use a subscript s for *soft* to distinguish this pion from other pions in the decay chain.

The background distribution comes from random tracks that when combined happen to have the invariant mass close to the mass of a D meson. If we accept only the candidates in a narrow mass window that includes the D peak, we will have a sample rich in D mesons, but we still expect some background "under" the peak that we have to account for. We do this by background subtraction: we assume that the background shape is linear in the region plotted (a safe assumption since the peaks are so narrow), and extrapolate the amount of background under the peak from the one seen away from the peak, in the region that contains only background. Technically this is done by choosing the "signal region" and two "sideband regions," the
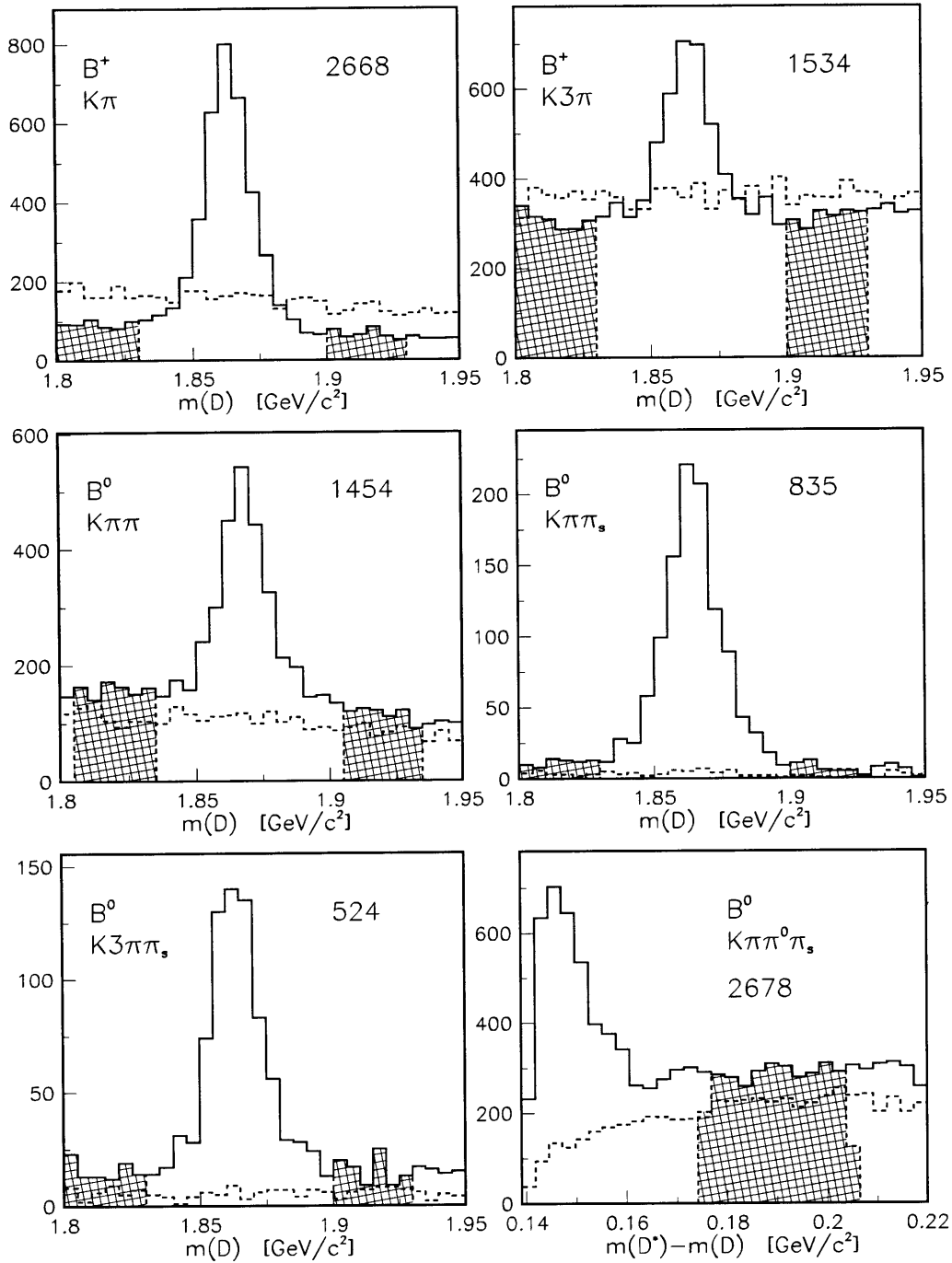
Figure 3-2: The spectra of invariant mass of D candidates in the data. A soft pion, π_s, in the signature comes from a D^* in the decay chain. The sidebands are shaded, and the estimated number of real B events in the signal region is shown in each plot.

former containing the peak, and the latter containing only background; when we plot various quantities we will be subtracting their distribution seen in the sidebands from the one seen in the signal region. The sideband regions are shaded in figure 3.1.1, and appendix B lists the boundaries of signal and sideband regions for each signature. Table 3.1.1 lists the number of events in each signal region, as well as the estimated numbers of background events and real B mesons.

decay signature	candidates in signal region	estimated background	number of B mesons
$\bar{D}^0 \to K^+\pi^-$	3141	473 ± 22	2668
$\bar{D}^0 \to K^+\pi^-\pi^+\pi^-$	3404	1870 ± 43	1534
$D^- \to K^+\pi^-\pi^-$	2275	821 ± 29	1454
$D^{*-} \to \bar{D}^0\pi_s^-, \; \bar{D}^0 \to K^+\pi^-$	891	56 ± 7	835
$D^{*-} \to \bar{D}^0\pi_s^-, \; \bar{D}^0 \to K^+\pi^-\pi^+\pi^-$	618	94 ± 10	524
$D^{*-} \to \bar{D}^0\pi_s^-, \; \bar{D}^0 \to K^+\pi^-\pi^0$	4288	1610 ± 40	2678

Table 3.1: Number of B and background events in each decay signature.

Looking at the decay chains 3.1 through 3.6 we see that the lepton always has the same charge as the K. We use this fact, along with the charge correlation between other particles, to reduce the combinatorial background by rejecting combinations of tracks with the wrong correlation of charges. It is useful, however, to plot the invariant mass distribution of candidates whose lepton and K have different charge. These distributions are shown as dashed histograms in figure 3.1.1. The absence of peaks in these distributions insures that there isn't a significant number of events in the sample where the lepton is either fake or produced independently of the D meson, the so-called "open charm". In absence of the neutrino and therefore B mass peaks, this is the strongest argument we have that all our $\ell + D$ events really contain B mesons.

The last decay chain, 3.6, requires a slightly different treatment from the other five. In this case we do not reconstruct the D meson fully, we lose the neutral pion. This situation is analogous with losing the neutrino from the B decay—there is no $K\pi$ invariant mass peak, unlike in the other signatures. What we have to use in

its place is the peak in the mass difference between the D^{*-} candidate and its $\bar{D}^0$ subset, $m(K, \pi, \pi_s) - m(K, \pi)$, the same quantity we use to reduce background in the signatures 3.4 and 3.5. This distribution is shown in the last plot in figure 3.1.1. Two peculiarities are apparent from the plot. First, partial reconstruction of the $\bar{D}^0$ momentum results in a much more smeared peak, spread over almost $20 \, \mathrm{MeV/c^2}$, compared to $\pm 3 \, \mathrm{MeV/c^2}$ window in the signatures 3.4 and 3.5. Second, the background distribution is not flat, but rises sharply from the kinematic threshold, following the shape of the phase space. Consequently, the choice of the sideband region is dictated by the *shape* of the candidates with the wrong ℓ–K charge correlation (lepton and K have different charge), which are made up of combinatorial background, normalized in the region $m(K, \pi, \pi_s) - m(K, \pi) > 0.17 \, \mathrm{GeV/c^2}$ to the right-sign ℓ–K distribution (lepton and K have the same charge). Other than this subtlety, the background subtraction proceeds in the same manner.

3.1.2   Soft Pion Veto

From the perspective of the code that searches for the signatures, the only difference between the decays 3.1 and 3.4, and similarly between 3.2 and 3.5, is the presence of an additional soft pion produced in the decay of a D^* meson. This means that the code looking for the signature of 3.1 (3.2) will also find the decays 3.4 (3.5). This is of course undesirable, so in looking for the decays 3.1 and 3.2 we also look for any pions that could have come from a $\bar{D}^*$ decay, and reject all the events where such a pion is found. This procedure is called the "soft pion veto," meaning that when the veto is satisfied the candidate is rejected. The veto pions are not required to pass the same stringent quality cuts as the ones accepted as $\bar{D}^*$ decay products from the decay chains 3.4 and 3.5; this significantly improves the separation between the B flavors, and the decrease of the $\bar{D}^0$ finding efficiency by vetoing on random tracks is very small.

63

3.1.3 Removal of $\bar{D}^0 \to K^+ \pi^- \pi^+ \pi^-$ Duplicates

In the two decay signatures where the $\bar{D}^0$ decays into a K and three pions, 3.2 and 3.5, there is a possibility that one set of tracks will form more than one $\bar{D}^0$ candidate. This happens when two different mass assignments pass the cuts, *e.g.* the ones with the exchanged K track and π track of the same charge. This is undesired combinatorial background, so we require that no two candidates have the same set of $\bar{D}^0$ tracks. Of the combinations that do have the same sets of $\bar{D}^0$ tracks, we pick the one that has the smallest χ^2 (in the $\bar{D}^0$ signature 3.2), or the $m(D^{*+}) - m(\bar{D}^0)$ closest to its central value (in the D^{*+} signature 3.5). This requirement is applied to candidates with the right-sign ℓ–K correlation after the wrong-sign ones have been eliminated.

3.2 Generating Monte Carlo Events

We use two different Monte Carlo programs to generate B events (see figure 3.2). The first one is Pythia 5.7/Jetset 7.4 [33], which simulates the entire $p\bar{p}$ collision. This is a very sophisticated simulator, but it requires vast amounts of processing power. That is why, for predictions about the B decay chain only, we use a much faster "Bgenerator" program [34], which generates only b quarks according to the p_{T} spectrum distribution from the inclusive b-quark production calculation by Nason, Dawson and Ellis [35], and converts them into B mesons according to the Peterson fragmentation function (section 1.3.2 and reference [23]) without creating any other hadronization particles. The output of both generators is in the HEPEVT event format, described in reference [32].

Events are then passed into a specialized Monte Carlo program developed by the CLEO collaboration (CLEOMC, also called QQ [36]), which redecays all B mesons it finds in the event record, without disturbing any other particles. Its output then goes through a simple filter that rejects events without a $\ell + D^{(*)}$ candidate to speed up the generation, and optionally applies the trigger requirement.

Events that pass this filter advance through a fast detector simulation, performed
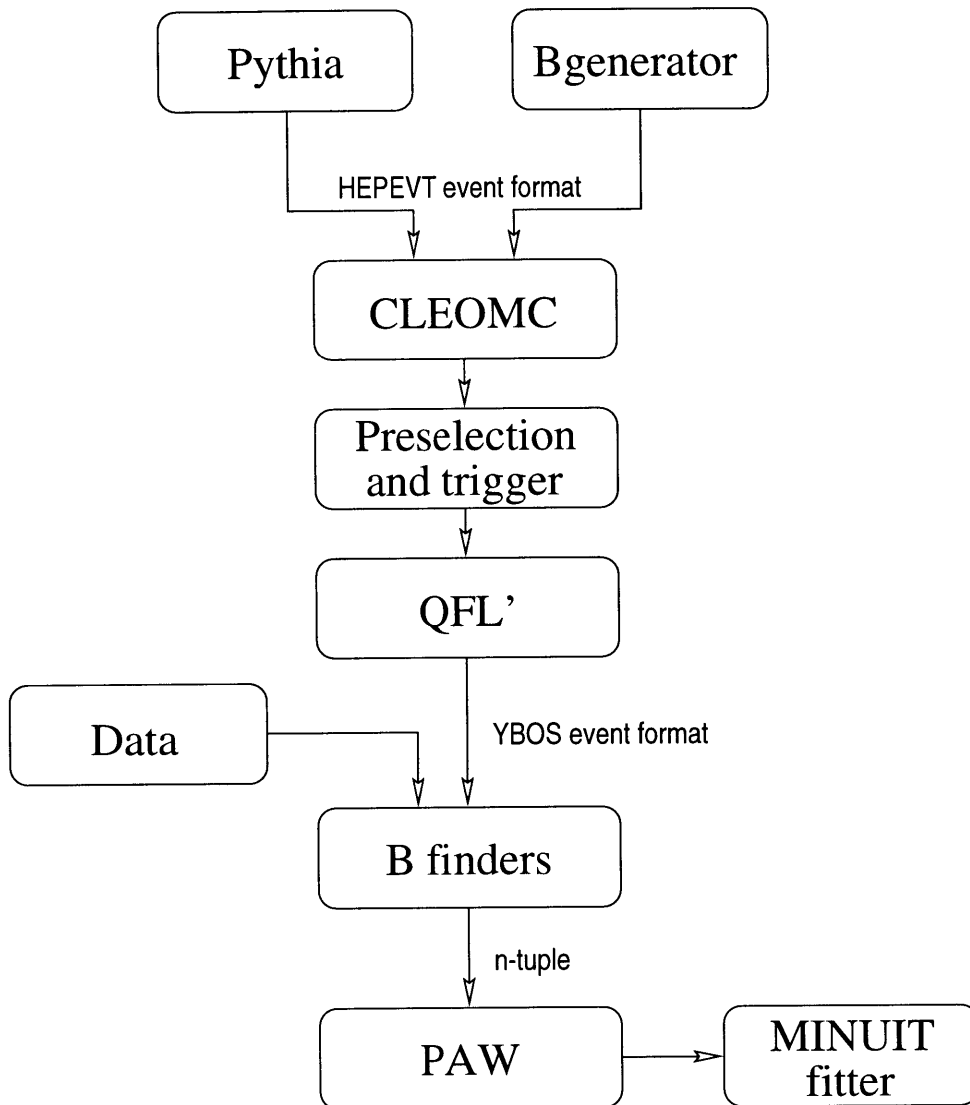
Figure 3-3: The structure of the Monte Carlo generators. Generated events are reconstructed using the same B finding code used on the data.

by the QFL' program [37]. This simulation creates hits and performs the complete track reconstruction only in the SVX; in the CTC parametrized track resolutions are used instead. QFL' also includes conversions and bremsstrahlung.

The output of QFL' is in the same format as the data, so from here on the same modules are used to find B mesons and extract results.

3.2.1 Trigger Parametrization

The requirement that the lepton from B decay pass the trigger significantly affects the p_T spectrum of reconstructed mesons. To reproduce the spectra seen in the data with the Monte Carlo generators, we have to apply a similar bias.

Figure 3.2.1 shows the ratio of the p_T distributions of the Monte Carlo-generated leptons without any trigger requirement and the ones seen in the data. The electron and muon triggers are different, so we compare them separately. We fit the turn-ons with an error function, which rises from 0 to 1 through a region with a width σ_{p_T} around the central value p_T^0. The fits and the resulting values of the parameters are also shown in figure 3.2.1.

3.3 Finding B^{**} Mesons

Once we reconstruct the B, searching for the B^{**} appears simple enough: we combine the B meson with all the pions found around it, and look for peaks in the invariant mass distribution of the composite object. There is, however, a serious problem with this simple scheme—the neutrino we lose carries away a significant fraction of the meson's mass. The invariant mass of the visible decay products can therefore be anywhere between the $\ell D^{(*)}$ threshold and the B mass, a window of more than $3\,\text{GeV}/\text{c}^2$! Consequently, the B^{**} peak is spread over a similar range of masses. Moreover, the B^{**} decays strongly, so the pion from its decay originates at the primary vertex (leaves a "prompt" track). As will become obvious later in the text, a plethora of other particles are also produced independently of the $B^{(**)}$ meson that come from
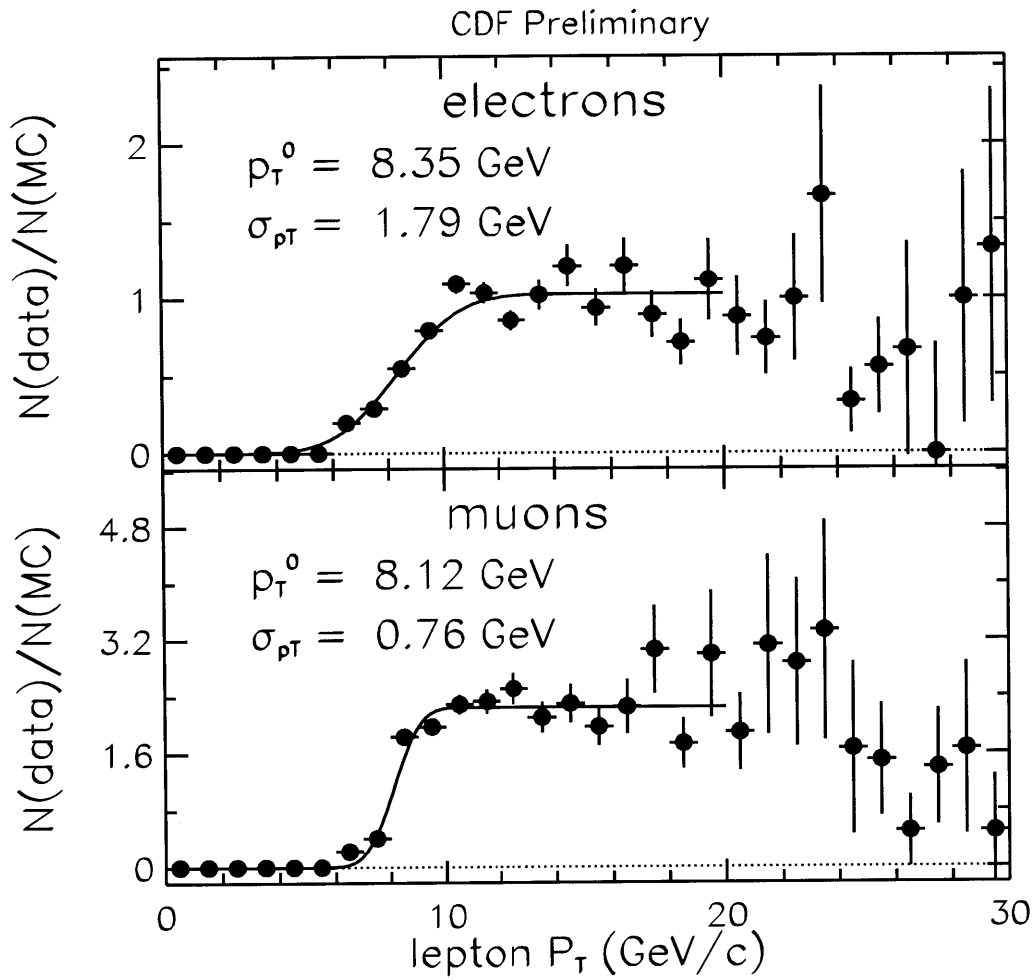
Figure 3-4: The ratios of lepton p_T distributions in the data and the Monte Carlo for electrons and muons showing the trigger turn-on. The fit to an error function is also shown.

the primary vertex; we cannot possibly distinguish such a wide B^{**} mass peak from prompt backgrounds.
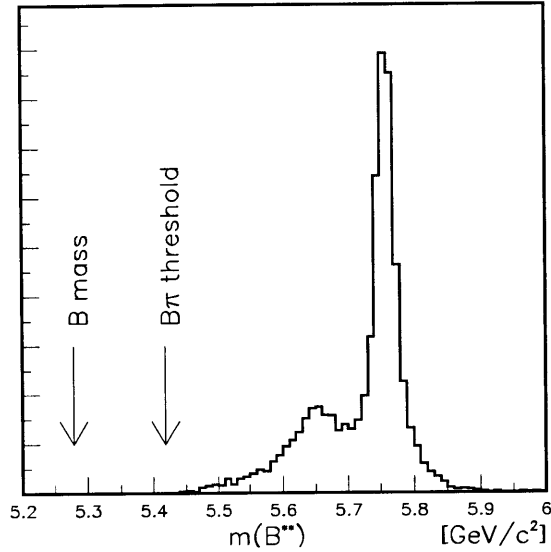
Figure 3-5: The generated $B(2P)$ invariant mass spectrum.

What we can do instead is look at the difference between the mass of the $B\pi$ system and the threshold for the decay:

$$Q(B,\pi) = m(B\pi) - m(B) - m(\pi).$$

In a sample of fully reconstructed B mesons, the B^{**} mass peak would have the same shape in Q but be shifted so that the $B\pi$ threshold is at $Q = 0$. We will therefore call the quantity Q the invariant mass as well, keeping in mind that it is actually a difference of masses.

To study whether we can see the B^{**} states in Q we have generated a sample of events containing them using the Monte Carlo described above. The invariant mass of the generated states is shown in figure 3-5.

The top plot in figure 3.3 shows the invariant mass Q of the B^{**} states found with fully reconstructed B mesons. We see that even if we find all B decay products, the
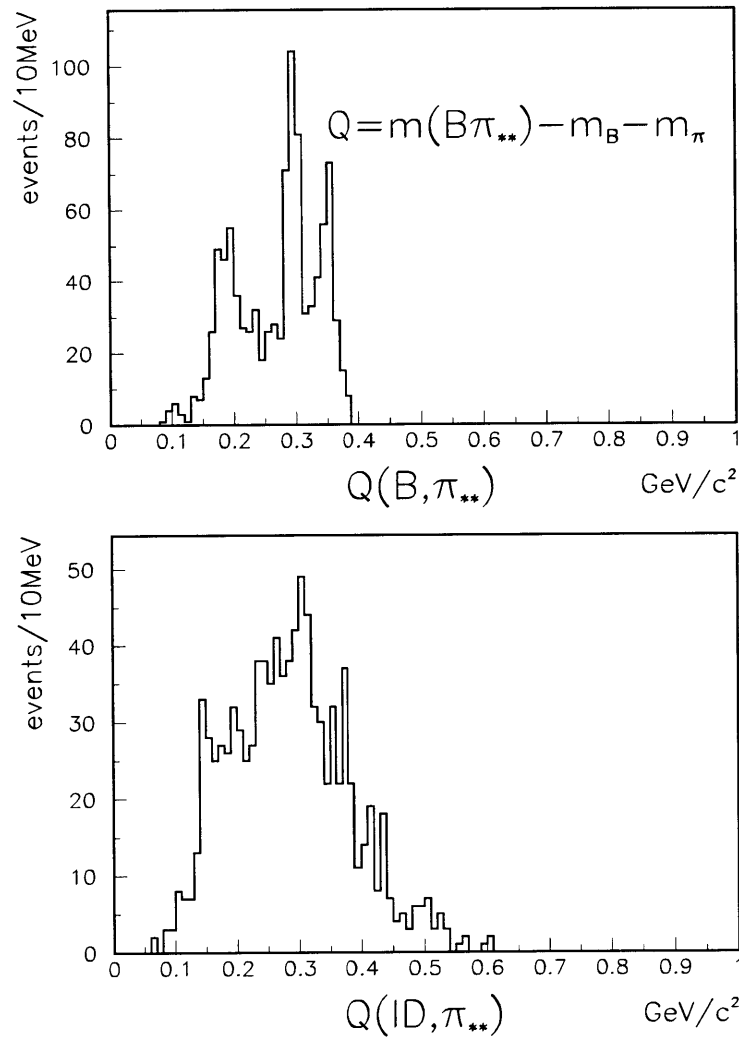
Figure 3-6: Reconstructed B^{**} invariant mass, measured relative to the threshold for $B\pi$ decay. The top plot shows the effect of the lost photon from $B^* \to B$ decays. At the bottom is the analogous quantity for partially reconstructed B mesons.

distribution is much less peaked than the generated B^{**} mass. The reason for this is the decay of B^{**} into B^*; about 73% of all $2P$ states decay through a B^*, and the photon from the subsequent $B^* \to \gamma B$ transition cannot be efficiently reconstructed at CDF.

Our B mesons are only partially reconstructed, so we must look at the quantity

$$Q(\ell D^{(*)}, \pi) = m(\ell D^{(*)} \pi) - m(\ell D^{(*)}) - m(\pi)$$

instead. The resulting shape of the B^{**} mass peak is shown in the bottom plot in figure 3.3. Clearly, the invariant mass resolution degrades considerably, but we see that the entire B^{**} mass peak is confined to a region of ~ 300 MeV/c^2—not a hopelessly wide window! We can even improve this resolution a little by estimating the best we can the momentum of the B before the decay, as described in the next section.

3.4   Correcting the Momentum of B Mesons

The loss of the neutrino systematically shifts the reconstructed B momentum. We can improve our estimate of the real B momentum by predicting this shift from the Monte Carlo and applying a correction to the measured momentum. This correction is often called the "$\beta\gamma$ correction", as it corrects the Lorentz boost $1/(\beta\gamma) \equiv m/\mathrm{p}$ of the B.

3.4.1   The Standard $\beta\gamma$ Correction

A B meson that lived a time t_{true} will have travelled the distance L_{xy} in the transverse plane before decaying. This distance is given by

$$ct_{true} = L_{xy} \frac{m(B)}{\mathrm{p_T}(B)}.$$

We do not know the momentum of the B, however, so when measuring the lifetime

of the B we approximate this by

$$ct_{true} \approx ct \equiv L_{xy} \frac{m(B)}{\mathrm{p_T}(\ell D)} \left\langle \frac{\mathrm{p_T}(\ell D)}{\mathrm{p_T}(B)} \right\rangle$$

where

$$\mathcal{K} \equiv \left\langle \frac{\mathrm{p_T}(\ell D)}{\mathrm{p_T}(B)} \right\rangle$$

is the average correction factor we get from the Monte Carlo. The $\mathcal{K}$ factor distribution turns out to have a mean of $\approx 85\%$ and an RMS of $\approx 11\%$, so the correction required is not very large. This is a consequence of the trigger requirement: events where the neutrino takes away a larger fraction of the B momentum are less likely to pass the trigger.

The fraction of the original B momentum retained by the ℓD system is plotted in figure 3-7. A simple $\beta\gamma$ correction would therefore just scale the ℓD momentum by the constant $\mathcal{K}$ factor so that the new distribution has a mean of one. Previous analyses ([40]) have shown, however, that the optimal correction factor is a function of the invariant mass of the ℓD system. Therefore, we use $\mathcal{K} = \mathcal{K}(m(\ell D))$. The B momentum distribution after such a correction is shown in figure 3-7 for comparison.

The average Q resolution for the B^{**} states and the systematic shift of their measured Q values for various $m(\ell D)$ ranges before ("Raw") and after ("$\beta\gamma$") such a correction are shown in figure 3.4.3. The improvement is considerable in the low $m(\ell D)$ range, and negligible in the high $m(\ell D)$ range. This is expected: a smaller $m(\ell D)$ means that the neutrino carried away more energy, thereby increasing the spread between the momentum of the B and its visible decay products. (Obviously, one way to improve the Q resolution without correcting the B momentum would be to cut out events with $m(\ell D)$ below a certain value. This, however, quickly reduces the size of the sample, and the $\beta\gamma$ correction makes it unnecessary.)
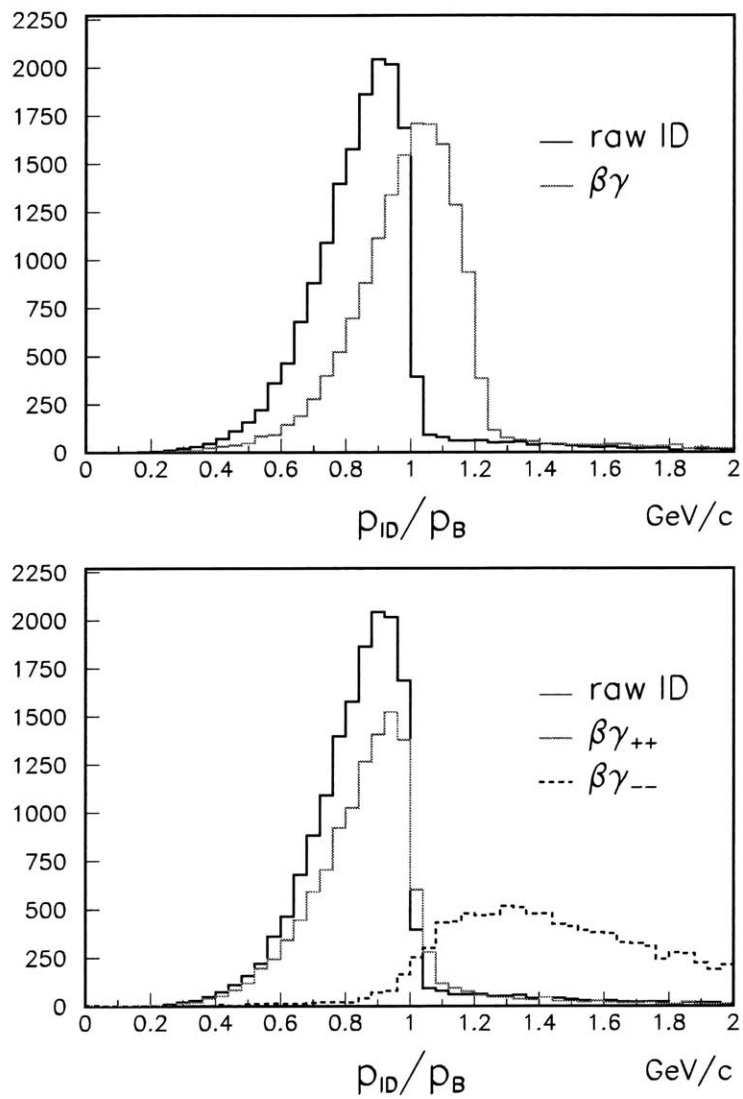
Figure 3-7: Fraction of the original B momentum carried by the ℓD system.

3.4.2 The Improved $\beta\gamma$ Correction

We also studied the possibility of calculating the B momentum from the properties of its visible decay products and the measured position of the secondary vertex. This procedure is described in appendix C. We call the resulting correction the "m_{T} correction." We decided against using it in this analysis because it has a relatively large intrinsic inefficiency—it rejects about a fifth of all B candidates. We did learn a valuable lesson from its study, however: the position of the secondary vertex contains information that can improve our estimate of the direction of the B momentum. Therefore, in the rest of this analysis, in place of the four-vector of the ℓD system, we use the following as the best estimate of the properties of the B meson before the decay:

- the magnitude of the momentum is set to the magnitude of the momentum of the ℓD system corrected by the $\beta\gamma$ correction factor K as described above;

- the direction of the momentum in the transverse plane is set to the direction of the secondary vertex;

- the pseudorapitidy is set to $\eta(\ell D)$;

- the mass is set to $m(B)$.

The Q resolution for B^{**} states reconstructed using such a constructed "particle" is shown in figure 3.4.3 under the label "$\beta\gamma$d." The improvement over applying only the standard $\beta\gamma$ correction is only slight, but it comes at no expense.

The expected B^{**} mass distributions after various corrections are shown in figures 3-8 and C-2.
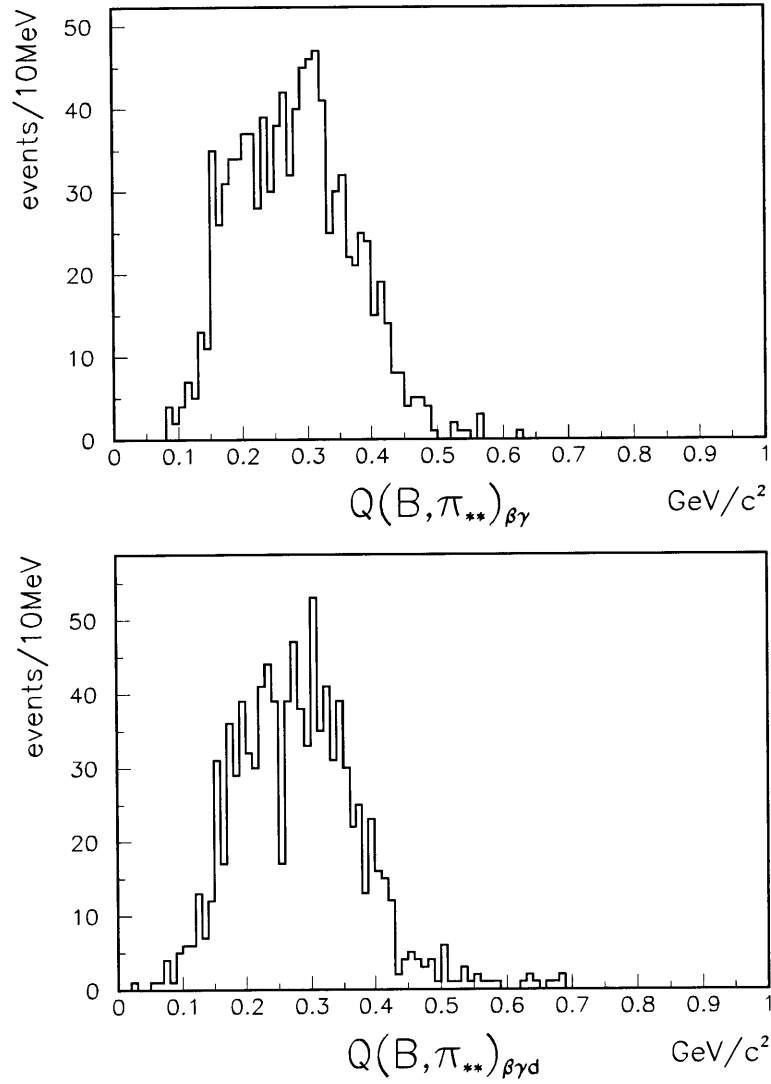
Figure 3-8: Reconstructed B^{**} invariant mass, measured relative to the threshold mass: (top) after $\beta\gamma$ correction, and (bottom) after correcting the direction of the B momentum.

74

3.4.3 Summary of B Momentum Corrections

Figure 3.4.3 summarizes the resolution on the invariant mass Q for B^{**} states using various B momentum estimators. The average resolution after applying the correction we use is about $50 \, \mathrm{MeV/c^2}$—a very encouraging result considering that we are missing a B decay product!
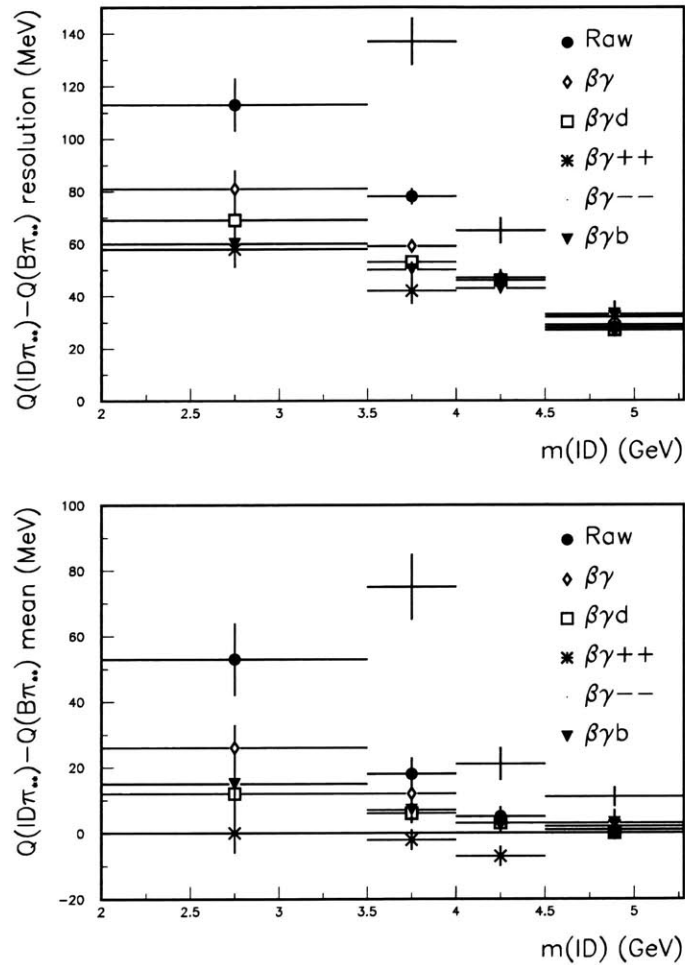
Figure 3-9: The resolution and the mean shift of the Q value for pions from B^{**} decay after various corrections of the ℓD momentum and direction.

Chapter 4

Sample Composition

The B mesons in our sample are not fully reconstructed. In addition to the obvious difficulty of having to approximate their original momentum based on the properties of their visible decay products, there is a much more involved complication inherent in this method of reconstruction: the exact flavor content of the decaying B meson cannot be deduced with certainty from its reconstructed fragments. We call this effect the "sample composition," emphasising the fact that a sample with a single decay signature contains events with B mesons of different flavors. Strictly speaking, this effect is just a special case of the "flavor mixing" discussed in section 6.2; this is, however, its most complicated instance, so it deserves special attention.

The cause of the "impure" sample composition is illustrated in figure 4-1. Other than the "direct" decay, in which a B decays into just the neutrino and the products we detect, there are a number of other decay chains that produce the same signature with one or more additional particles that escape undetected. The chains that feed a signature from a B flavor different from the one responsible for the direct decay we call "cross-talk."

4.1   Cross-Talk

The two most important mechanisms that result in cross-talk are (see figure 4-1):
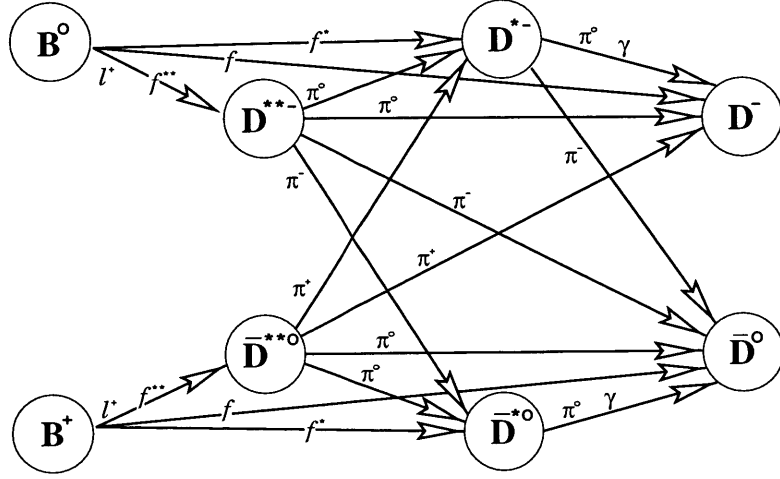
Figure 4-1: The relevant semileptonic B decay chains.

- **Inefficiency of the D^{*-} veto.** The decay signature

$$B^0 \to \nu\ell^+ D^{*-}, \quad D^{*-} \to \bar{D}^0 \pi_s^-$$

looks exactly like

$$B^+ \to \nu\ell^+ \bar{D}^0$$

if we fail to reconstruct the pion from D^{*-} decay. In the process of looking for $\ell^+\bar{D}^0$ signatures we perform a search for tracks that are compatible with a $D^{*-} \to \bar{D}^0\pi_s^-$ decay and reject all events where such a track is found; this is called the "soft pion veto" and is explained in chapter 3. This search is, however, not fully efficient: the efficiency for detecting the π_s^- we call $\epsilon(\pi_s)$ and calculate from the data as explained in section 4.2.4.

- **Higher excited states of D mesons.** The D meson mass spectrum closely resembles that of the B meson. In fact, in the $m_Q \to \infty$ limit the mass splittings between the ground and orbitally excited states are almost exactly the same in the B and D systems; the first-order difference in these splittings is introduced as $1/m_Q$ corrections in HQET (see chapter 1). We therefore have to take into

77

account the possibility that the B we are trying to reconstruct decayed into a D^{**} state,[1] which subsequently decayed into the fully reconstructed particles.

Just like in the B system, we expect two narrow and two broad D^{**} resonances. Unlike the B system, the D meson is produced in the decay of a B meson, not by hadronization of c quarks. That means we don't have to worry about production of associated hadronization particles. There is, however, a slight complication of a similar nature: the B meson can undergo a four-body decay, $B \to \nu\ell D^{(*)}\pi$, which is topologically identical to the production and decay of a D^{**} resonance (since D^{**} doesn't travel an appreciable distance in our detector); to distinguish it from the resonant $D^{(*)}\pi$ production, we call this process *non-resonant.*

To date there is experimental evidence ([22]) for the production of the two narrow D^{**} states, $D_1(2420)$ and $D_2^*(2460)$. The two broad states have not been identified yet, and are expected to be indistinguishable from the non-resonant four-body B decays within the available datasets. For this reason, an attempt to reconstruct and remove the D^{**} states from our samples could not employ the $D^{(*)}\pi$ invariant mass peaks, but rather would have to rely on the topological selection of tracks originating at the B decay vertex. We do not attempt any such selection; we calculate instead the expected cross-talk using the expected properties of B decays, as explained below. In the rest of this analysis we will use the label D^{**} for *all* $B \to \nu\ell D^{(*)}\pi$ decays, resonant and non-resonant alike.

4.2   Sample Composition Parameters

Given the diagram in figure 4-1, our goal is to find a minimal set of parameters that describes the relative abundance of all the decay chains shown. These parameters are called the "sample composition parameters" because they tell us the fraction of $\ell D^{(*)}$

---

[1]We neglect here the decays into even higher states, like the radially excited $D(2S)$ for example.

events in a particular signature that came from a B^0 or a B^+. The next four sections will introduce and quantify the most important effects.

4.2.1 Decays Through Excited D States

We first turn our attention to the decay chains that proceed through D^{**} states. Looking at figure 4-1, we need three parameters to fully quantify B decays through D^{**} states.

- The first parameter is the *fraction* of B mesons that decay into a D^{**} state, labelled f^{**}:

$$f^{**} \equiv \frac{\mathcal{B}(B \to \nu\ell D^{**})}{\mathcal{B}(B \to \nu\ell DX)} \tag{4.1}$$

  This number is poorly constrained from direct measurements. Recall, however, that our definition of "D^{**}" includes the non-resonant four-body B decays and that we neglect the decays to higher excited D states. We can therefore write

$$f^{**} + f^* + f = 1 \tag{4.2}$$

  where f^* and f are numbers analogous to f^{**} for decays into D and D^* (also shown in the figure). From reference [38] we get

$$\mathcal{B}(B \to \nu\ell D) \ = \ 1.7 \pm 0.5 \tag{4.3}$$

$$\mathcal{B}(B \to \nu\ell D^*) \ = \ 4.4 \pm 0.7 \tag{4.4}$$

$$\mathcal{B}(B \to \nu\ell DX) \ = \ 9.6 \pm 1.6 \tag{4.5}$$

  so we use $f^{**} = 0.36 \pm 0.12$.

- The second parameter is the fraction of D^{**} states that decay through a charged pion (thus contributing to the cross-talk). Strong isospin arithmetic sets this fraction to 2/3.

79

- The third parameter is the fraction of D^{**} states that decay into a vector state:

$$P_V \equiv \frac{\mathcal{B}(B \to D^{**} \to D^*\pi)}{\mathcal{B}(B \to D^{**} \to D^*\pi) + \mathcal{B}(B \to D^{**} \to D\pi)} \qquad (4.6)$$

Of the four D^{**} resonances, the $J = 0$ can only decay into $D\pi$, the two $J = 1$ states can only decay into $D^*\pi$, and the $J = 2$ can go both ways with branching ratios given by spin counting and the available phase space. P_V is then an effective quantity describing the division of $B \to D^{**}$ decay chains in our sample among the four D^{**} states. At first glance, this division is given simply by spin counting. After closer inspection, however, the matters turn out to be significantly complicated by the trigger requirement, as described in the next section. In this analysis we use the value $P_V = 0.33 \pm 0.28$ which was measured in the same data sample as described in reference [40].

The remaining B mesons decay to either a D or a D^*. Looking at equation 4.2, it is obvious that we need only two variables to describe the B branching fractions into D^{**}, D^* and D mesons. We use f^{**} and the ratio of the other two branching fractions:

$$R_f = \frac{f^*}{f} \qquad (4.7)$$

Equations 4.3 and 4.4 give us $R_f = 2.5 \pm 0.6$.

To calculate the sample composition, we need, for each signature, to sum up the branching fractions of all the decay chains that contribute to that signature, and from those numbers calculate the fraction of B^0 and B^+ mesons.

For example, table 4.1 lists all the decay chains that can produce the $B \to \ell\nu D^{*-}X$ signature. The compact notation for labelling chains, shown in the column labelled "code" in the table, is described in appendix D. In the following equations we will use the index ℓ to denote a single decay chain (*e.g.* in the D^{*-} case shown here, ℓ can be [100.221], [121.221] or [212.221]). Similarly, we will use the index k to denote a single decay signature, *i.e.*, k can be any of the six signatures described in chapter 3 and appendix B.

80

code	decay chain	$\phi_{k\ell} \equiv \frac{\mathcal{B}_{k\ell}}{\mathcal{B}(B \to \nu\ell X)}$
100.221	$B^0 \to \nu\ell^+ D^{*-}$	f^*
121.221	$B^0 \to \nu\ell^+ D^{**-}$, $D^{**-} \to D^{*-}\pi^0$ (lost π^0)	$\frac{1}{3}f^{**}P_V$
212.221	$B^+ \to \nu\ell^+ \overline{D}^{**0}$, $\overline{D}^{**0} \to D^{*-}\pi^+$ (lost π^+)	$\frac{2}{3}f^{**}P_V$

Table 4.1: The B decay chains that contribute to the ℓD^{*-} decay signatures, and their relative contributions.

The branching fraction for a single decay chain relative to the total B semileptonic branching fraction we call $\phi_{k\ell}$:

$$\phi_{k\ell} \equiv \frac{\mathcal{B}_{k\ell}}{\mathcal{B}(B \to \nu\ell X)} \tag{4.8}$$

We can also define the total branching fraction of a B flavor into a specific signature,

$$\Phi_k^0 \equiv \frac{\mathcal{B}(B^0 \to \text{``}k\text{''})}{\mathcal{B}(B^0 \to \nu\ell X)} \tag{4.9}$$

$$\Phi_k^+ \equiv \frac{\mathcal{B}(B^+ \to \text{``}k\text{''})}{\mathcal{B}(B^+ \to \nu\ell X)} \tag{4.10}$$

and express these in terms of $\phi_{k\ell}$:

$$\Phi_k^0 = \sum_{B^0 \to \ell} \phi_{k\ell} \tag{4.11}$$

$$\Phi_k^+ = \sum_{B^+ \to \ell} \phi_{k\ell} \tag{4.12}$$

where the label $B^0 \to \ell$ means that the sum goes over all decay chains that originate from B^0, and similarly for B^+.

Finally, the sample composition is:

$$\text{fraction of } k \text{ from } B^0 = \frac{\Phi_k^0}{\Phi_k^0 + \Phi_k^+} \tag{4.13}$$

$$\text{fraction of } k \text{ from } B^+ = \frac{\Phi_k^+}{\Phi_k^0 + \Phi_k^+} \tag{4.14}$$

4.2.2 Relative Charm Reconstruction Efficiencies

The phase space available for the semileptonic decay of a B meson depends on the mass of its decay products. The lepton and the neutrino are common to all the decay chains we are considering, but the different states of D mesons have significantly different masses. In addition, the density of the distribution of B decay products in the phase space depends on the spin of the D meson. The angular momentum of the D states we are encountering can be 0, 1 or 2, so we expect significantly different spectra of the detected particles from different decay chains.

The first requirement a semileptonic B event has to satisfy in order to end up in our data sample is that the lepton passes the trigger. The electron trigger has a turn-on near $p_T^e = 7.5\,\mathrm{GeV}/c$ and the muon trigger near $p_T^\mu = 9\,\mathrm{GeV}/c$ (see section 3.2.1). This is by far the largest source of "inefficiency" for detecting semileptonic B decays, and any difference in the momentum spectrum of leptons is bound to have a large effect on the total detection efficiency. In addition to the trigger requirement, we impose various cuts on the other B decay products (see appendix B). All this means that we have to calculate the efficiency for detecting each decay chain from the Monte Carlo, and incorporate that knowledge in the calculation of sample composition.

The straightforward way of accomplishing this is to rewrite equations 4.11 and 4.12 as

$$\Phi_k^0 = \sum_{B^0 \to \ell} \phi_{k\ell}\epsilon(k\ell) \tag{4.15}$$

$$\Phi_k^+ = \sum_{B^+ \to \ell} \phi_{k\ell}\epsilon(k\ell) \tag{4.16}$$

where $\epsilon(k\ell)$ is the efficiency[2] for detecting the signature k if it originated in decay chain ℓ.

A big problem with this plan, however, is that the absolute individual efficiencies depend on a number of parameters that are not modelled very well (or not at all) in the

---

[2] For brevity, throughout this work we use the term "efficiency" to denote the product of kinematic acceptance and detector efficiency for one or more particles.

Monte Carlo (such as detector aging effects, for example). We can solve this problem by noting that every signature has one "direct" decay chain, the one where we detect all the particles except the neutrino ([100.221] for the ℓD^{*-} signature, see table 4.1). Looking at the equations 4.13 and 4.14, we see that we can divide all the absolute efficiencies by the absolute efficiency for the direct chain without changing the form of the equations. The efficiencies we get in this way are then measured relative to the direct chain, so we name them "relative charm reconstruction efficiencies." In the process of division most of these poorly understood effects cancel out, which reinforces our confidence in the Monte Carlo results.

Putting this into symbols, relative charm reconstruction efficiency $\epsilon_{k\ell}^D$ is

$$\epsilon_{k\ell}^D \equiv \frac{\epsilon(k\ell)}{\epsilon(kd)} \tag{4.17}$$

where ϵ_{kd} is the absolute efficiency for the direct chain, $\ell = d$. By this definition, $\epsilon_{kd}^D = 1$. We can then write

$$\Phi_k^0 = \sum_{B^0 \to \ell} \phi_{k\ell} \epsilon_{k\ell}^D \tag{4.18}$$

$$\Phi_k^+ = \sum_{B^+ \to \ell} \phi_{k\ell} \epsilon_{k\ell}^D \tag{4.19}$$

The relative charm reconstruction efficiencies for all the decay chains and all the signatures are listed in appendix E. We calculated them by running the Monte Carlo simulation described in section 3.2 and comparing the number of generated and detected events for each decay chain in every signature. Some of the efficiencies are significantly different from 1. A breakdown by the requirements that failed indicates that most of this effect is caused by the lepton trigger, and very little by the D selection requirements.

4.2.3 Difference Between $\tau(B^0)$ and $\tau(B^+)$

This analysis relies on the assumption that the production rates of B^0 and B^+ mesons are equal. While this assumption itself is very well tested, there is still a possibility that the branching fractions of different B flavors into the decay chains we detect are not equal. One mechanism that could cause this inequality is a difference in hadronic decay widths of the two B flavors.

The semileptonic B decays are well described using the "spectator" model, according to which the b quark undergoes the weak decay, and the light quark is just a spectator—it doesn't affect the rate of the weak decay. Consequently, the total semileptonic decay width in this model doesn't depend on the flavor of the light quark. If, however, the hadronic B decays proceed at different rates, then the total number of semileptonic decays we observe will be different for the two flavors, since the hadronic decays will "steal" more mesons from one flavor than from the other.

The total B decay width is the sum of the semileptonic and the hadronic width, $\Gamma_{tot} = \Gamma_{sl} + \Gamma_{had}$. The quantity of interest to us is the ratio of the semileptonic branching fractions, $\mathcal{B}_{sl} = \Gamma_{sl}/\Gamma_{tot}$. Using $\Gamma_{tot} = \hbar/\tau$ we can express this ratio as the ratio of lifetimes of the two flavors:

$$\frac{\mathcal{B}_{sl}(B^+)}{\mathcal{B}_{sl}(B^0)} = \frac{\Gamma_{sl}(B^+)/\Gamma_{tot}(B^+)}{\Gamma_{sl}(B^0)/\Gamma_{tot}(B^0)} = \frac{\Gamma_{tot}(B^0)}{\Gamma_{tot}(B^+)} = \frac{\tau_{B^+}}{\tau_{B^0}} \tag{4.20}$$

This means that the ratio of the measured lifetimes of the two B flavors gives us the size of their relative contribution to the observed semileptonic B decays. Recalling that equations 4.18 and 4.19 describe the relative contributions of various decay chains originating at a B^0 or a B^+, we can rewrite them as

$$\Phi_k^0 = \tau_{B^0} \sum_{B^0 \to \ell} \phi_{k\ell} \epsilon_{k\ell}^D \tag{4.21}$$

$$\Phi_k^+ = \tau_{B^+} \sum_{B^+ \to \ell} \phi_{k\ell} \epsilon_{k\ell}^D \tag{4.22}$$

and preserve the forms of equations 4.13 and 4.14.

84

The current world-average value of the ratio of B^0 and B^+ lifetimes is consistent with one,

$$\frac{\tau_{B^+}}{\tau_{B^0}} = 1.02 \pm 0.05$$

but we include this parameter in the calculation of the sample composition so that its measurement error contributes to the total systematic uncertainty.

4.2.4 Calculating $\epsilon(\pi_s)$ from the Data

As we mentioned earlier, limitations of the detector and of the particle-finding algorithms result in a loss of some of the pions from the decay $D^{*-} \to \bar{D}^0 \pi_s^-$ even though we fully reconstruct the $\bar{D}^0$. The events containing a $B^0 \to \nu \ell^+ D^{*-}$ decay where this happens will end up in our $B^+ \to \nu \ell^+ \bar{D}^0$ sample, thus contributing to the cross-talk. To quantify this contribution, in addition to the various branching fractions from figure 4-1 we also need to know the efficiency for finding the pion from D^{*-} decay, $\epsilon(\pi_s)$.

The $D^{*-} \to \bar{D}^0 \pi_s^-$ decay is very close to the kinematic threshold—the energy of the pion is only about $40\,\mathrm{MeV/c^2}$ in the D^{*-} rest frame—so the momentum of the pion in the detector is mostly determined by the velocity of the D^{*-} meson in the laboratory frame of reference, i.e. these pions typically have very low momentum (are "soft," hence the subscript s). Unfortunately, the detector response for soft tracks is poorly understood, so the determination of $\epsilon(\pi_s)$ from the Monte Carlo calculation is ridden with difficulties. For this reason, we calculate this efficiency from the data.

We start by noticing that the selection of $D^{*-} \to \bar{D}^0 \pi_s^-$ signatures starts from a sample of $\bar{D}^0$ signatures without the soft pion veto. The veto consists of looking for any track that forms a D^{*-} candidate with the reconstructed $\bar{D}^0$ candidate; events that pass the veto we take as $B^+ \to \nu \ell^+ \bar{D}^0$ candidates, and of the remaining events we choose the ones where the soft pion passes more stringent quality requirements as

$B^0 \to \nu \ell^+ D^{*-}$ candidates. We can define the quantity

$$R^{*(meas)} = \frac{N(\ell D^0, \text{fail veto})}{N(\ell D^0, \text{total before veto})} \qquad (4.23)$$

which is simply the fraction of events from the original $\bar{D}^0$ data sample that are removed by the veto. The data gives us $R^{*(meas)} = 0.249 \pm 0.008$.

The final step is to figure out the fraction of events in the original $\bar{D}^0$ data sample that *should have been* removed by the veto. We call this quantity R^*. In other words, $R^{*(meas)} = \epsilon(\pi_s) R^*$. This number can be calculated from the other sample composition parameters by noting that $N(\ell D^0, \text{total before veto})$ is simply the sum of all $\phi_{k\ell}$ that lead to the ℓD^0 signature (see appendix D), and $N(\ell D^*) \equiv N(\ell D^0, \text{should have failed veto})$ is the sum over the decay chains that proceed through a D^{*-}, that is [100.221], [121.221] and [212.221], but *without* the $(1 - \epsilon(\pi_s))$ factor, explicitly

$$
\begin{aligned}
R^* &= \frac{1}{\Phi^0 + \Phi^+} \left[\frac{2}{3} f^{**} P_V \mathcal{B}(D^{*+} \to D^0 \pi^+) \epsilon^D_{100.221} \tau_{B^0} \right. \\
&+ f^* \mathcal{B}(D^{*+} \to D^0 \pi^+) \epsilon^D_{121.221} \tau_{B^0} \\
&+ \left. \frac{1}{3} f^{**} P_V \mathcal{B}(D^{*+} \to D^0 \pi^+) \epsilon^D_{212.221} \tau_{B^+} \right]
\end{aligned}
\qquad (4.24)
$$

Using the central values of the other sample composition parameters (see table 4.3) and the measured value of $R^{*(meas)}$ we get $\epsilon(\pi_s) = 0.74 \pm 0.02$. The error on this number doesn't include the systematic uncertainty on the other sample composition parameters; to properly account for the correlations between all the parameters we let their values float in the fit, as will be explained in chapter 6, so the actual value of $\epsilon(\pi_s)$ is continually being recalculated to agree with the current values of the other parameters. This changing of $\epsilon(\pi_s)$, of course, only reflects changes in the predicted value of R^*, since $R^{*(meas)}$ is measured independent of sample composition.

4.3 Summary of Sample Composition

In summary, we calculate the sample composition as

$$\text{fraction of } k \text{ from } B^0 = \frac{\Phi_k^0}{\Phi_k^0 + \Phi_k^+}$$

$$\text{fraction of } k \text{ from } B^+ = \frac{\Phi_k^+}{\Phi_k^0 + \Phi_k^+}$$

where Φ_k^0 and Φ_k^+ are total contributions to the decay signature k from decay chains originating from B^0 and B^+ mesons respectively.

Φ_k^0 and Φ_k^+ are calculated as

$$\Phi_k^0 = \tau_{B^0} \sum_{B^0 \to \ell} \phi_{k\ell} \epsilon_{k\ell}^D$$

$$\Phi_k^+ = \tau_{B^+} \sum_{B^+ \to \ell} \phi_{k\ell} \epsilon_{k\ell}^D$$

where $\phi_{k\ell}$ is the relative abundance of the decay chain ℓ, $\epsilon_{k\ell}^D$ is its reconstruction efficiency relative to that of the direct chain for the signature k, and τ_B is the lifetime of the B meson whose decay chains the sum runneth over.

Values of $\phi_{k\ell}$ and $\epsilon_{k\ell}^D$ for all decay chains are listed in appendices D and E respectively. The other sample composition parameters are summarized in table 4.3.

Parameter	Value	Source
f^{**}	0.36 ± 0.12	[38]
R_f	2.5 ± 0.6	[38]
τ_{B^+}/τ_{B^0}	1.02 ± 0.05	[32]
P_V	0.33 ± 0.28	[40]
$R^{*(meas)}$	0.249 ± 0.008	measured in the data
R^*		calculated from other SC parameters
$\epsilon(\pi_s)$		$R^{*(meas)}/R^*$

Table 4.2: Summary of the sample composition parameters.

Chapter 5

Backgrounds

As explained in chapter 3, a data sample was extracted that contains a number of B mesons. Our goal is to measure, by counting the pions from B^{**} decay, what fraction of those mesons come from a B^{**} state. In order to proceed two complications need to be resolved: first, not all events in the sample have a B meson, and second, not all prompt pions in those events that do contain a B come from B^{**} decay. This chapter concentrates on the treatment of these backgrounds. A two-letter identifier is assigned to each type of background; these identifiers will be used in the following chapters.

5.1 NB: Fake B Events

The treatment of non-B events is straightforward: we separate the events that fall into the signal and sideband regions of the D mass peaks (figure 3.1.1), and subtract the appropriately scaled distributions for the sidebands from the ones for the signal region.

This background is highly dependent on the particular decay signature—track combinatorics are different—so we have to do the subtraction separately in each signature.

5.2 PU: Pile-Up Events

Pile-ups are events with more than one primary vertex. In CDF Run 1 the number of hard interactions per beam crossing was considerably greater than one, so we expect that a significant number of secondary (tertiary, *etc.*) $p\bar{p}$ collisions occurred so close to the $b\bar{b}$ primary vertex that we can't distinguish the two.

Distance in z from Primary Vertex (Data)

χ^2/ndf	235.2 / 91
P1	0.1281E+05
P2	0.6692E-01
P3	0.9892
P4	5651.
P5	0.1111E-01
P6	2.194
P7	4937.
P8	0.2894
P9	20.04
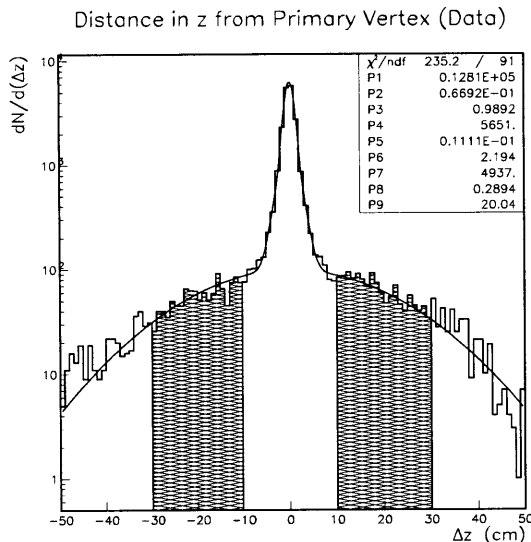
Figure 5-1: The $dN/d(\Delta z)$ distribution of tracks in B events. The narrow peak at $|\Delta z| = 0$ characterizes our z resolution. The wide (20 cm Gaussian) background is attributed to tracks from other $p\bar{p}$ collisions.

The properties of tracks coming from pile-ups are discussed in some detail in reference [44]. Here we handle them in essentially the same way: we make the relevant distributions with tracks that originate far in z (the "Δz sidebands") from the primary vertex closest to the B meson, and subtract them from the distributions for tracks near that vertex (the "Δz signal"). How to choose the Δz signal and sideband regions is obvious from figure 5-1. Tracks coming from the same primary vertex as the B meson form a narrow ($\sigma \approx 1\,cm$) peak at $\Delta z = 0$. The wide distribution under the peak we attribute to tracks from other $p\bar{p}$ collisions, fit a Gaussian shape to it, and from the fitted parameters choose the signal region ($|\Delta z| < 5\,cm$) and two sidebands

89

(shaded, $10\,cm < |\Delta z| < 30\,cm$).

Pile-ups are totally uncorrelated with B production, so their contribution to our distributions doesn't depend on the flavor or kinematic properties of the B meson. This means we can measure the contribution on the entire sample, and apply the combined result to specific decay signatures.

5.3 UE: Underlying Event in B Events

$p\bar{p}$ collisions that produce B mesons will necessarily produce a plethora of other particles. Some of these particles are the result of painting the b quark white; these are often called b fragmentation tracks, but here we refer to them as b *hadronization* tracks to distinguish them from products of fragmentation of other color strings. These particles are concentrated in a narrow cone around the direction of the observed B meson. Everything else that comes out of the same collision we call the "underlying event."
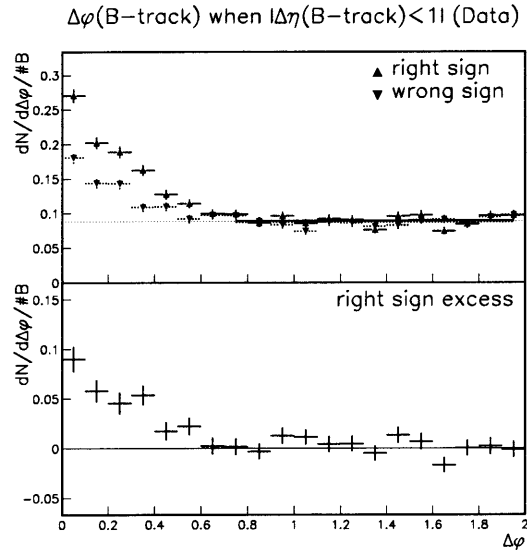
Figure 5-2: The $dN/d(\Delta\phi)$ distribution of tracks close in η to the B mesons.
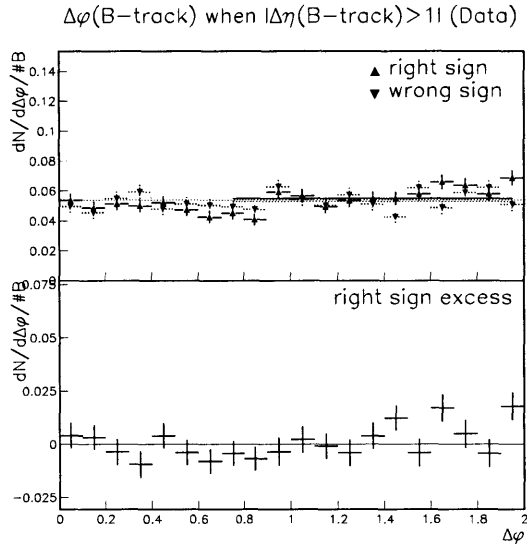
Figure 5-3: The $dN/d(\Delta\phi)$ distribution of tracks far in η from the B mesons.

There are different ways to produce an underlying event particle. The two mechanisms simulated in the Monte Carlo we use are beam remnants and multiple interactions. Beam remnants are colored leftovers of the proton and the antiproton that hosted the primary hard scattering. The breakup of the associated color strings will result in production of particles that occasionally end up near the observed B mesons. Multiple interactions are hard scatterings between other pairs of partons in the same $p\bar{p}$ collision, occurring independently of the scattering that produces the b quarks. It is important to note that both these mechanisms will produce particles that are uncorrelated with the B meson to first order.

To estimate the contribution of this background to our distributions, we first need to find a segment of space populated only with the underlying event particles. In our studies we found out that we cannot use minimum-bias events (which were traditionally the favorite candidate for estimating the underlying event), but rather have to rely on B events. This is documented in some detail in reference [44]; here we repeat only the few relevant results.

Briefly, looking at the $dN/d(\Delta\phi)$ distribution of tracks in B events (figure 5-

2), we can clearly see the excess of tracks near the B meson, in the $|\Delta\phi| < 0.6$ region, and a flat distribution further away. The flat region is a very good candidate for measurement of the underlying event, but first we have to make sure it really describes well the tracks closer to the meson. To do this, we plot the same $dN/d(\Delta\phi)$ distribution for tracks that are far in η from the B (figure 5-3). The flatness of this distribution means that we can safely use the tracks from the flat region in figure 5-2 to estimate what the underlying event will look like under the meson. It is clear how to proceed: we rotate the tracks that are in the $1 < |\Delta\phi| < 2$ region under the B, and use their distributions as the best estimate of the underlying event.

Since we define the underlying event as everything coming out of the same collision that is *not* correlated with the B, we can measure its contribution on the entire sample, like the pile-ups, and apply that result to specific decay signatures.

5.4   HA: *b* Hadonization Products

As their name suggests, the "*b* hadronization products" originate in the process of hadronization of *b* quarks. They come from the primary vertex and are correlated with the B direction (they appear in a narrow cone around the meson) and flavor. Since the decay of the B^{**} is strong as well, these tracks are almost indistinguishable from the pions from B^{**} decay—the only difference is kinematical, hadronization tracks being non-resonant.

This is our dominant background, and unfortunately the least well understood one. We devote the entire section 6.6.1 to it.

5.5   BD: *B* Decay Products

In the process of selecting B candidates, we do not attempt to reconstruct any B decay products other than the lepton and the $D^{(*)}$ daughters. We expect that a certain fraction of B mesons decays through a D^{**}, or directly into $\nu\ell D\pi$, the four-

body decay. Pions from the decay of the D^{**}, or from the four-body decay, come from the B vertex, but a significant portion will appear to have passed through the primary vertex as well. Unlike the pions from the B^{**} decay, these will appear non-resonant in the B reference frame even if they come from a narrow D^{**} resonance.

The shape of this contribution we get from a Monte Carlo calculation. The normalization and charge correlation with the B flavor depend on properties of B decays that are not known very well, so the parameters that determine the final shape we leave floating in the fit. This is explained in more detail in chapter 6 and reference [40].

5.6 Optimizing the Search

The selection requirements we apply to B^{**} decay products affect the shape of the mass peak we expect to see. On the B meson side, the requirement that the lepton pass the trigger is by far the greatest determinant of the distributions of B mesons we detect. The pion from the B^{**} decay, on the other hand, is relatively unbiased, the only requirements so far being that it is compatible with coming from the primary vertex nearest the B meson, and that it passes some basic track quality cuts.

If our goal were to select as many B^{**} candidates as possible, there would clearly be a lot of room for improvement: we could apply a number of topogical cuts, for example on the opening angle between the meson and the pion, or on the decay angle in the rest frame of the meson. Since our understanding of backgrounds is far from perfect, however, we are loath to apply any cuts that could bias the invariant mass distribution.

One of the few "safe" requirements we can apply is the transverse momentum cut on the candidate track. In order to maximize the significance of the signal, we want to choose the value to cut on such that the quantity $S^2/(S + B)$ is maximized. Here S is the expected number of signal tracks, and B is the expected number of background tracks under the signal (i.e., in the region below $500\,\mathrm{MeV/c^2}$). The left plot in figure 5-4 shows how this quantity changes in the Monte Carlo as we vary

93
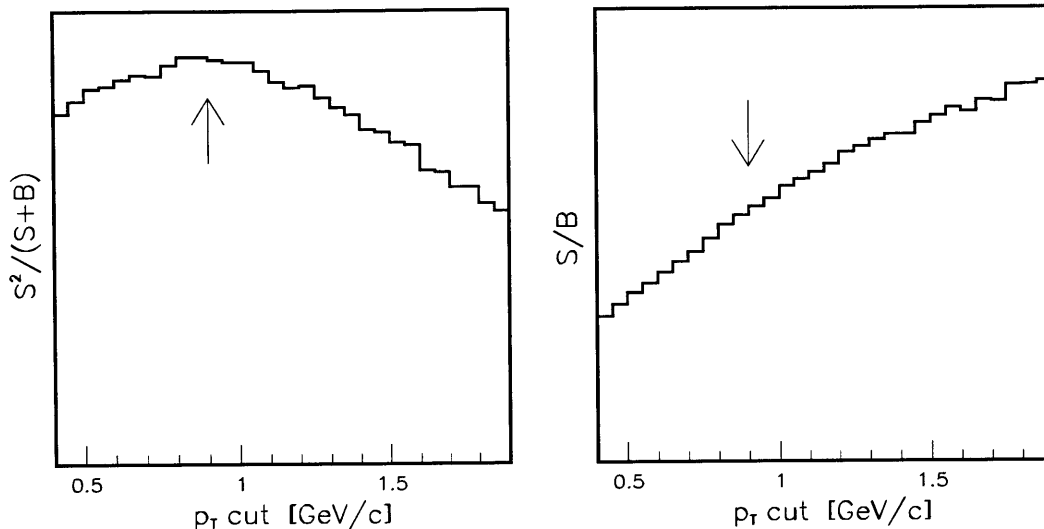
Figure 5-4: $S^2/(S + B)$ and signal-to-background ratio as a function of the p_T cut on the candidate track. The arrows show the value we choose to cut on.

the p_T cut (the right side of the figure shows the change in the signal-to-background ratio). We require that the track p_T be greater than 900 MeV/c.

5.7 Combining the Components

Of all the backgrounds we listed, only the b hadronization tracks and the B decay products are correlated with B mesons. The other, "uncorrelated," backgrounds we get from elsewhere in the data and subtract their distributions from the signal distributions to account for the expected impurities in the signal region.

The key to combining the uncorrelated backgrounds is noticing that each uncorrelated component contains all the others as its own backgrounds. Therefore, we have to subtract the distributions for the D sidebands from the ones for the D signal, and also the ones for the Δz sidebands from the ones for the Δz signal, but then we also have to *add* the distribution for the D sidebands *and* Δz sidebands to the result. Clearly, we have to apply the equivalent procedure to the underlying event distributions before we subtract them from the signal.

94

The Q distributions seen in the data for D and Δz signal and sideband regions are shown in figures 5-5 through 5-10 for each decay signature. The top four plots in these figures are the normal Q spectra of tracks around B candidates. The bottom four plots, on the other hand, are the estimated Q spectra of the underlying event, obtained from rotated tracks as explained earlier. If we label the four rows of histograms in the figures with numbers 1 through 4 starting from the top, and the two columns as L and R, then in order to implement the background-subtraction procedure from the last paragraph we perform the following histogram arithmetic:

$$L1 - R1 - (L2 - R2) - (L3 - R3 - (L4 - R4)).$$

Figure 5-11 shows the resulting distributions in the two decay signatures with the most B candidates. The plot on the left side is the $\bar{D}^0 \rightarrow K^+\pi^-$ signature, which contains mostly charged B mesons. The plot on the right side is the $D^{*-} \rightarrow \bar{D}^0\pi_s^-$, $\bar{D}^0 \rightarrow K^+\pi^-\pi^0$ signature, which conatins mostly neutral B mesons. The difference between the two is striking at the first glance. Around the charged mesons we see a large excess of right-sign tracks in the region where we expect the signal to be, but around neutral mesons there is hardly any excess at all. This turns out to be caused by an interplay of several factors, and to fully explain it we need the concepts explained in the following sections. We return to this phenomenon at the end of section 6.6.1.

Kπ Data
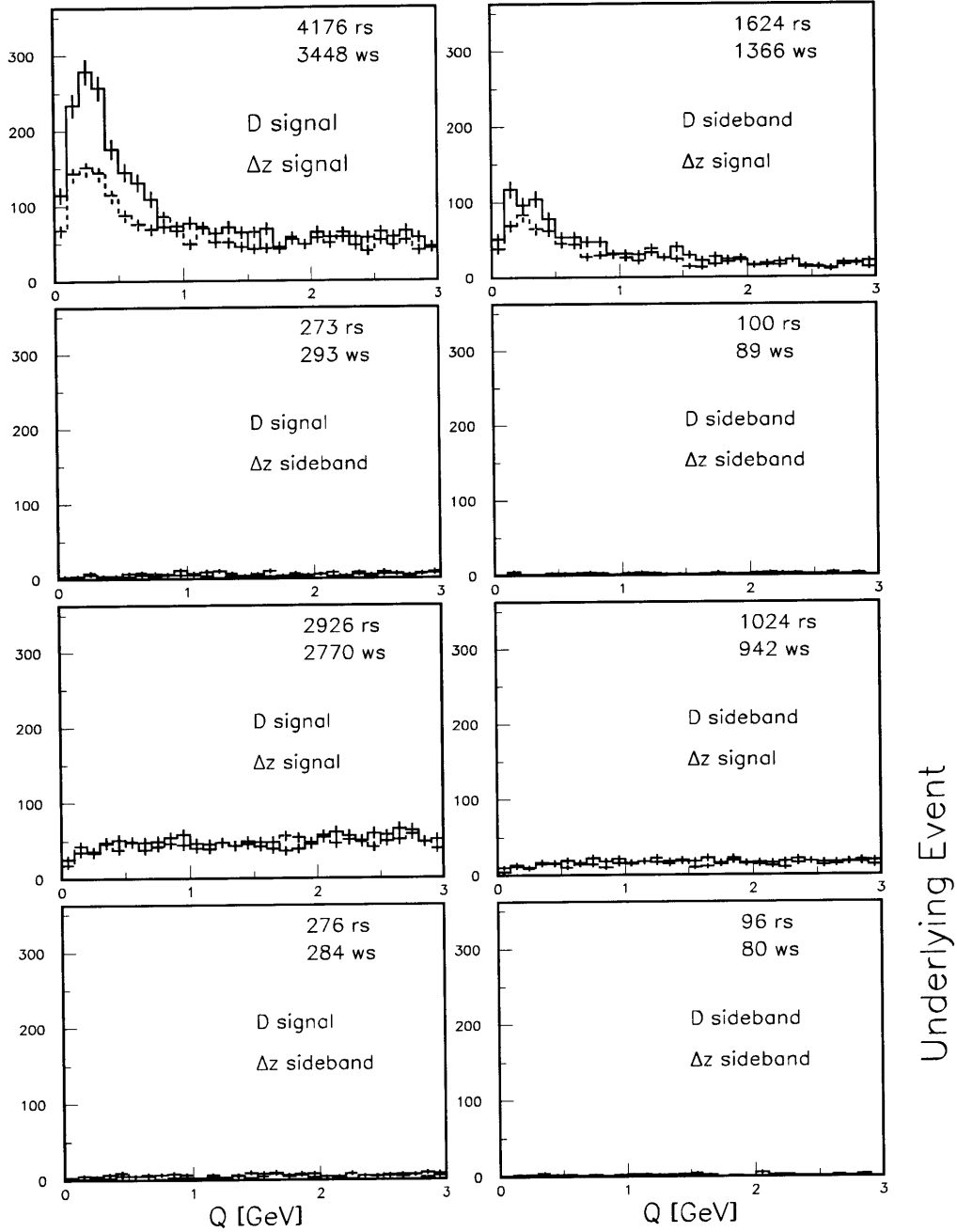
Figure 5-5: The Q spectrum of the B-$track$ combinations seen in the $\bar{D}^0 \rightarrow K^+\pi^-$ data. The solid (dashed) histograms are the right-sign (wrong-sign) combinations.

K3π Data
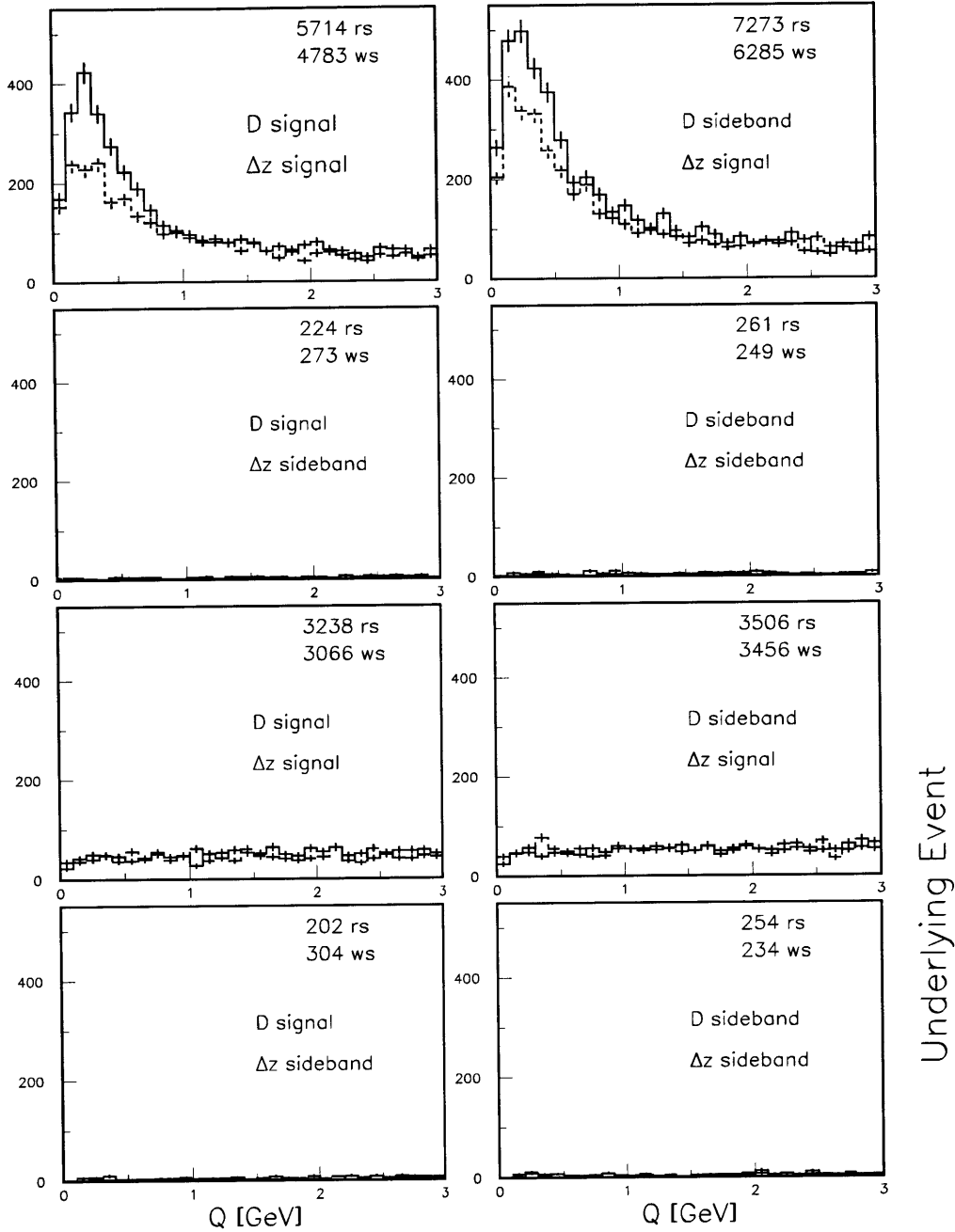
Figure 5-6: The Q spectrum of the *B-track* combinations seen in the $\bar{D}^0 \rightarrow K^+\pi^-\pi^+\pi^-$ data. The solid (dashed) histograms are the right-sign (wrong-sign) combinations.

97
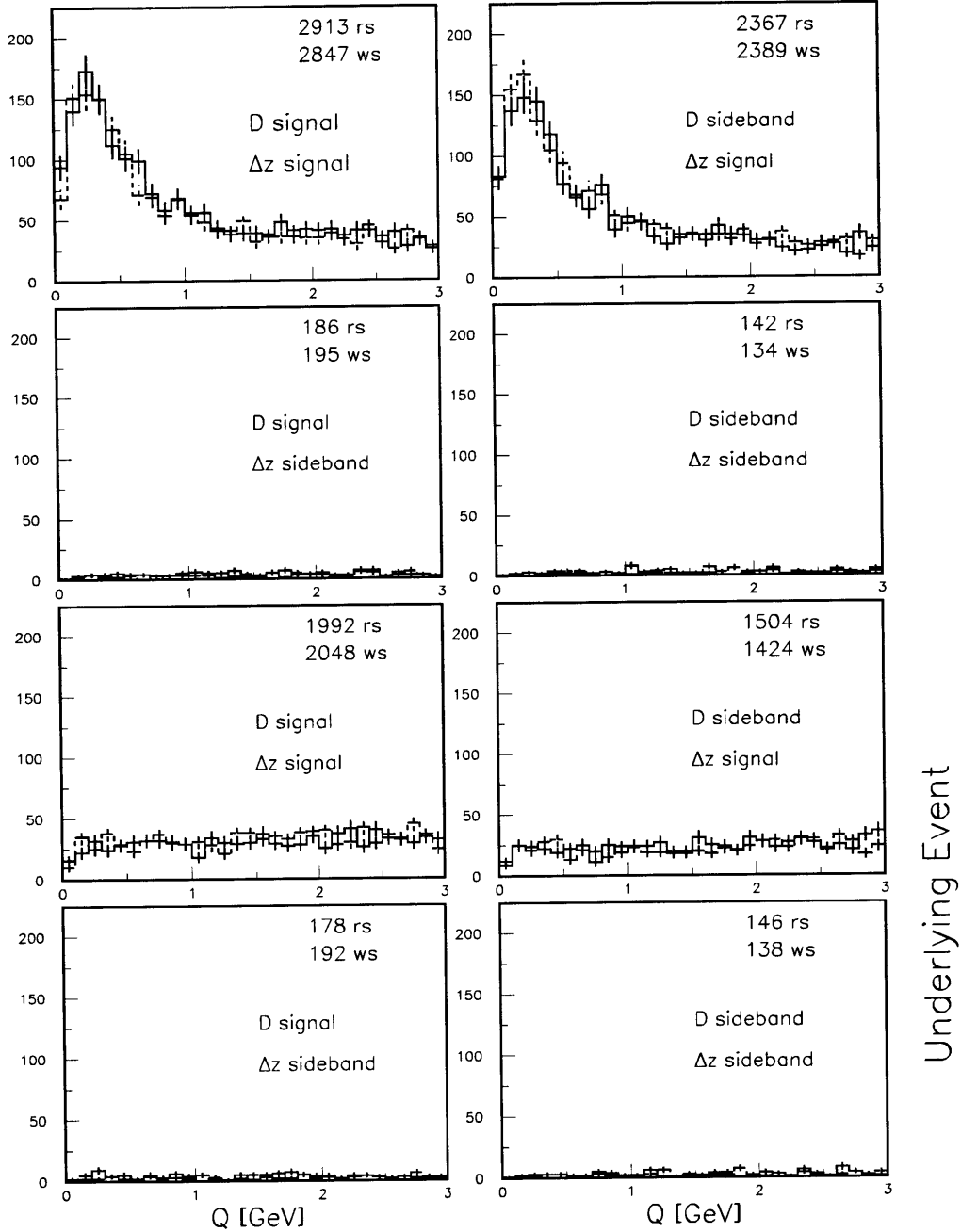
Figure 5-7: The Q spectrum of the B-*track* combinations seen in the $D^- \rightarrow K^+\pi^-\pi^-$ data. The solid (dashed) histograms are the right-sign (wrong-sign) combinations.

$K\pi\pi_s$ Data
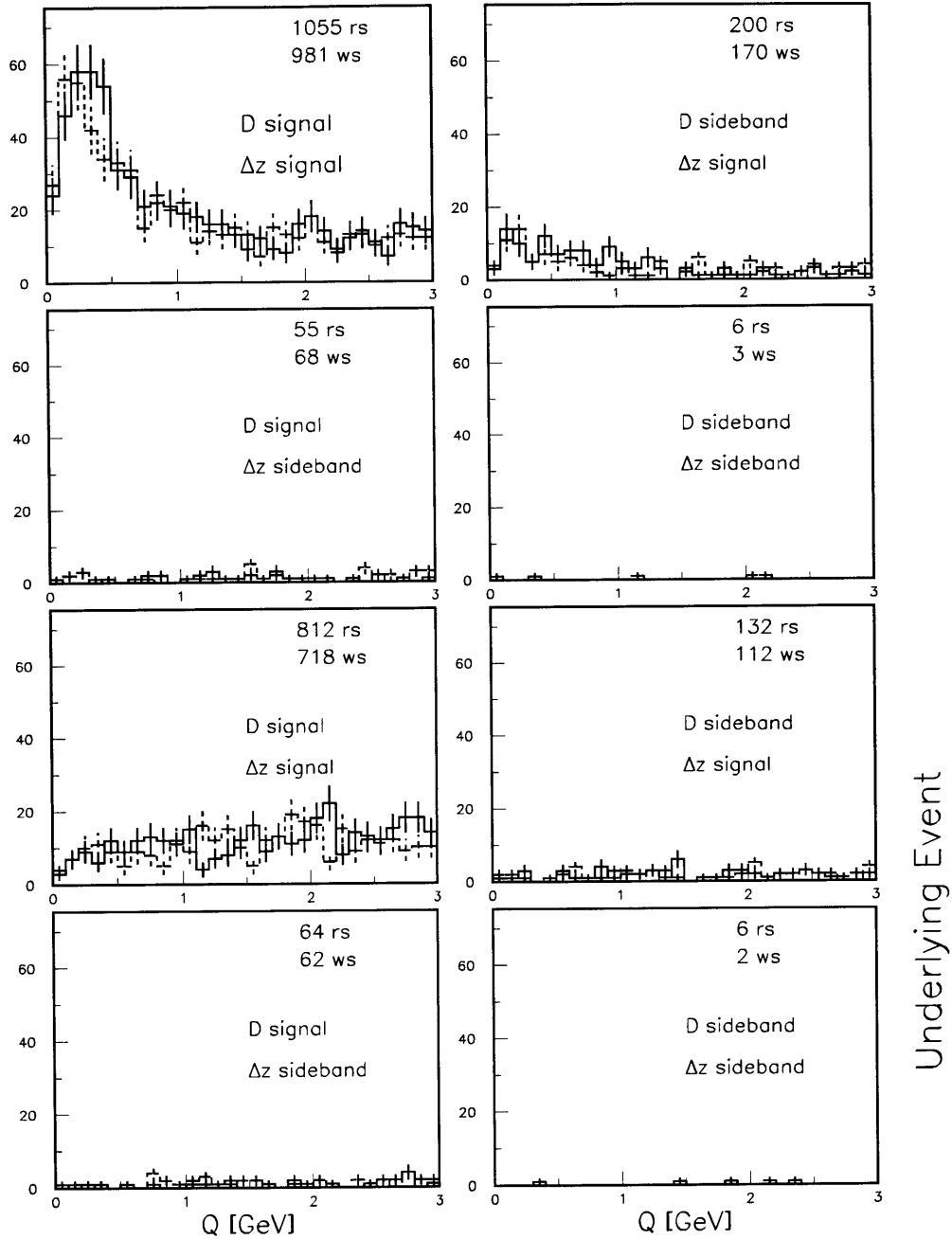
Figure 5-8: The Q spectrum of the *B-track* combinations seen in the $\bar{D}^0\pi_s^-$, $\bar{D}^0 \rightarrow K^+\pi^-$ data. The solid (dashed) histograms are the right-sign (wrong-sign) combinations.

K3ππ_s Data
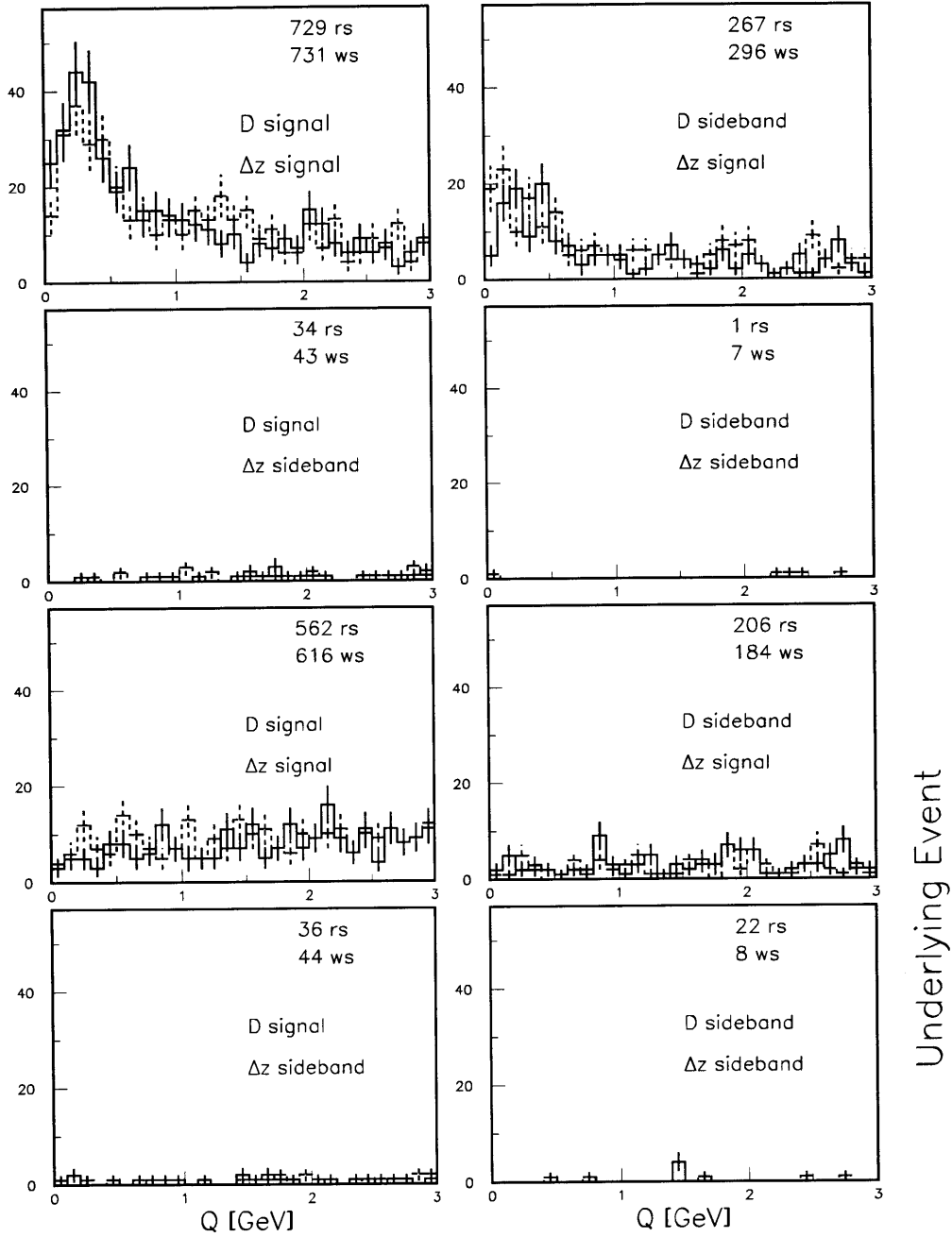
Figure 5-9: The Q spectrum of the *B-track* combinations seen in the $\bar{D}^0 \pi_s^-$, $\bar{D}^0 \rightarrow$ $K^+\pi^-\pi^+\pi^-$ data. The solid (dashed) histograms are the right-sign (wrong-sign) combinations.

$K\pi\pi^0\pi_s$ Data
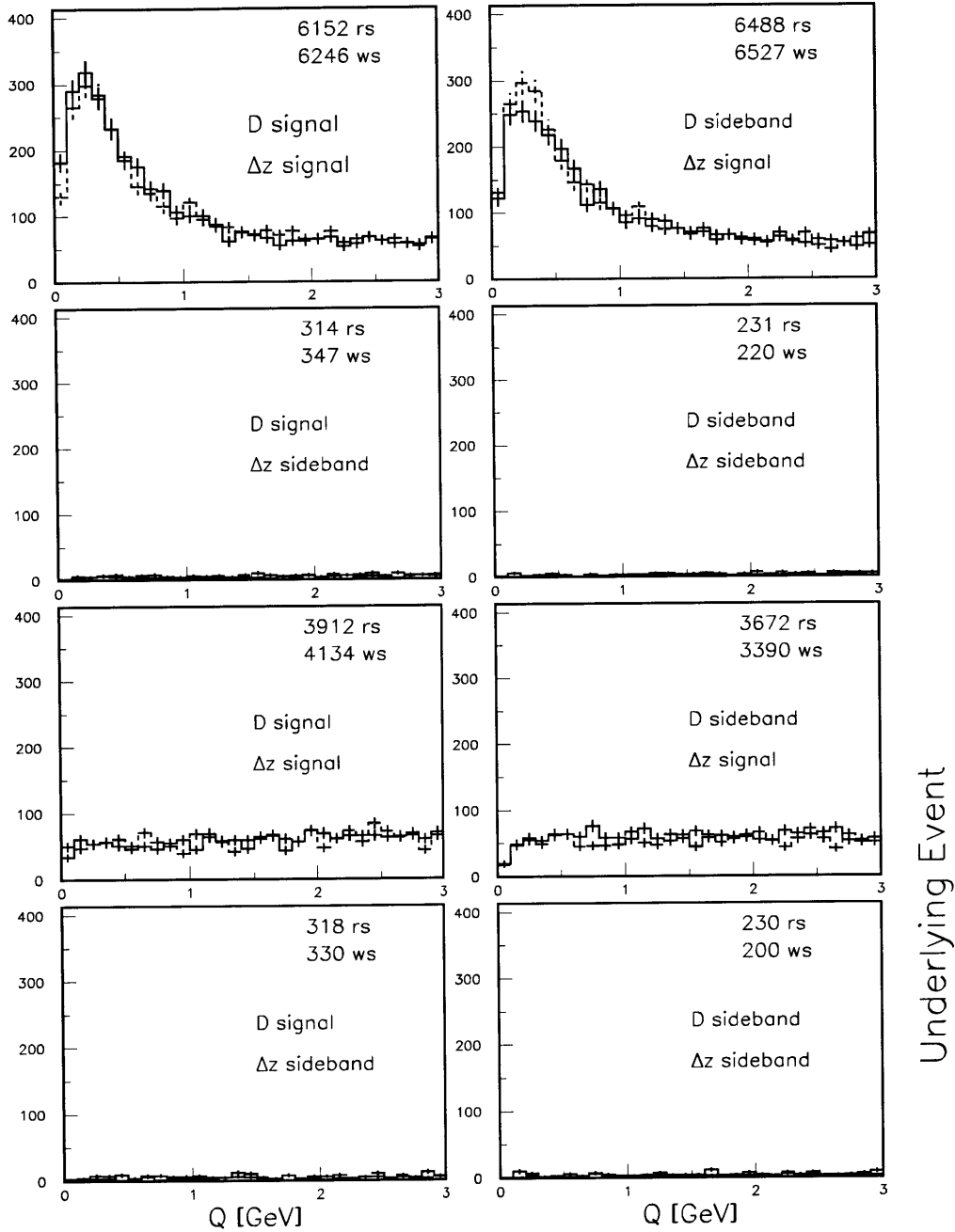
Figure 5-10: The Q spectrum of the B-track combinations seen in the $\bar{D}^0\pi_s^-$, $\bar{D}^0 \to K^+\pi^-\pi^0$ data. The solid (dashed) histograms are the right-sign (wrong-sign) combinations.
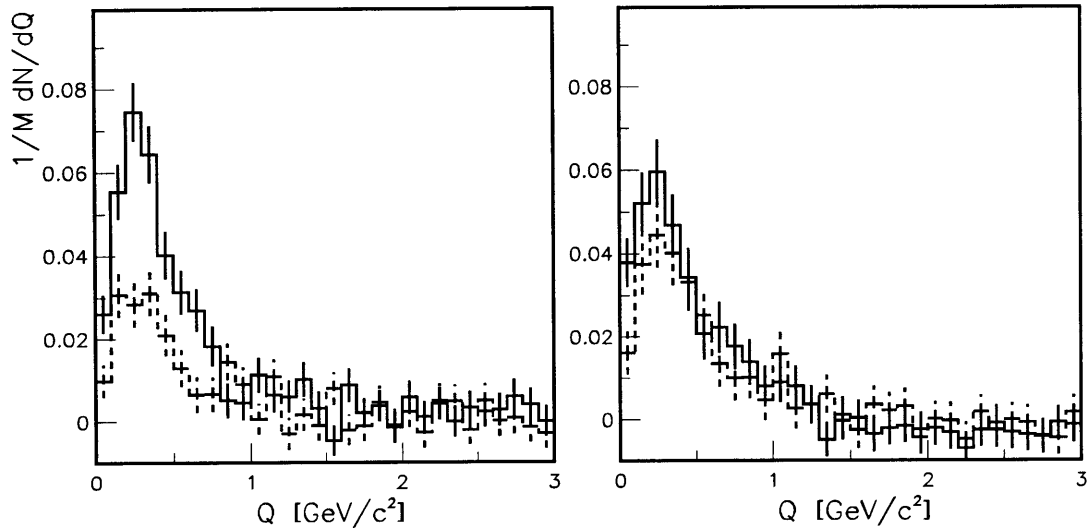
Figure 5-11: The Q spectrum of the *B-track* combinations seen in the two signatures with a large number of B candidates after all the "uncorrelated" backgrounds have been subtracted. The solid (dashed) histograms are the right-sign (wrong-sign) combinations.

5.8 Statistical Uncertainty

The treatment of statistical uncertainties is complicated by the fact that there may be more than one candidate track per event. From the statistical point of view, we can treat every B candidate as a separate experiment, and a presence of a track as a stochastic occurence. We then make the $n(Q)$ distribution as a profile histogram, and calculate the statistical uncertainties bin by bin as $\text{RMS}_i/\sqrt{M}$, where i is bin index, and M is the number of "experiments" (i.e., B candidates) that went into that bin. This procedure is applied separately to every histogram in figures 5-5 through 5-10, and in subsequent operations these uncertainties are added in quadrature.

Chapter 6

The Fit

This chapter describes the procedure for fitting the B^{**} signal together with the backgrounds described in the preceding chapter. First, the relevant variables are defined. Then, the equations for a general case of "flavor mixing" are derived. Finally, this result is applied to our case, which is illustrated in figure 6-1.
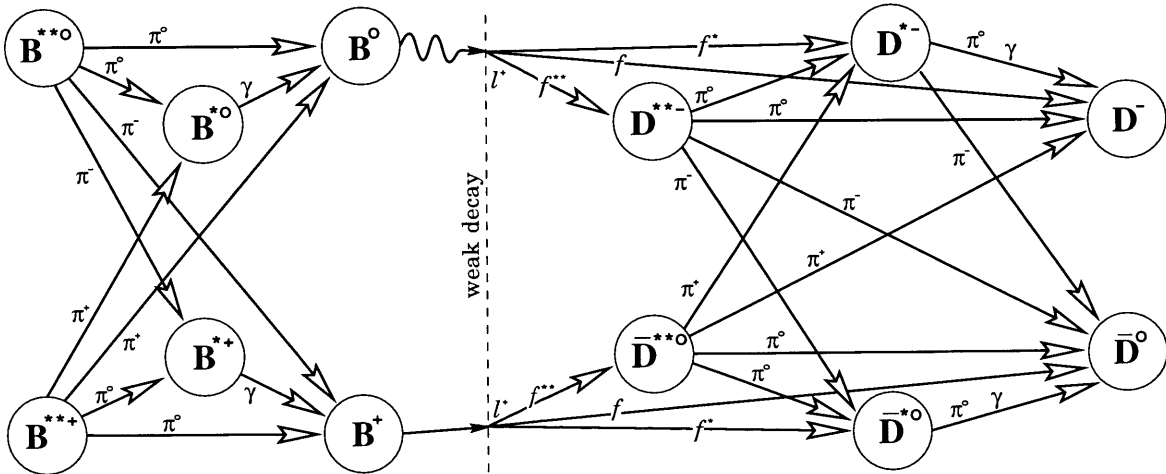
Figure 6-1: The B decay chains of most significance to this analysis.

6.1 Definitions

The central concept in this procedure is the distribution of the invariant mass (i.e., $Q = m(B\pi) - m(B) - m(\pi)$) of *B-track* combinations under the assumption that every track is a pion. We call this distribution the "count:"

$$n = n(Q) = \frac{dN}{dQ}.$$

It is important to note that we do not do "tagging," i.e. we do not choose one track for every B candidate. The integral of the count can therefore be greater than the number of B candidates—we consider all tracks that pass the cuts.

Tracks can be labelled as "right-sign" (RS) or "wrong-sign" (WS) by their charge relative to the flavor of the detected B meson. Right sign combinations are for instance $B^+\pi^-$ and $B^0\pi^+$, meaning that the two B flavors that contain a b antiquark have the opposite definition of right-sign correlation. (In particular, in semileptonic B decays the sign of the lepton is used as a direct indication of heavy quark flavor since it unambiguously determines whether it was a b or a $\bar{b}$ that decayed weakly.) Given this, we can label the counts of only right-sign (wrong-sign) tracks as n_{RS} (n_{WS}). Obviously, to completely describe the total count *and* charge correlation of tracks around B mesons we need to know both the n_{RS} and n_{WS} distributions.

In order to simplify the equations later in this derivation, we find it useful to define the "asymmetry" $\mathcal{A}$, which describes the excess of right-sign over wrong-sign combinations:

$$\mathcal{A} = \mathcal{A}(Q) = \frac{n_{\text{RS}}(Q) - n_{\text{WS}}(Q)}{n_{\text{RS}}(Q) + n_{\text{WS}}(Q)} \tag{6.1}$$

$$n_{\text{RS}} = n_{\text{RS}}(Q) = \frac{1 + \mathcal{A}(Q)}{2} \cdot n(Q) \tag{6.2}$$

$$n_{\text{WS}} = n_{\text{WS}}(Q) = \frac{1 - \mathcal{A}(Q)}{2} \cdot n(Q). \tag{6.3}$$

From the last two equations it follows that instead of using (n_{RS}, n_{WS}) to describe the

count and charge correlations, we can also use $(n,\ \mathcal{A})$. The two pairs of distributions contain the same information, so we will use whichever one makes the equations simpler to understand.

Since we have to deal with several backgrounds as well as the signal distribution, we label the counts of various components with the identifiers we defined in chapter 5. For example, the Q distribution of hadronization tracks is $(n^{\text{HA}},\ \mathcal{A}^{\text{HA}})$, and the signal is $(n^{**},\ \mathcal{A}^{**})$.

6.2   A General Case of Flavor Mixing
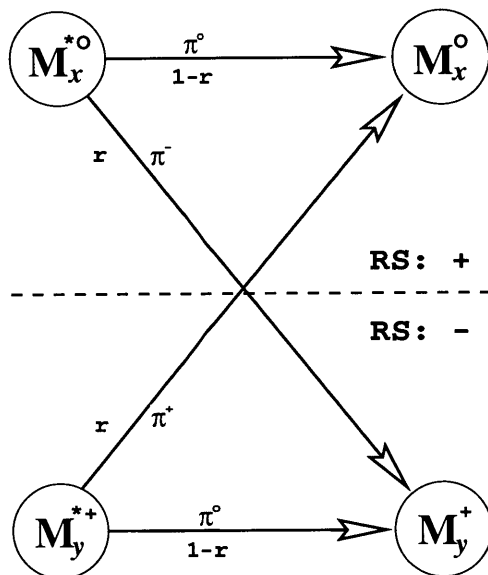
Figure 6-2: A general case of flavor mixing.

A generalized example of "flavor mixing" is illustrated in figure 6-2. The nodes in the graph depict different flavors and states of a fictional meson M. The subscripts x and y denote different light quark flavors $(u,\ d$ or $s)$. We can plot the count, $n(Q)$, of all tracks seen in the vicinity of detected mesons. If the tracks are seen around M_x^0 (M_y^+) we label the count n_x (n_y).

To clarify what we mean by "flavor mixing" we make the following observations:

- We detect only the ground states of meson M, i.e. we see only the states on the right side of the diagram.

- There is a "cross-talk" between the upper and lower half of the diagram from decays of M^* through a charged pion.

- Our definition of right-sign correlation is the opposite in the two halves of the diagram.

- If tracks are being produced in association with the meson M and in correlation with its flavor but not its state (ground or excited), then those tracks that are produced in association with an excited state of the meson that subsequently decays into a ground state of different flavor will appear to be of the opposite charge correlation with the detected meson from the one they had originaly with the produced meson.

- If a fraction R of all detected M mesons is produced in the excited state, and a fraction r of those decays through a charged pion (see figure 6-2), then the previous sentence can be expressed as:

$$n'_{x,\mathrm{RS}} = n_{x,\mathrm{RS}} \cdot \underbrace{((1-R)+(1-r)R)}_{\alpha^x_C} + n_{y,\mathrm{WS}} \cdot \underbrace{R \cdot r}_{\alpha^x_W} \qquad (6.4)$$

Here primes denote the distributions we see, and the distributions without primes are the ones we would see in the absence of flavor mixing. By exchanging RS with WS, and x with y, we get a set of four equations whose meaning is easier to grasp if we rewrite them as follows:

$$n'_x = n_x \cdot \alpha^x_C + n_y \cdot \alpha^x_W \qquad (6.5)$$

$$\mathcal{A}'_x = \frac{\mathcal{A}_x n_x \alpha^x_C - \mathcal{A}_y n_y \alpha^x_W}{n_y \alpha^x_C + n_y \alpha^x_W} \qquad (6.6)$$

In other words, if we are looking at particles produced in association with an uncertain state or flavor of the meson M, but can only detect the ground state with

106

a known flavor, then the contribution from particles produced in association with the other ("wrong") flavor is "leaking through" the excited state into our desired ("correct") flavor, hence the indices C and W. The quantity α_C^x (α_W^x) is therefore the fraction of detected M_x^0 mesons that were produced as any M_x^0 (M_y^+) state.

An important result is that the asymmetry of tracks from the cross-talk component enters in the weighted sum in equation 6.6 with a minus sign, meaning that the cross-talk *reduces* the observed asymmetry if asymmetries for both flavors were positive before the mix. This is a direct consequence of the fact that right-sign correlation for one meson flavor is wrong-sign for the other.

6.3   Excited B States

Going back to our case, we start from an imaginary perfect B sample, where "perfect" means an infinite number of events, each having a B meson that hadronized into a ground state with known momentum, flavor and decay length.

It is clear from equations 6.5 and 6.6 that if a background component is symmetric ($\mathcal{A} = 0$) and does not depend on the meson flavor ($n_x = n_y$), then it is not affected by flavor mixing. That is why we can eliminate PU and UE from this calculation by simply subtracting them, as described in chapter 5. The only distributions left are (n^{HA}, $\mathcal{A}^{\mathrm{HA}}$)—the ($n^{**}$, $\mathcal{A}^{**}$) and (n^{BD}, $\mathcal{A}^{\mathrm{BD}}$) are not defined yet: they arise as a consequence of "imperfections" of the sample we tackle later in the derivation.

The first instance of "flavor mixing" we encounter when going from the left side of figure 6-1 to the right are the B^{**} states. We introduce B^{**} into the picture under these assumptions:

- the hadronization process leaves the B^{**} with the momentum spectrum given by the Peterson fragmentation function with the same constant as the one for the ground state ($\epsilon_B = \epsilon_{B^{**}}$), and

- the hadronization process produces hadronization tracks with the same count and asymmetry with respect to the meson regardless of its spin or mass.

We can then write out equation 6.4 for the case in hand: n_{RS}^{HA} around observed B_d that originated in B_u^{**} decay will be equivalent[1] to n_{WS}^{HA} around observed B_u that were produced directly—RS becomes WS because its meaning is the opposite for B_d and B_u.

In order to get from here to equations 6.5 and 6.6 we also need the ratios R and r. Strong isospin sets the latter ratio to 2/3, but for the former one we need to know two more quantities:

$$h^{**} = \frac{\mathcal{B}(b \to B^{**})}{\mathcal{B}(b \to \text{any } B \text{ state})} \tag{6.7}$$

$$\epsilon_B^{**} = \frac{\epsilon(B \text{ from } B^{**} \text{ decay})}{\epsilon(\text{directly produced } B)} \tag{6.8}$$

$$\tag{6.9}$$

h^{**} is the probability that a b quark hadronizes into an orbitally excited state (this is the number we want to measure), and ϵ_B^{**} is the relative B reconstruction efficiency. Using these two, the coefficients in equation 6.4 can be expressed as:

$$\alpha_C = \frac{1 - h^{**}(1 - \frac{1}{3}\epsilon_B^{**})}{1 - h^{**}(1 - \epsilon_B^{**})} \tag{6.10}$$

$$\alpha_W = \frac{\frac{2}{3}h^{**}\epsilon_B^{**}}{1 - h^{**}(1 - \epsilon_B^{**})} \tag{6.11}$$

In other words, α_C is the fraction of observed B mesons accompanied by the "correct" hadronization tracks, and α_W is the fraction of observed B mesons accompanied by the "wrong" hadronization tracks. Note that, in this case, $\alpha_C^u = \alpha_C^d$ and $\alpha_W^u = \alpha_W^d$. The denominator in the equations for α_C and α_W is just the total number of detected B mesons—remember that the fraction of b quarks that *hadronize* into a B^{**} is not the same as the fraction of *detected* B mesons that were produced in B^{**} decay; the efficiency for detecting a B depends on how it was produced, hence the need for ϵ_B^{**}.

---

[1]This in not strictly correct, since the detected B meson has different kinematic properties from the one associated with the hadronization process. The effect of this difference on the shape of $n^{HA}(Q)$ is ignored in this analysis because the shape is not resonant and is further smeared by the B momentum resolution.

We now have all the elements needed for equations 6.5 and 6.6. By putting the real flavors in we get:

$$n_d^{\text{HA}\prime} = \alpha_C n_d^{\text{HA}} + \alpha_W n_u^{\text{HA}} \tag{6.12}$$

$$n_u^{\text{HA}\prime} = \alpha_C n_u^{\text{HA}} + \alpha_W n_d^{\text{HA}} \tag{6.13}$$

$$\mathcal{A}_d^{\text{HA}\prime} = \frac{\alpha_C n_d^{\text{HA}} \mathcal{A}_d^{\text{HA}} - \alpha_W n_u^{\text{HA}} \mathcal{A}_u^{\text{HA}}}{\alpha_C n_d^{\text{HA}} + \alpha_W n_u^{\text{HA}}} \tag{6.14}$$

$$\mathcal{A}_u^{\text{HA}\prime} = \frac{\alpha_C n_u^{\text{HA}} \mathcal{A}_u^{\text{HA}} - \alpha_W n_d^{\text{HA}} \mathcal{A}_d^{\text{HA}}}{\alpha_C n_u^{\text{HA}} + \alpha_W n_d^{\text{HA}}} \tag{6.15}$$

Of course, after this stage $(n^{**\prime}, \mathcal{A}^{**\prime})$ spring into existence—in a sense they are causing the flavor mixing. Charged pions from B^{**} decay will always appear as right sign, that is $n_{\text{WS}}^{**\prime} = 0$ and $\mathcal{A}_{u,d}^{**\prime} = 1$.

6.4 $B^0 - \bar{B}^0$ Mixing

Moving further to the right in figure 6-1, we encounter $B^0 - \bar{B}^0$ mixing. Some of the detected B^0 mesons in our sample began their brief careers as $\bar{B}^0$ mesons, and vice versa. The fraction of mixed mesons in the sample depends on the efficiency for detecting a B meson as a function of its proper time. We call this fraction χ_{eff}:

$$\chi_{\text{eff}} = \frac{\int N_{\text{MIXED}}(t) \cdot \epsilon_{\text{R}}(t) dt}{N_{\text{TOT}}} \tag{6.16}$$

Note that this is *not* the average mixing probability for a mixture of B flavors: it is simply χ_d corrected for our acceptance, i.e. the fraction of observed B_d^0 mesons that mixed. The difference between χ_d and χ_{eff} is a result of implicit $c\tau$ cuts we apply during event selection.

Mixing flips the sign correlation of all particles that originate before the decay of a neutral B, but it does not affect the total count. Therefore, the equations will look simpler than in the general case—the counts and asymmetries are the same in both

the upper and lower half of figure 6-2. The following relations hold:

$$n''_{\text{RS}} = (1 - \chi_{e\!f\!f})n'_{\text{RS}} + \chi_{e\!f\!f}n'_{\text{WS}} \tag{6.17}$$

$$n''_{\text{WS}} = (1 - \chi_{e\!f\!f})n'_{\text{WS}} + \chi_{e\!f\!f}n'_{\text{RS}} \tag{6.18}$$

therefore $\mathcal{A}'' = (1 - 2\chi_{e\!f\!f})\mathcal{A}'$. Since the total count is not affected, mixing only affects those components of the background that have asymmetry different from zero (i.e., the hadronization tracks), but it also affects a portion of the signal—the pions from the decay of a charged B^{**}. We can thus write:

$$\mathcal{A}_d^{\text{HA}''} = (1 - 2\chi_{e\!f\!f})\mathcal{A}_d^{\text{HA}'} \tag{6.19}$$

$$\mathcal{A}_u^{\text{HA}''} = \mathcal{A}_u^{\text{HA}'} \tag{6.20}$$

$$\mathcal{A}_d^{**''} = (1 - 2\chi_{e\!f\!f})\mathcal{A}_d^{**'} = (1 - 2\chi_{e\!f\!f}) \tag{6.21}$$

$$\mathcal{A}_u^{**''} = \mathcal{A}_u^{**'} = 1 \tag{6.22}$$

6.5 Unknown B Flavor

At this point we can drop the assumption that we know the flavor of the detected B meson with certainty. In other words, we are moving to the right edge of figure 6-1.[2]

If a B meson decays into an excited D state instead of the ground state, say a D^{+*}, and we fail to detect the charged pion from the strong decay of the excited D state, it will appear to us that the B candidate was a B_u^- when in fact it was a $\bar{B}_d^0$. Therefore, in every sample of B_u^- candidates reconstructed as an $\ell^- \nu D^0$ we expect a certain fraction of $\bar{B}_d^0$ events.

We call a particular set of detected particles a "decay signature," and there can be multiple "decay chains" that feed into a signature. Every decay signature has one

---

[2]The equations shown are a bit more general: we can use them in any B sample where we can tell at least the flavor of the b quark at decay. For samples in which the flavor of the heavy quark is not known, the right-hand sides of equations (6.23), (6.24) and (6.25) must be modified to include contribution from the other two meson flavors (i.e., $n_{\bar{d}}^{\text{HA},**''}$, $n_{\bar{u}}^{\text{HA},**''}$, $\mathcal{A}_{\bar{d}}^{\text{HA},**''}$ and $\mathcal{A}_{\bar{u}}^{\text{HA},**''}$).

dominant or "direct" decay chain, the one used in the definition of "right-sign" and "wrong-sign" correlation.

In general, we can make a flavor matrix α_k^x, where α is the fraction of B_x mesons in a sample consisting of events with a decay signature k. For instance, the above mentioned $\ell^- \nu D^0$ sample contains $\alpha_{k=\ell D^0}^u$ B_u^+ mesons and $\alpha_{k=\ell D^0}^d$ B_d^0 mesons. For every k the sum of α_k^u and α_k^d is one.

The procedure for calculating the α_k^u and α_k^d for our decay signatures is described fully in chapter 4. Recall that the input parameters needed for their calculation are:

- f^{**}—the fraction of semileptonic B decays that proceed through a D^{**} or a non-resonant $D^{(*)}\pi$ combination (the four-body decay):

$$f^{**} \equiv \frac{\mathcal{B}(B \to \nu\ell D^{**})}{\mathcal{B}(B \to \nu\ell X)}$$

- P_V—the fraction of D^{**} states that decay into a vector state:

$$P_V \equiv \frac{\mathcal{B}(D^{**} \to D^*\pi)}{\mathcal{B}(D^{**} \to D^*\pi) + \mathcal{B}(D^{**} \to D\pi)}$$

- f^* and f—the numbers analogous to f^{**} for the D^* and D states; since we ignore B decays into higher D states the three fractions add to one: $f^{**} + f^* + f = 1$; this means there are only two independent numbers, so we use f^{**} and

$$R_f = \frac{f^*}{f}$$

- $\epsilon(\pi_s)$—the efficiency for detection of pions from D^* decay; the Monte Carlo doesn't model well the tracking efficiencies in the kinematic range these pions populate, so we calculate $\epsilon(\pi_s)$ from the already mentioned parameters and the R^*, the fraction of detected $\bar{D}^0$ mesons that come from a D^{*-} decay, which is partly measured from the data as explained earlier;

- τ_{B^+}/τ_{B^0}—the ratio of B^+ and B^0 lifetimes; gives us the ratio of their semilep-

111

tonic branching fractions.

Keeping in mind the results from the generic case, we can write:

$$n_k^{\mathrm{HA},**} = \alpha_k^d n_d^{\mathrm{HA},**\prime\prime} + \alpha_k^u n_u^{\mathrm{HA},**\prime\prime} \tag{6.23}$$

$$\mathcal{A}_k^{\mathrm{HA},**} = \frac{\alpha_k^d n_d^{\mathrm{HA},**\prime\prime} \mathcal{A}_d^{\mathrm{HA},**\prime\prime} - \alpha_k^u n_u^{\mathrm{HA},**\prime\prime} \mathcal{A}_u^{\mathrm{HA},**\prime\prime}}{\alpha_k^d n_d^{\mathrm{HA},**\prime\prime} + \alpha_k^u n_u^{\mathrm{HA},**\prime\prime}} \quad \text{or} \tag{6.24}$$

$$\mathcal{A}_k^{\mathrm{HA},**} = \frac{\alpha_k^u n_u^{\mathrm{HA},**\prime\prime} \mathcal{A}_u^{\mathrm{HA},**\prime\prime} - \alpha_k^d n_d^{\mathrm{HA},**\prime\prime} \mathcal{A}_d^{\mathrm{HA},**\prime\prime}}{\alpha_k^u n_u^{\mathrm{HA},**\prime\prime} + \alpha_k^d n_d^{\mathrm{HA},**\prime\prime}} \tag{6.25}$$

where equation 6.24 (6.25) holds if the direct chain for the decay signature leads from a B_d (B_u).

These are our final formulas for the counts and asymmetries of the B^{**} signal and background. Before we fit these to the data, we have to add the (n^{BD}, $\mathcal{A}^{\mathrm{BD}}$) which comes into being at (or "is causing") this last step. We get this last contribution from a Monte Carlo calculation, and normalize it according to the parameters that go into the calculation of α_k^d and α_k^u.

6.6 Backgrounds Revisited

Armed with the nomenclature developed in this chapter, we can now return to the backgrounds not accounted for in chapter 5.

6.6.1 The b Hadronization Products

As mentioned earlier, the "b hadronization products" are everything that remains of the b jet after removing the B meson (i.e., its decay products). In a sense, these particles are the strong radiation the b quark has to shed in order to become color-neutral. But the B^{**} also decays strongly, so the only quality that distinguishes its decay products from hadronization tracks is the fact that they form resonances with the B meson. Considering that our capability for seeing resonances in this data sample is limited by resolution and statistics to the order of 0.1 GeV, it is clear that

we can't hope to see a narrow peak on top of a smooth background. What we have to do instead is use theoretical models to predict the properties of hadronization tracks, and assume that everything else are B^{**} decay products. This method has one obvious disadvantage: we have to trust the hadronization model.
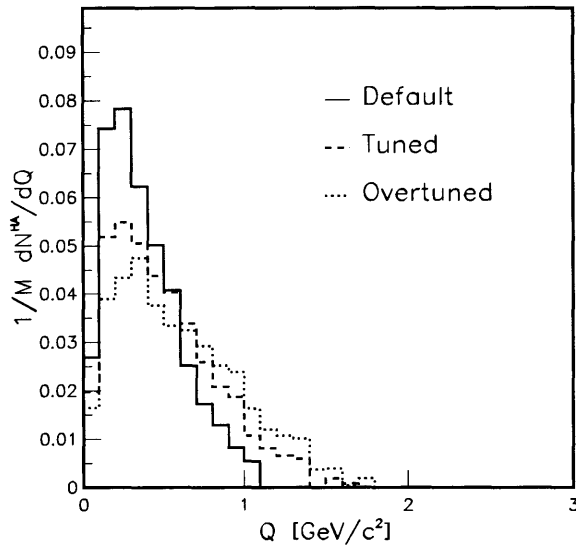
Figure 6-3: The change of the count of hadronization tracks, $n^{\text{HA}}(Q)$, generated by the Monte Carlo resulting from changing the parameters of the fragmentation model.

This innocent-sounding flaw turns into a near-disaster when we consider the results presented in reference [44]: the latest technology in Monte Carlo generation doesn't do a very good job at describing the particles coming out of the primary vertex. In the same note we have found a set of parameters that removes the symptoms (by increasing $\sigma_{\text{p}_\text{T}}^{frag}$, the "thickness" of the color strings), but the disease remains: can we trust the model if we had to stretch its fundamental parameters so far from the ones measured at colliders with a different physics setting?

The magnitude of the problem is illustrated in figure 6-3. The three histograms show the count, $n(Q)$, of the hadronization component only, as seen in the Monte Carlo with three different sets of parameters. The underlying event has been subtracted as described in chapter 5. The "tuned" parameters are the ones listed in

113
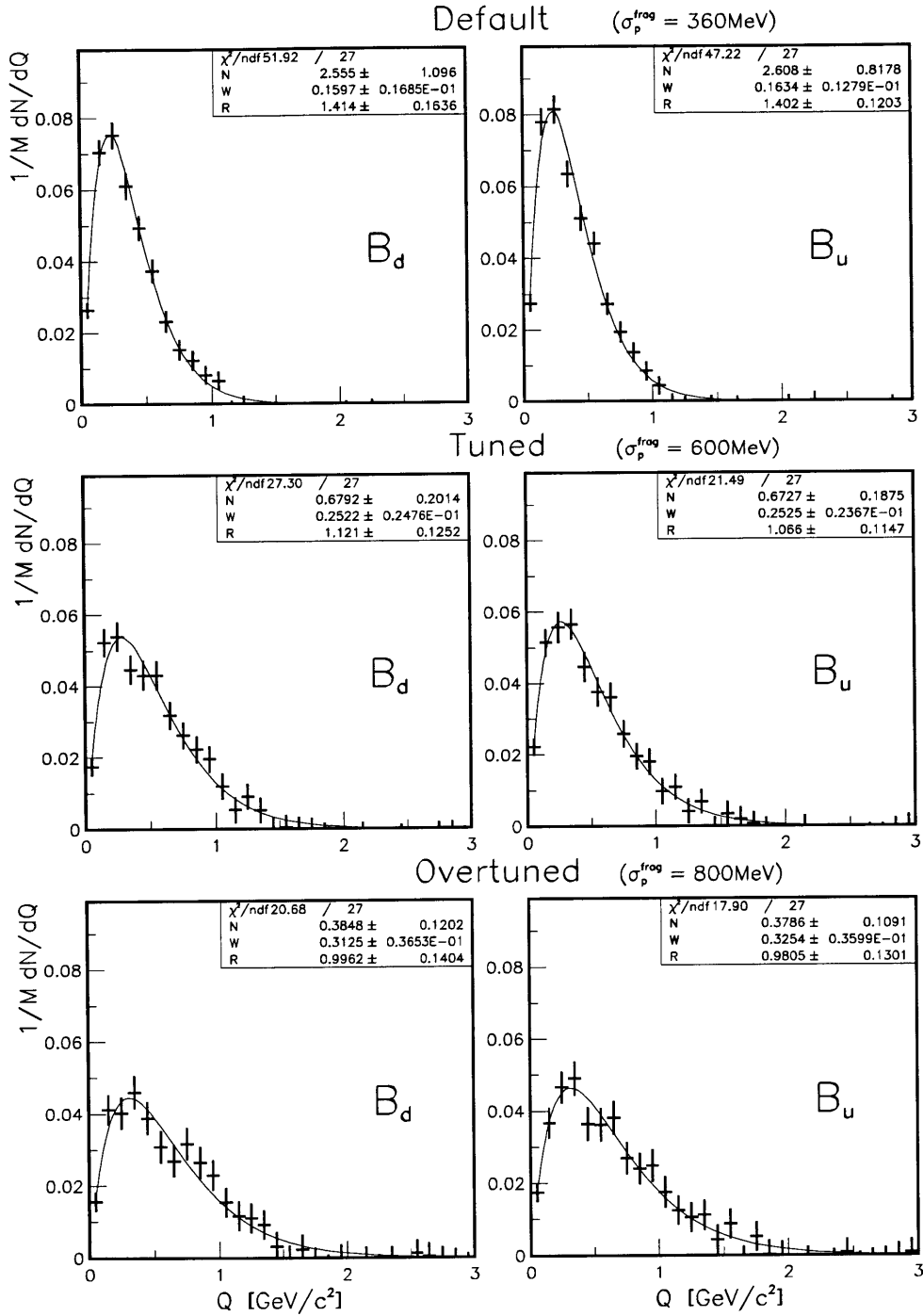
Figure 6-4: The counts of hadronization tracks, $n_{RS,WS}^{HA}(Q)$, in the Monte Carlo with different sets of parameters.

appendix A; the "overtuned" ones are another set of parameters that gives us a good description of the underlying event, but with a different setup of multiple interactions (the default one), so the $\sigma_{p_T}^{frag}$ is set to an even higher value of 800 MeV; the "default" parameters are the common ones for the CDF installation of PYTHIA. The change in the Monte Carlo prediction between these three (not unreasonable) sets of parameters reaches 50% in the region below 500 MeV, where we expect the signal to be. This is clearly not acceptable.

The ideal solution would certainly be to measure the properties of the hadronization component in a sample with no B^{**} events. Since we don't know yet how to make such a sample, the second best solution is to simulatneously fit the properties of the hadronization component and the B^{**} excess. The most important question we can ask here is: can our data constrain well enough all the parameters? The answer turns out to be yes, but only if we make further assumptions.

The Shape

The three rows of plots in figure 6-4 are the shapes of the hadronization component for the same three sets of parameters shown in figure 6-3, but this time separated by the meson flavor and fitted with a function[3] $n(Q) = \mathrm{N} \cdot \exp(-Q/\mathrm{W}) \cdot Q^{\mathrm{R}}$. Here N, W and R are the parameters for normalization, width and rise of the distribution.

As we expect, the width of the distribution on the Q axis (parameter P2) increases as we increase $\sigma_{p_T}^{frag}$—particles are being produced with higher transverse momenta relative to the b direction, so they form higher masses with the B meson. We also see that the track multiplicity is slightly higher around charged mesons than around neutral ones, which is also expected. Another valuable piece of information can be extracted from the figures: the widths of the hadronization distributions are essentially the same around the charged and neutral mesons, and this holds even as we

---

[3]The choice of function was motivated by two observations: the rise is predominantly phase space (i.e., the count must be zero at $Q = 0$), and the falloff is physics and appears to be exponential to first order.

change the parameters. This means that we can eliminate one degree of freedom by using a common width for both flavors.

The Asymmetry

Next we check the charge correlation. Figure 6-5 shows the fitted asymmetries of the hadronization component shown in the previous figures. The fact that the fits diverge at high Q values is of little consequence—there are hardly any hadronization particles produced there. In the low-Q region, where the signal is expected to lie, the difference is very small. In other words, the asymmetry of the hadronization component is much less parameter-dependent than its shape. This is a very important result. It supports our conjecture that we can constrain the shape of the hadronization background under the signal by fitting it simultaneously in the distributions and regions where we expect little or no B^{**} contribution. We can treat the different asymmetries as a systematic uncertainty, and a relatively small one at that, as will be shown in the next section.
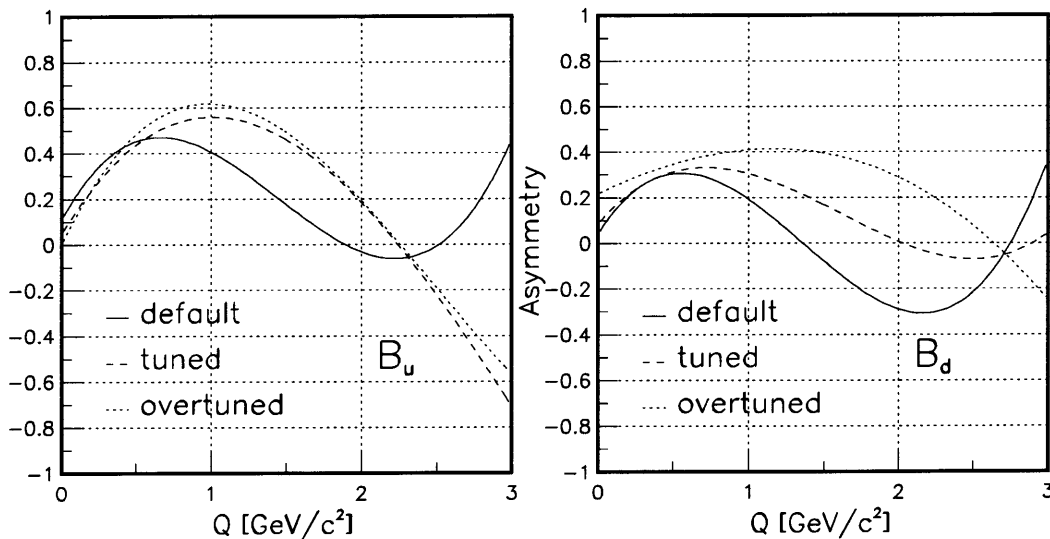
Figure 6-5: The asymmetry of hadronization tracks ($\mathcal{A}^{\text{HA}}$) in the Monte Carlo with different sets of parameters.

6.6.2 Gluon Splitting
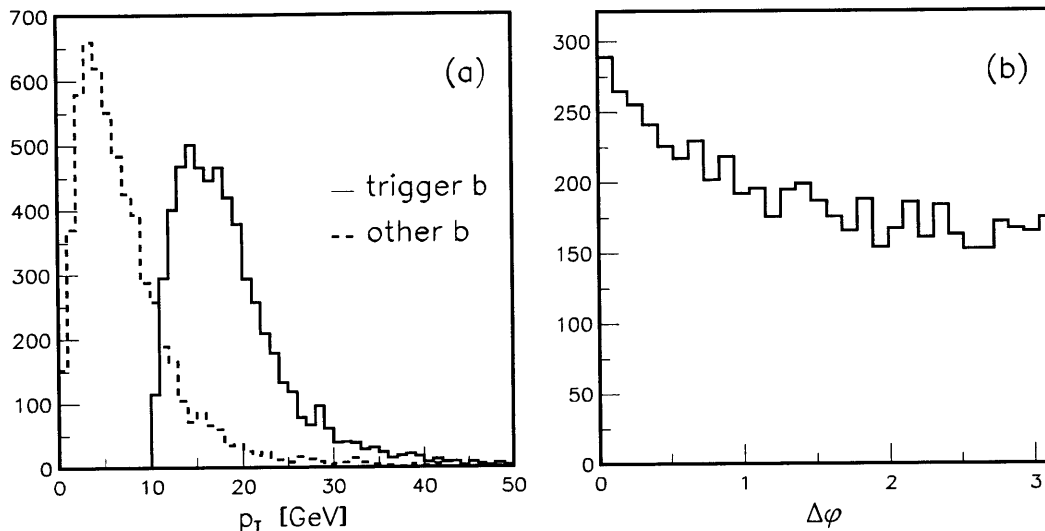
Figure 6-6: (a) The transverse momenta and (b) the angle in the transverse plane between the two b hadrons in "gluon splitting" NLO b production.

The treatment of backgrounds described so far breaks down if our sample contains a large background component with the shape significantly different from both the underlying event and the hadronization products. The most likely candidate for such a background is NLO $b\bar{b}$ production, in which the other b quark in the event is often near the reconstructed one in azimuth. To test the effect of such a background on our result, we have analyzed the events with heavy flavor produced by "gluon splitting." We used the Monte Carlo to generate the processes $gg \rightarrow gg$, $q\bar{q} \rightarrow gg$, and $qg \rightarrow qg$, and extracted the events where a gluon "splits" into a $b\bar{b}$ pair and one B passes our triggers. These events were then reweighted so that the angular distribution of the second b quark agrees with the theoretical prediction from reference [29].

The transverse momenta and the angle between the two b hadrons in such events are shown in figure 6-6. The second b is correlated in flavor with the reconstructed one, so their proximity is a reason for concern.

Figure 6-7 shows the Q distributions of the hadronization and the underlying event around the reconstructed B, as well as those of the decay products of the other

117
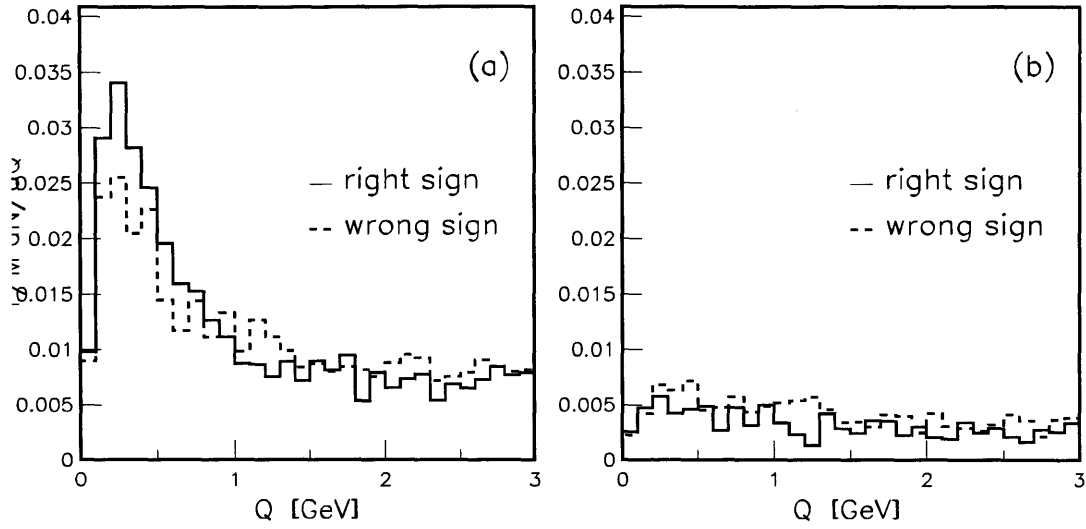
Figure 6-7: The dN/dQ distributions of (a) the hadronization and the underlying event, and (b) the decay products of the other b hadron in "gluon splitting" NLO b production.
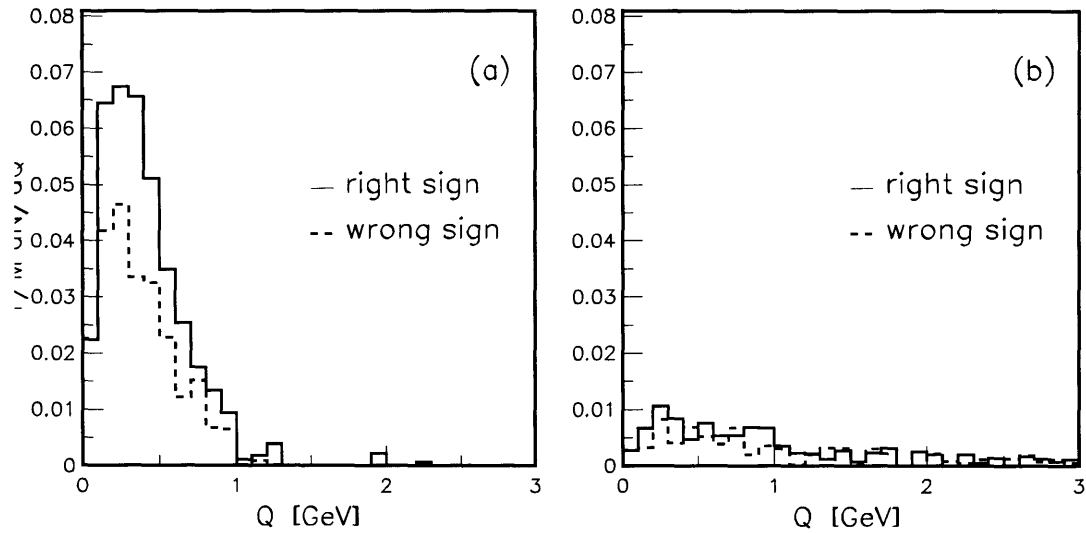
Figure 6-8: The underlying event-subtracted dN/dQ distributions of (a) the hadronization component, and (b) the decay products of the other b hadron in "gluon splitting" NLO b production.

b hadron. The particles from the other b hadron are, apparently, a significant portion of prompt tracks in such events. This is not a surprising result, given the low average transverse momentum of the other b quark. Our result is not, however, affected much by the absolute abundance of these tracks; since we are subtracting the distributions in the far $(1 < |\Delta\phi| < 2)$ region from the ones in the near $(|\Delta\phi| < 1)$ region, the quantity of greater significance is the *excess* of tracks in the near region over the far region, as shown in figure 6-8.

To quantify the effect of gluon splitting, we add the distributions from figure 6-8b (separated by charge correlation and flavor of the reconstructed B meson) to the predicted hadronization excess, and use the combined distributions in the flavor mixing calculations described earlier. The gluon-splitting portion is, of course, scaled by the expected fraction of events in our sample produced in this way. For a conservative error estimate, we set this fraction to $30 \pm 30\%$.

6.6.3 $B_s^{**} \to BK$ Background

The charged K from the decay $B_s^{**} \to B_u^+ K^-$ topologically looks just like the π from the $B_d^{**} \to B_u^+ \pi^-$ decay, so we expect to see a reflection of the B_s^{**} mass peak. Moreover, the decay $B_s^{**} \to B_d^0 K^0$ dilutes our B_d^0 signatures since we are not reconstructing neutral kaons. This situation is illustrated in figure 6-9.

B_s^{**}, unlike B_d^{**}, is strong isospin-neutral so it decays into charged and neutral products with equal probability. This simplifies the calculation—we need only one number, r_s, to describe the fraction of B mesons in our sample that originated in B_s^{**} decay:

$$r_s = \left(\frac{f_s}{f_d}\right)_{corr} \cdot h^{**} \cdot \frac{1}{2} \cdot \epsilon_s^{**} \tag{6.26}$$

The terms on the right-hand side of this equation have the following meanings:

- $(f_s/f_d)_{corr}$ is the relative B_s production rate, corrected for the fact that the value quoted in the literature [32] is measured from the relative abundance of
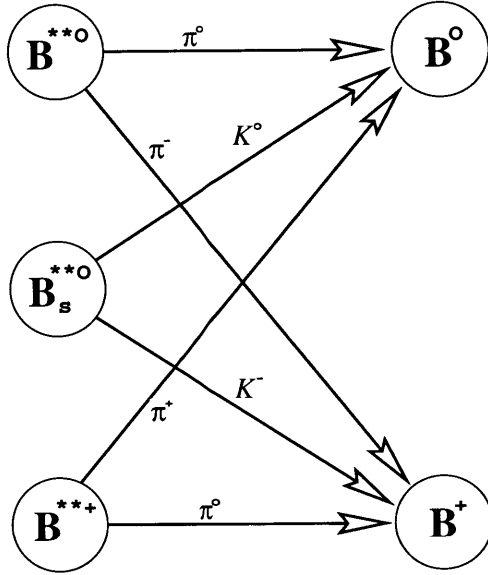
Figure 6-9: B_s^{**} contribution to our data sample.

observed exclusive B decay signatures, *i.e.* it doesn't take into account the $B_s^{**} \to BK$ "leak;" the required correction is

$$\left(\frac{f_s}{f_d}\right)_{corr} = \frac{2\frac{f_s}{f_d}}{2(1 - h^{**}) - h^{**}\frac{f_s}{f_d}}$$

- h^{**} is the fraction of B_s produced in a 2P state,

- 1/2 of which decay into a B_d, the other half into a B_u;

- ϵ_s^{**} is the relative efficiency for detecting a B produced in a B_s^{**} decay.

The fraction of charged B mesons accompanied by a kaon from B_s^{**} decay will then be $r_s \cdot \epsilon_K^{**}$, where ϵ_K^{**} is the acceptance-efficiency for detecting the charged K. The shape of this contribution, as well as ϵ_s^{**} and ϵ_K^{**}, are determined from the Monte Carlo calculation (see chapter 7).

6.6.4 B_s^{**} Hadronization

One additional complication arises from the presence of $B_s^{**} \to BK$ decays in our data sample: the hadronization tracks produced in association with the B_s^{**} are expected to have different properties from the ones seen around the B_u and B_d. This is illustrated in figure 6-10.

The left plot in the figure shows that the expected asymmetry of the B_s hadronization component is similar to the one seen around B_d in the region of greatest interest. The count, on the other hand, is expected to be significantly higher: the plot on the right shows the ratio of counts of tracks seen around B_s and B_d. Since we can't let this shape float like the B_d and B_u shapes (this is a relatively small background and we have no data to constrain its shape), we fix it to the shape of the hadronization around B_d by fitting a straight line to the ratio in figure 6-10b and using that as a correction.
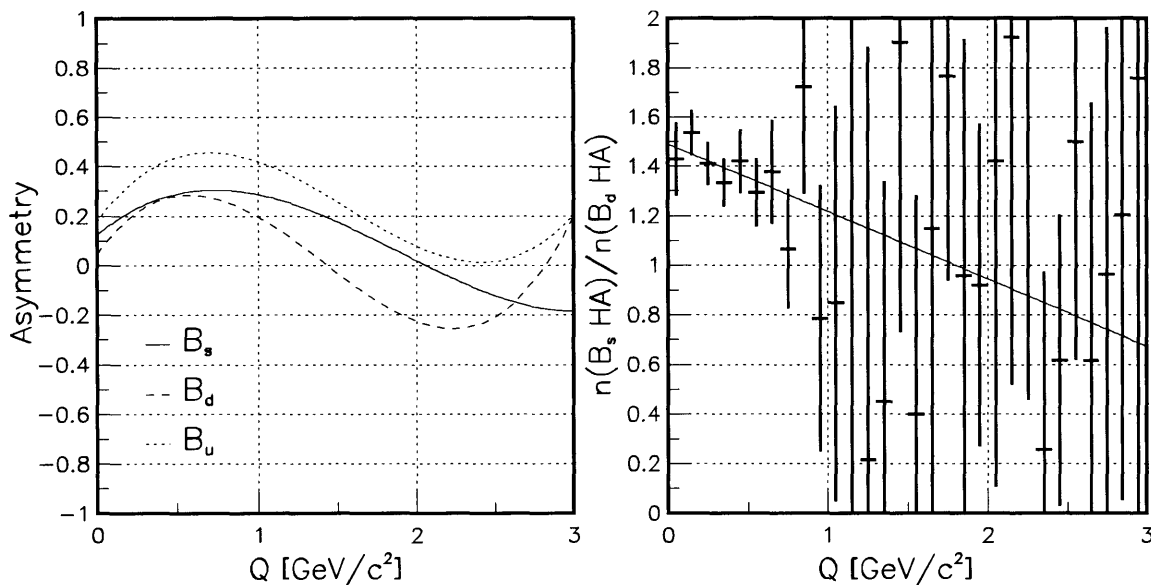
Figure 6-10: Expected distributions of B_s^{**} hadronization tracks. The left plot compares the expected asymmetries of hadronization tracks around different meson flavors. The right plot shows the expected ratio of counts of the hadronization tracks observed around B_s and B_d.

121

The required corrections to the quantites from equations 6.12 through 6.15 are as follows:

$$n_d^{\mathrm{HA}\prime} \rightarrow n_d^{\mathrm{HA}\prime}(1 - r_s) + n_d^{\mathrm{HA}} r_s \mathrm{corr}(Q) \tag{6.27}$$

$$n_u^{\mathrm{HA}\prime} \rightarrow n_u^{\mathrm{HA}\prime}(1 - r_s) + n_d^{\mathrm{HA}} r_s \mathrm{corr}(Q) \tag{6.28}$$

$$\mathcal{A}_d^{\mathrm{HA}\prime} \rightarrow \frac{\mathcal{A}_d^{\mathrm{HA}\prime} n_d^{\mathrm{HA}\prime}(1 - r_s) + \mathcal{A}_s^{\mathrm{HA}} n_d^{\mathrm{HA}} r_s \mathrm{corr}(Q)}{n_d^{\mathrm{HA}\prime}(1 - r_s) + n_d^{\mathrm{HA}} r_s \mathrm{corr}(Q)} \tag{6.29}$$

$$\mathcal{A}_u^{\mathrm{HA}\prime} \rightarrow \frac{\mathcal{A}_u^{\mathrm{HA}\prime} n_u^{\mathrm{HA}\prime}(1 - r_s) - \mathcal{A}_d^{\mathrm{HA}} n_d^{\mathrm{HA}} r_s \mathrm{corr}(Q)}{n_u^{\mathrm{HA}\prime}(1 - r_s) + n_d^{\mathrm{HA}} r_s \mathrm{corr}(Q)} \tag{6.30}$$

$$n^{**\prime} \rightarrow n^{**\prime}(1 - r_s) \tag{6.31}$$

where $\mathrm{corr}(Q)$ is the mentioned correction function.

6.7 The χ^2 Function

Using the formulas derived in this section, we perform a binned χ^2 fit to the data of the expected (n_{RS}, n_{WS}) distributions for the signal plus all backgrounds.

In several steps in the above derivation we have introduced parameters that are not known from first principles and are not measured very well, namely χ_{eff}, f^{**}, P_V, R_f, R^*, τ_{B+}/τ_{B^0}, f_s/f_d, and the efficiencies: ϵ_B^{**}, ϵ_π^{**}, ϵ_D^{**}, ϵ_s^{**} and ϵ_K^{**}. These parameters determine our final sample composition, and some of them are highly correlated. It would therefore be incorrect to treat their uncertainties as uncorrelated systematic errors; to account for the correlations we have to leave these parameters floating in the fit, with the appropriate χ^2 terms added to the function. The complete χ^2 function is then:

$$\chi^2 = \sum_{k,Q} \left(\frac{n_{k,\mathrm{RS}}^{calc}(Q) - n_{k,\mathrm{RS}}^{meas}(Q)}{\sigma_{k,\mathrm{RS}}^n(Q)} \right)^2 + \sum_{k,Q} \left(\frac{n_{k,\mathrm{WS}}^{calc}(Q) - n_{k,\mathrm{WS}}^{meas}(Q)}{\sigma_{k,\mathrm{WS}}^n(Q)} \right)^2$$
$$+ \sum_{P} \left(\frac{P^{meas} - P}{\sigma(P)} \right)^2$$

where the last term sums up the relative deviations of all the floating parameters

mentioned above from their measured values.

6.8 The Difference Between B_u and B_d

We now have all the elements in place to make an important observation. A big puzzle during the study of this data sample was why is there such a large excess of right-sign tracks in the B_u^+ signatures and hardly any excess in the B_d^0 signatures (see figure 5-11). Here is the complete answer:

- Since the hadronization undergoes flavor mixing through a B^{**} decay, the higher HA asymmetry around B_u^+ will not get reduced much by the lower HA asymmetry around B_d^{**0}, but the lower HA asymmetry around B_d^0 will practically get wiped out by the higher HA asymmetry around B_u^{**+}. The $\mathcal{A}^{**}$ is still equal to one around both flavors at this stage, but

- B_d^0 mixes, so about a fifth of its own B^{**+} excess ends up in the wrong sign (which reduces the asymmetry by two fifths), and B_u^+ doesn't mix, so all of its B^{**0} excess is seen as right-sign.

- In the B_d^0 signatures the cross-talk comes from the B_u^+ which doesn't mix and is accompanied by hadronization of larger asymmetry, so all of the cross-talk excess goes into the wrong sign for B_d^0. In the B_u^+ signatures, on the other hand, the cross-talk comes from the B_d^0 which mixes and so contributed two fifths of its own B^{**} excess and asymmetry (which was lower to begin with) to the right sign for B_u^+.

- The $B_s^{**} \rightarrow BK$ background further increases the asymmetry around the charged B mesons but not around the neutral ones.

The combined effect is difficult to quantify because we are measuring some of the quantities that determine the magnitude of various components from the same data sample. The sum of these effects, however, is able to explain the counts and asymmetries we observe in the data very well, as shown in the next chapter.

Chapter 7

Results

7.1 Efficiencies

Figure 7-1 depicts the sources of all the efficiencies mentioned earlier in the text. (For brevity, "efficiency" in this text means the product of kinematic and detector acceptance and efficiency for finding a particle.)

Since we normalize all our findings to the number of observed B mesons, the efficiency for finding a "directly" produced B meson (*i.e.* the one that originated in the hadronization process, not in the decay of an excited state) is set to unity. ϵ_B^{**} (ϵ_s^{**}) is then the efficiency for finding a B meson produced in decay of B^{**} (B_s^{**}) *relative* to the one for the directly produced mesons. ϵ_π^{**} (ϵ_K^{**}) is, similarly, the efficiency for finding a pion (kaon) from B^{**} decay given that the B has been observed. ϵ_D^{**} is the probability that a pion from D^{**} decay passes our cuts for prompt pion candidates.

The background shape and the efficiencies for finding pions from D^{**} and kaons from B_s^{**} are calculated from the Monte Carlo. For the properties of D^{**} mesons we use the default settings of QQ version 9.1. The masses of B_s^{**} states are set to the theoretical predictions from reference [16], which are in agreement with the evidence from referecne [19]. Table 7.1 lists the number we get.

The determination of the efficiencies for finding signal pions and B mesons is a little more involved, since we want to get an estimate of B^{**} mass as well as its
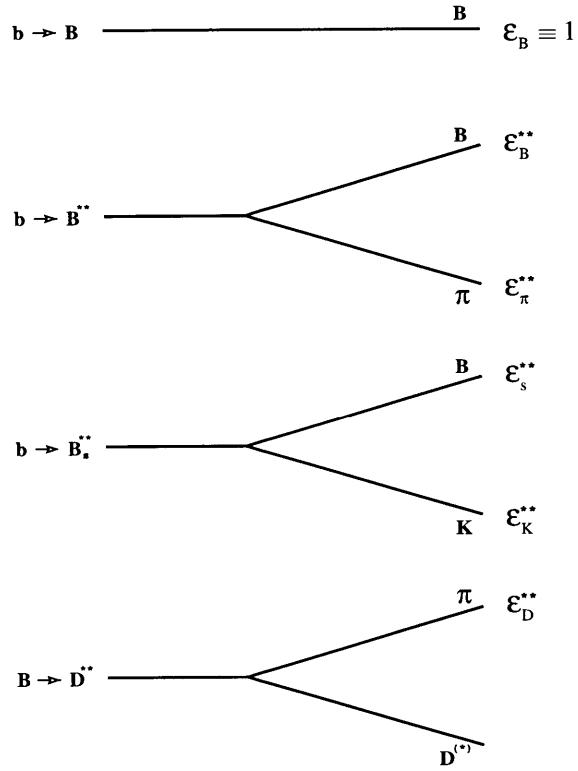
Figure 7-1: Diagram of efficiencies for finding particles from various processes.

ϵ_D^{**}	0.160 ± 0.009
ϵ_s^{**}	0.623 ± 0.025
ϵ_K^{**}	0.664 ± 0.064

Table 7.1: Efficiencies.

production fraction. We generate samples with a wide range of B^{**} masses, and calculate these two efficiencies as a function of B^{**} mass. The results are shown in figure 7-2.
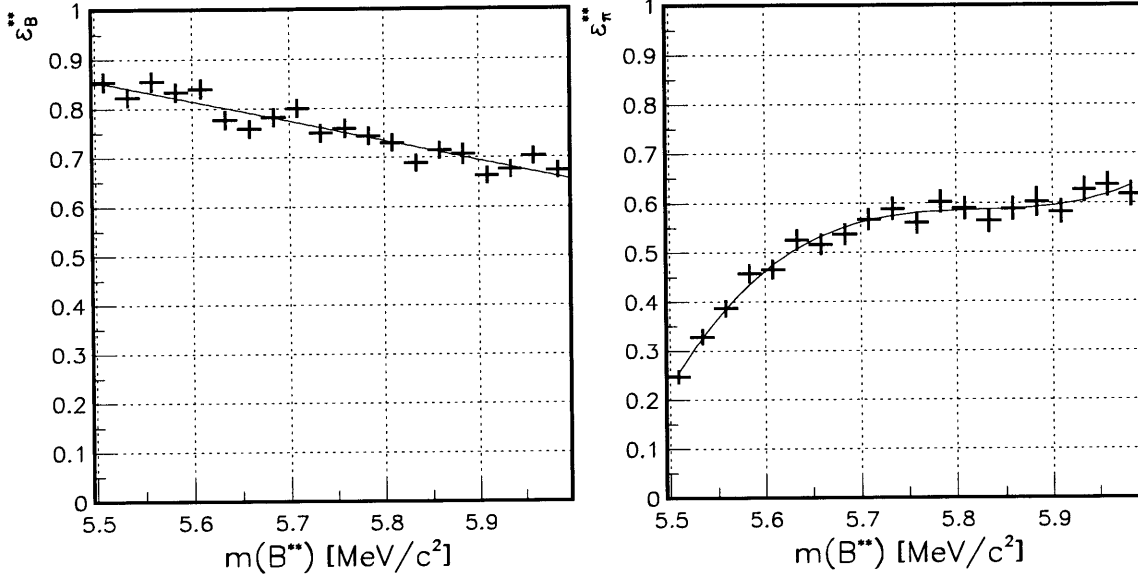
Figure 7-2: Dependence of ϵ_B^{**} and ϵ_π^{**} on the B^{**} mass.

A common correction is applied to all the track efficiencies (*i.e.* ϵ_π^{**}, ϵ_D^{**} and ϵ_K^{**}) to account for the fact that the Monte Carlo simulates tracking efficiencies from Run 1B and doesn't take into account the instantaneous luminosity effects or the time-dependent degradation of the detector. The resulting tracking efficiencies are set to agree with the numbers from references [46] and [47].

7.2 Resonance Scan

The fitting procedure described in chapter 6 is implemented in Fortran using the MINUIT library. The relative complexity of the fitting procedure leaves plenty of room for mistakes. For a simple check, and to test the overall behavior of the fitter, we used a single Gaussian as the shape of the B^{**} excess and varied its mean and width over the region of interest. The results are shown in figures 7-3, 7-4 and 7-5.

126

A distribution $138 \pm 25\,\text{MeV}/\text{c}^2$ wide at $Q_{mean} = 236 \pm 24\,\text{MeV}/\text{c}^2$ results in the best fit and the fitted fraction $h^{**} = 0.350 \pm 0.060_{stat} \pm 0.053_{syst}$ (see section 7.4 for the explanation of errors). The shape of the fitted contributions is shown in figures 7-6 and 7-7. The smooth curve is the fitted shape of the hadronization component alone—the $y = 0$ line corresponds to the combined underlying event, pile-ups and D sidebands. The dotted histograms are the sum of all backgrounds, so the difference between the solid and the dotted histograms is the fitted B^{**} excess.
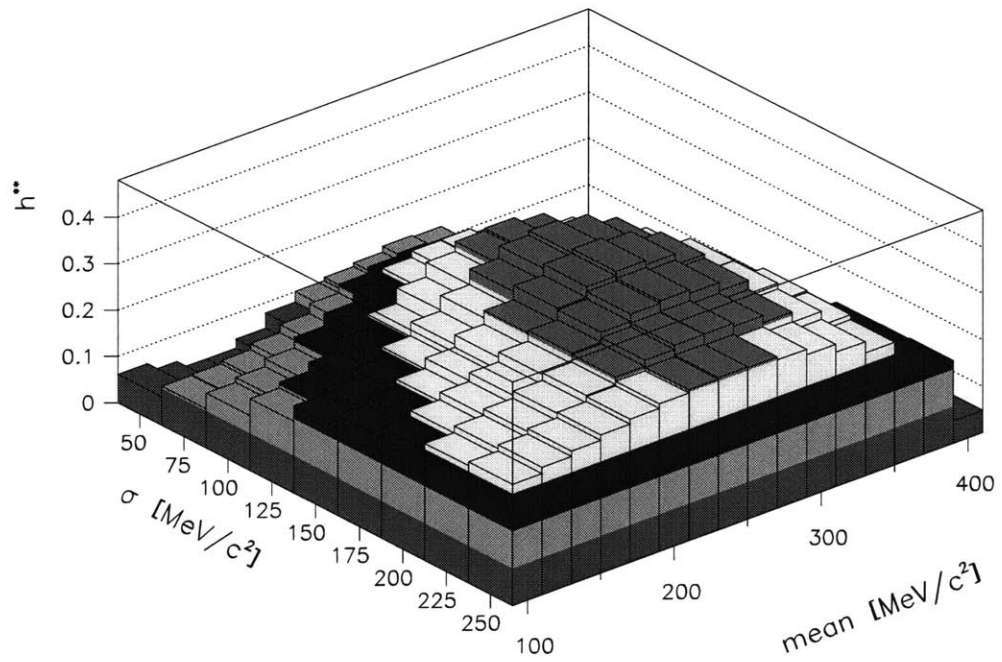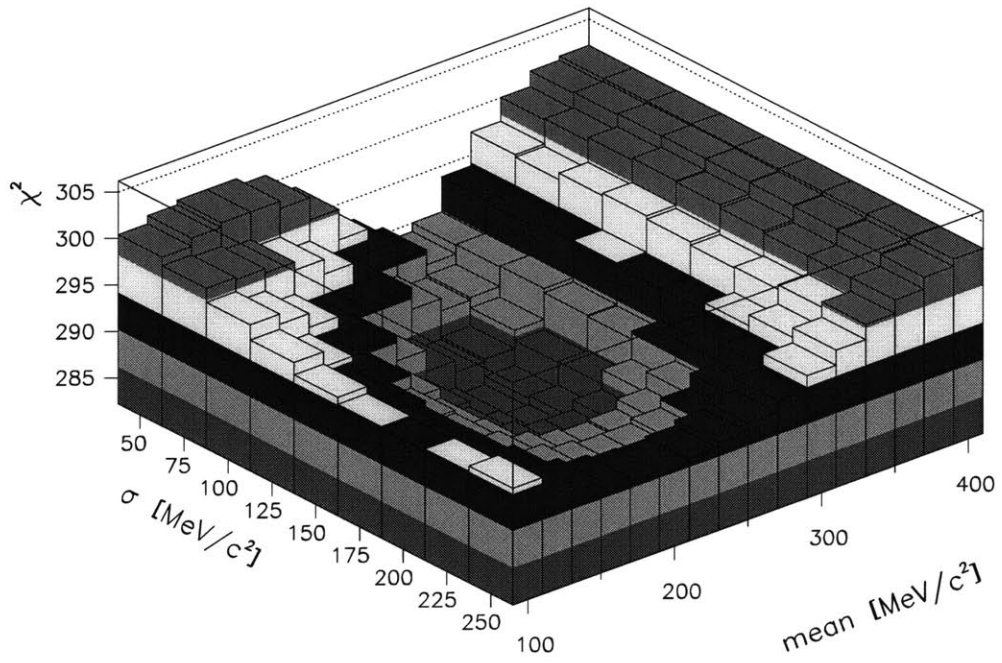
Figure 7-3: Dependence of the fit χ^2 and the fitted B^{**} production fraction on the parameters of the Gaussian distribution. The z-axis color levels cover 5 units of χ^2 (top plot) and 0.08 units of h^{**} (bottom plot).
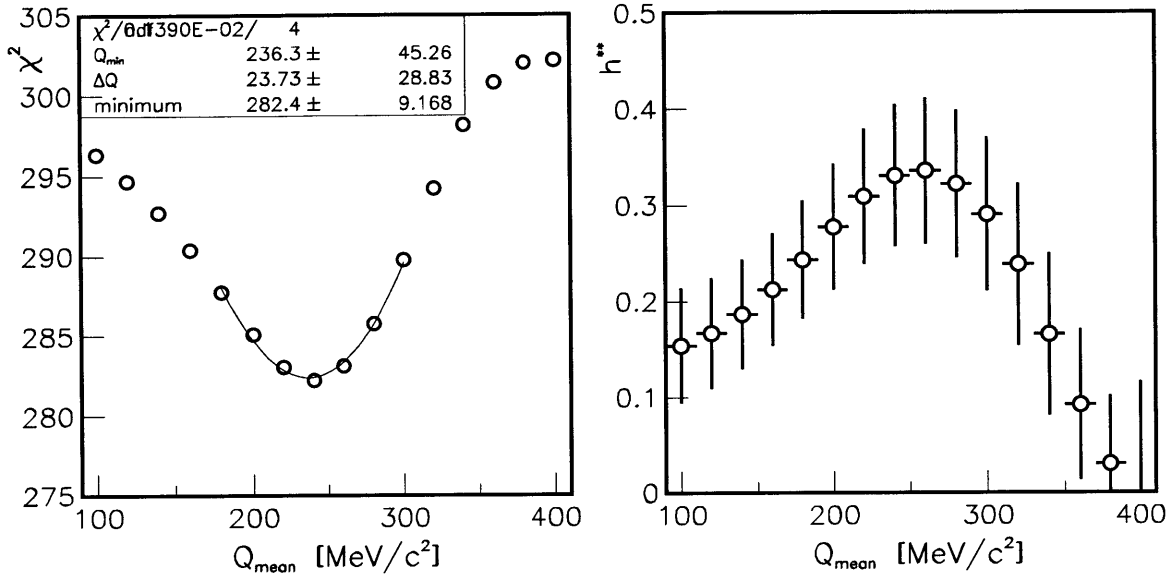
Figure 7-4: Dependence of the fit χ^2 and the fitted B^{**} production fraction on the mean value of the Gaussian distribution.
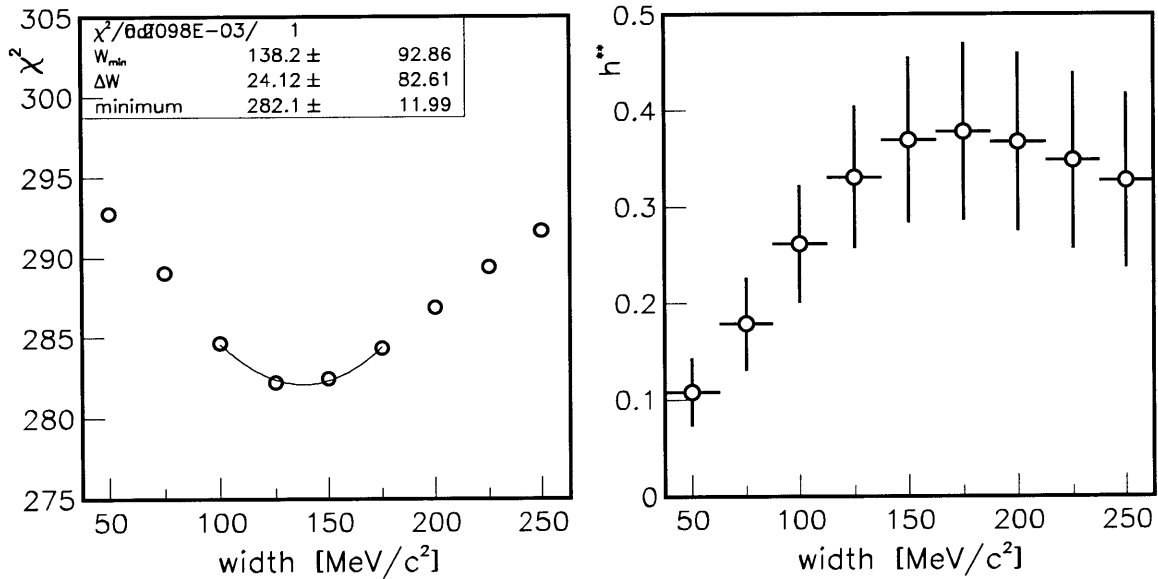
Figure 7-5: Dependence of the fit χ^2 and the fitted B^{**} production fraction on the width of the Gaussian distribution.

Right Sign
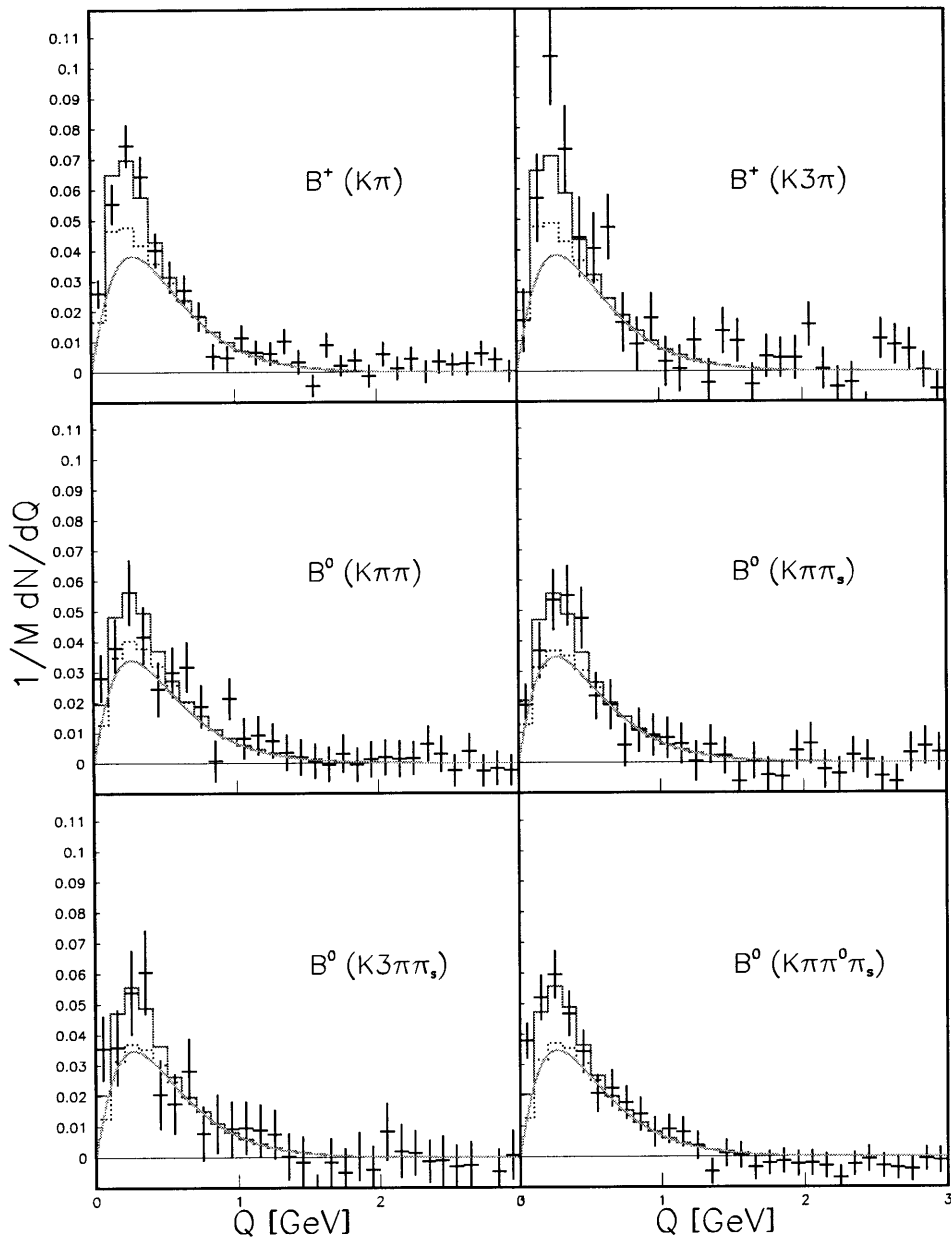
Figure 7-6: The fitted distributions for the right-sign tracks. The points with error bars are the values measured in the data; the smooth curves are the fitted contribution from the hadronization tracks; the dotted histograms are the sum of all backgrounds, and the solid histograms include the fitted signal as well.
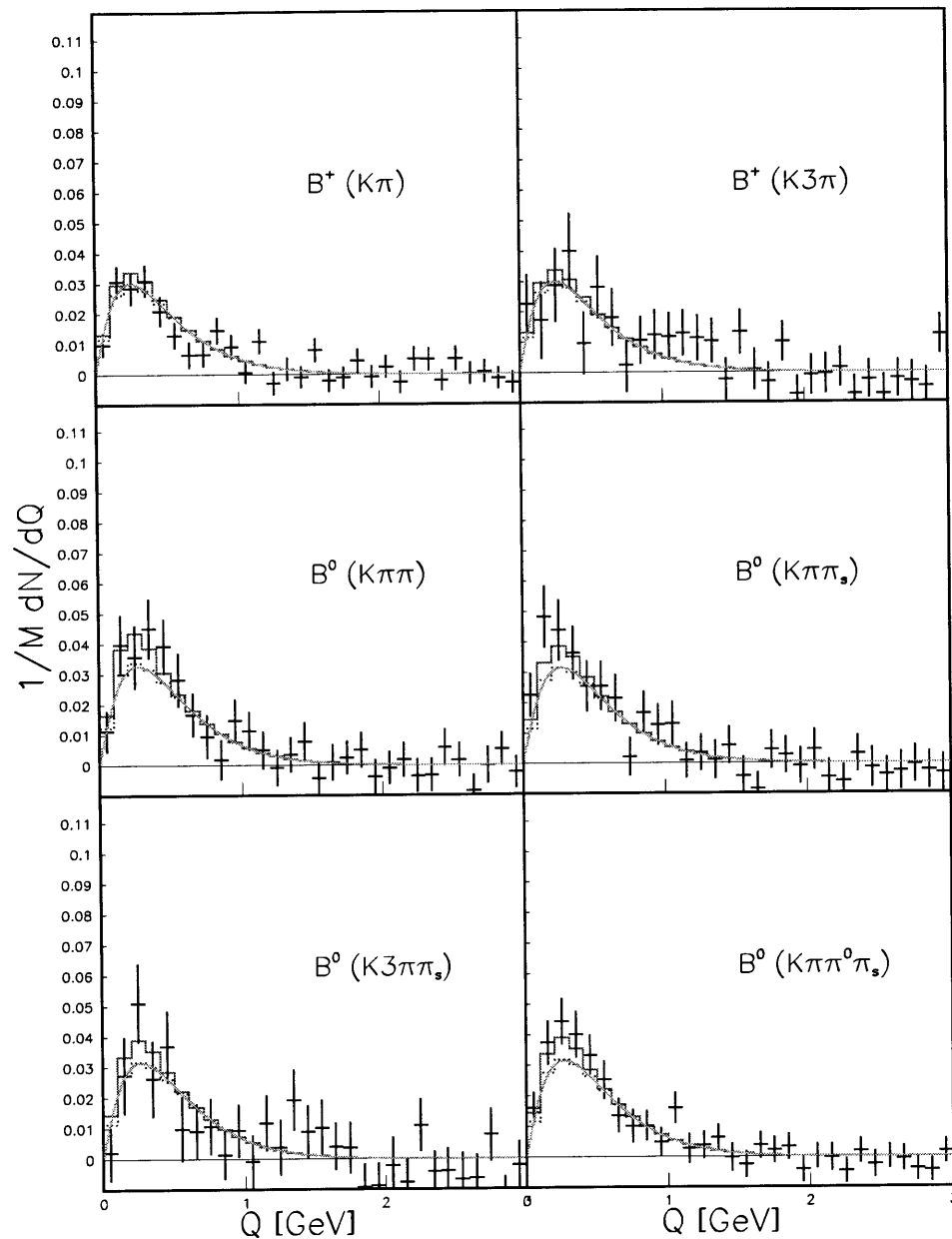
Figure 7-7: The fitted distributions for the wrong-sign tracks. The points with error bars are the values measured in the data; the smooth curves are the fitted contribution from the hadronization tracks; the dotted histograms are the sum of all backgrounds, and the solid histograms include the fitted signal as well.

7.3 Results of the Mass Fit

The splitting between the four B^{**} states is caused by the chromodynamic interaction between the two quarks that is the analog of the hyperfine splitting in atomic physics. All the theoretical models of heavy-light mesons make a much stronger statement about the magnitude of this splitting than about the mass difference between the 2P states and the ground states of the mesons. For this reason, and also because we cannot distinguish the four resonances in the semileptonic B sample, when measuring the most likely mass of the B^{**} states we move all the 2P masses together without changing their splitting.

There is, however, some controversy about the splitting between the broad and the narrow resonances. While all the models predict 12–$15 \, \mathrm{MeV/c^2}$ mass difference between the two narrow states and 0–$19 \, \mathrm{MeV/c^2}$ between the two broad ones, recent work [15, 16] suggests that the broad resonances actually have higher mass than the narrow ones, contrary to naive expectations based on atomic spectra. To try to gain more insight on this question, we varied the masses of the narrow and the broad states separately and observed the behavior of the fit.

The results are shown in figure 7-8. It is obvious from the shape of the χ^2 that the broad states have very little effect on the fit—changing their mass by $300 \, \mathrm{MeV/c^2}$ moves the most likely mass of the narrow states by less than $50 \, \mathrm{MeV/c^2}$.

The choice of the splitting between the narrow and the broad states selects a diagonal slice through the two-dimensional histograms in figure 7-8. We show two such slices, one for the splittings we started with (from reference [14]) in the top half of figure 7-9, and another for the most recent predictions from reference [16] in the bottom half of figure 7-9 (the splittings are shown in table 1.1). Using the mass of the narrowest state ($\mathbf{J} = 1$, $\mathbf{J}_q = \frac{3}{2}$) as a tag, we find that the most likely mass of the B^{**} mesons is $5732 \pm 22 \, \mathrm{MeV/c^2}$ in the former and $5709 \pm 20 \, \mathrm{MeV/c^2}$ in the latter case. The fitted production fractions for these masses are $h^{**} = 0.292^{+0.054}_{-0.058} stat^{+0.042}_{-0.035} syst$ and $h^{**} = 0.276^{+0.056}_{-0.059} stat^{+0.033}_{-0.029} syst$ respectively (see section 7.4 for explanation of

132

errors).

The shape of the fitted contributions for the EGF mass distribution is shown in figures 7-10 (right-sign tracks) and 7-11 (wrong-sign tracks). Figure 7-12 combines the decay signatures with similar composition.
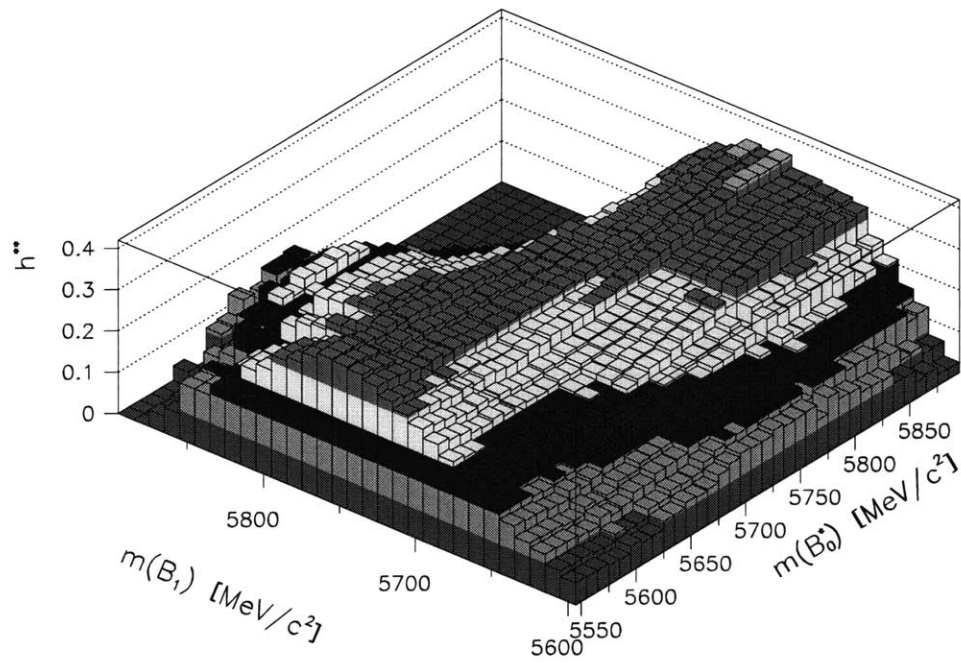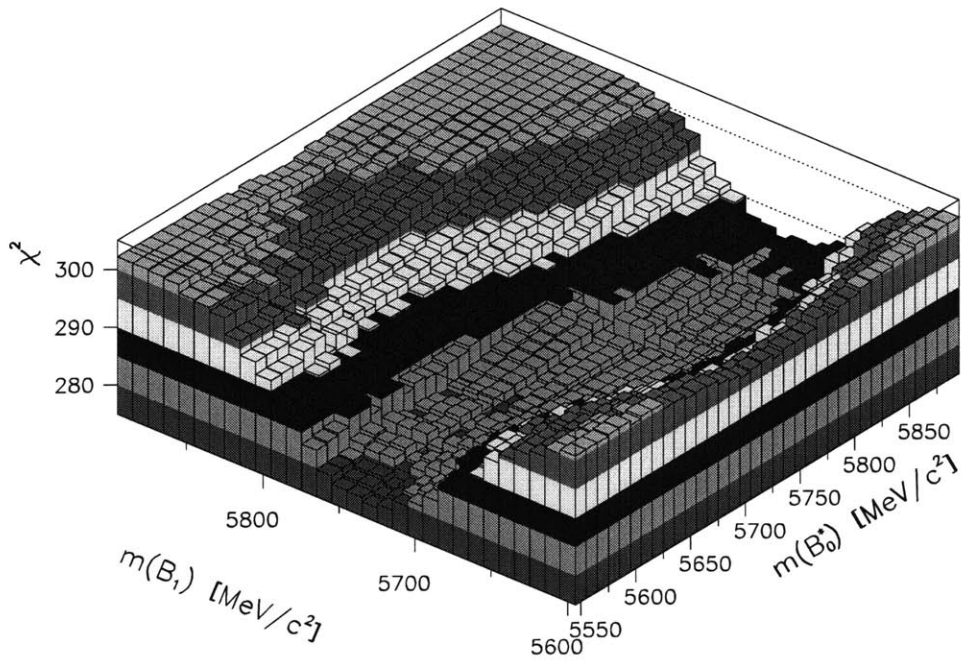
Figure 7-8: χ^2 of the fit and the fitted B^{**} production fraction as a function of the mass of the B^{**} states. The left (right) axis is the mass of the two narrow (wide) states. The z-axis color levels cover 5 units of χ^2 (top plot) and 0.07 units of h^{**} (bottom plot).

Figure 7-9: χ^2 of the fit and the fitted B^{**} production fraction as a function of the mass of the B^{**} states. The mass shown on the x axis is that of the narrow $J=1$ state, and the mass splittings in the top (bottom) histograms are labelled EHQ (EGF) in the text.
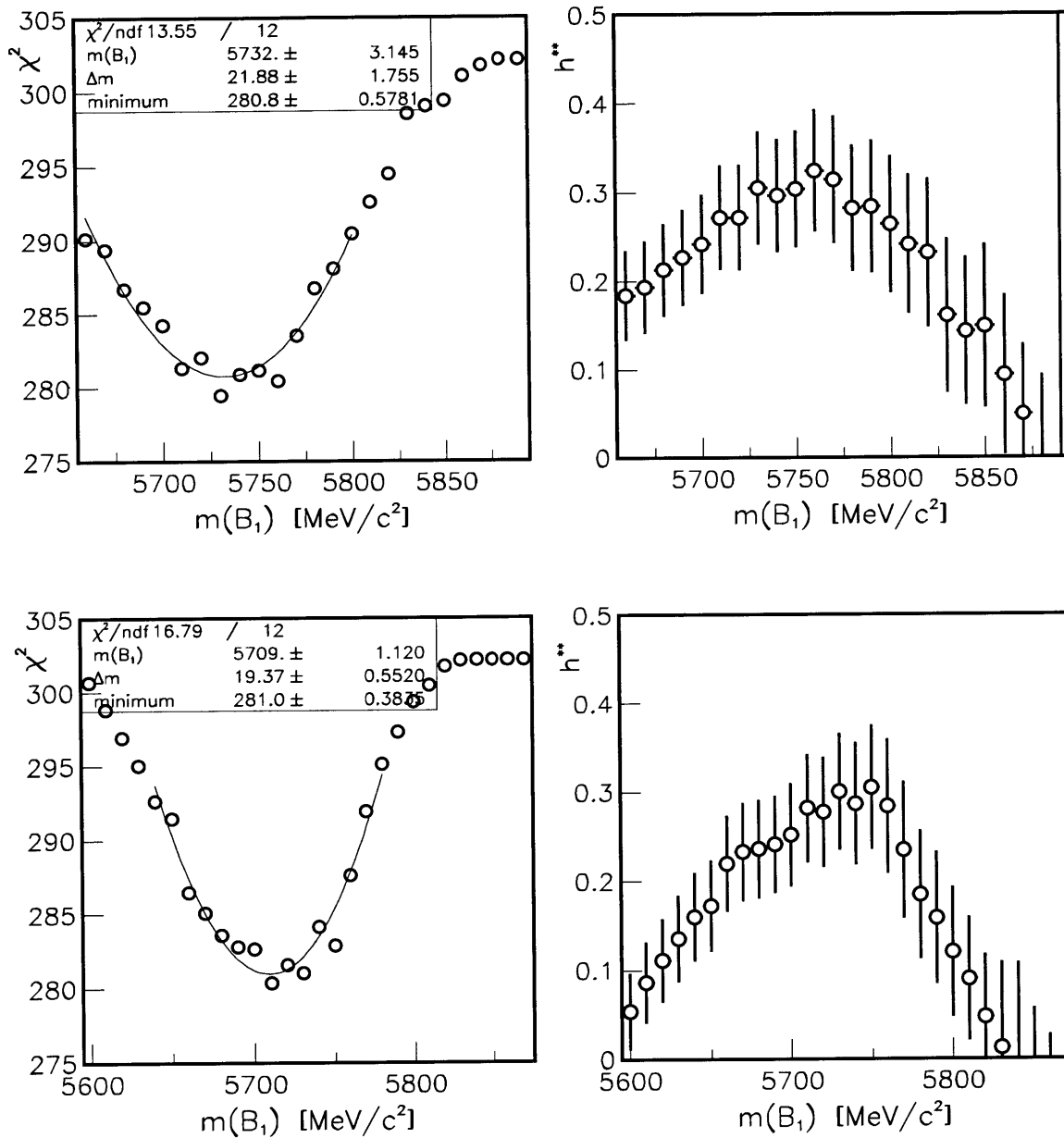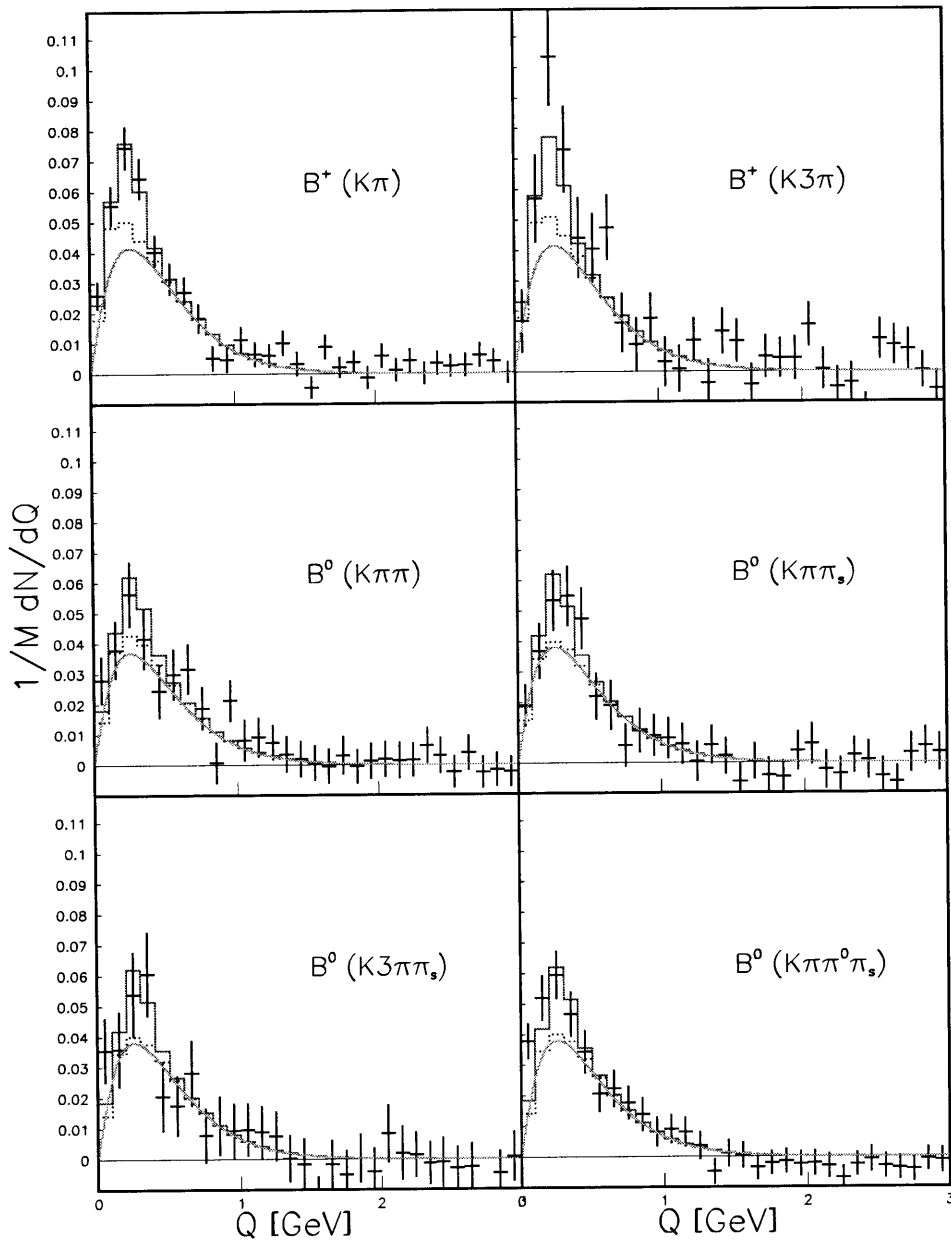
Figure 7-10: The fitted distributions for the right-sign tracks. The points with error bars are the values measured in the data; the smooth curves are the fitted contribution from the hadronization tracks; the dotted histograms are the sum of all backgrounds, and the solid histograms include the fitted signal as well.

Wrong Sign
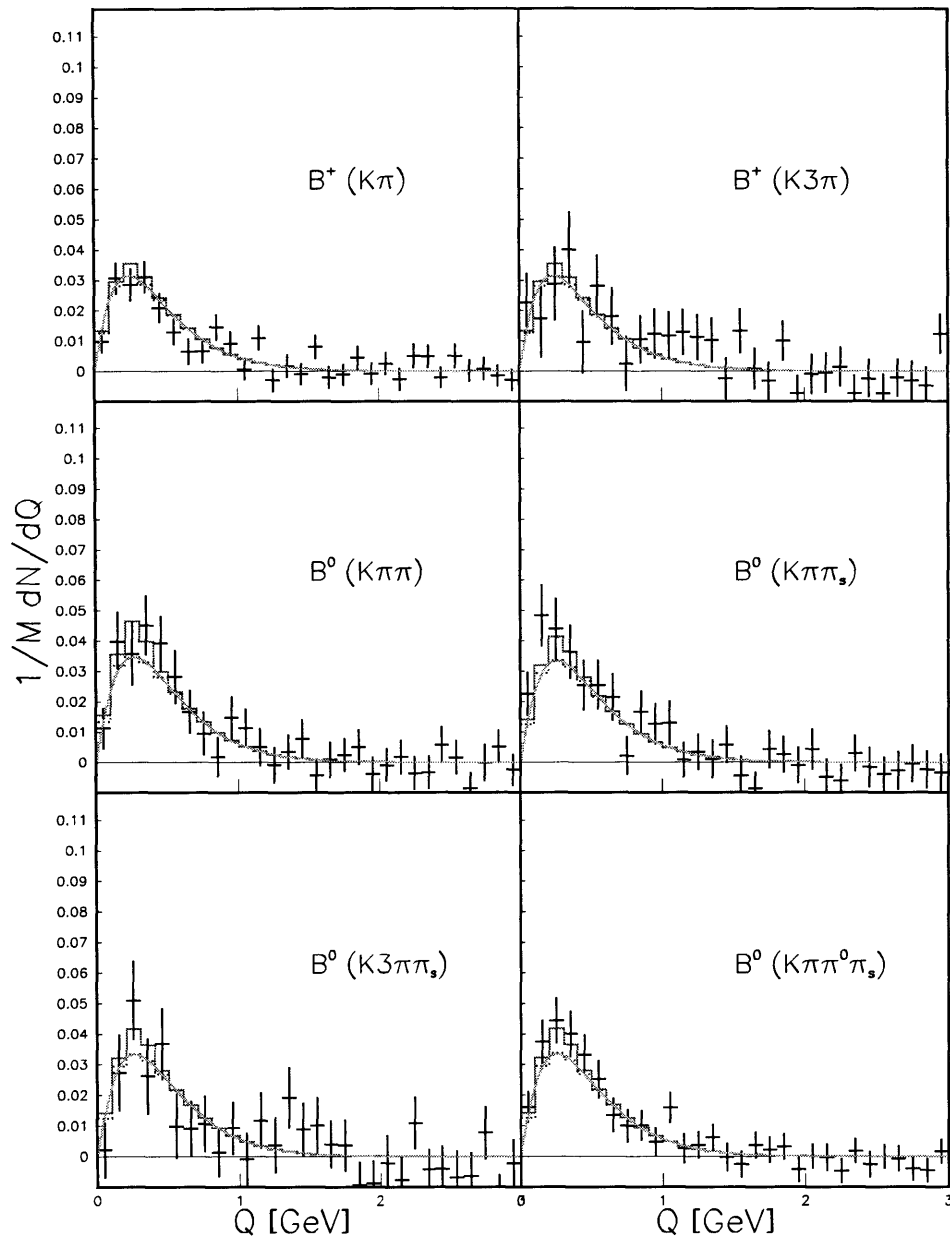
Figure 7-11: The fitted distributions for the wrong-sign tracks. The points with error bars are the values measured in the data; the smooth curves are the fitted contribution from the hadronization tracks; the dotted histograms are the sum of all backgrounds, and the solid histograms include the fitted signal as well.
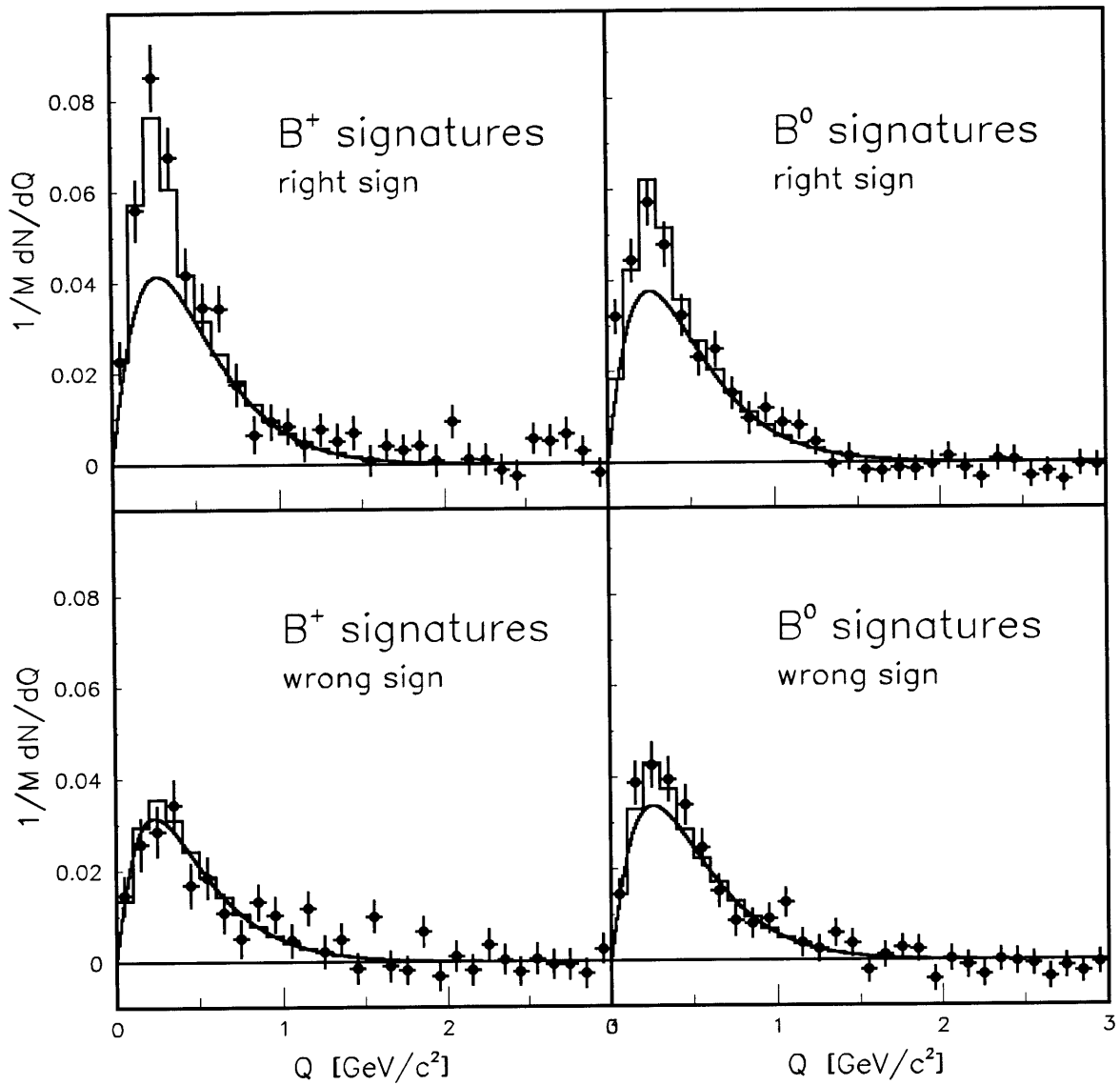
Figure 7-12: The distributions from the two previous figures with combined signatures that have similar composition.

138

7.4 Estimating Measurement Errors

Our estimate of backgrounds depends on the B^{**} production fraction and *vice versa*. This results in a very high level of correlation between some of the parameters in the fit. To avoid overestimating the systematic error, instead of varying each of the parameters in turn by its uncertainty, we leave all of the parameters floating in the fit and add the appropriate terms to the χ^2 function, as shown in chapter 6.

The error calculated in such a "big" fit is then a combination of the statistical and the systematic error. In order to separate the statistical contribution from the systematic, we fix all the external parameters (the ones that are not calculated from our data sample) after the fit converges and refit. The error returned from this "small" fit is the sought statistical error. To get the systematic error we subtract in quadrature the statistical part from the total error we got from the "big" fit.

Statistical Uncertainties		
sample size	−0.0289	+0.0285
algorithm	−0.0479	+0.0449
parameters	−0.0096	+0.0107
total	−0.0567	+0.0543
Systematic Uncertainties		
correlated	−0.0131	+0.0234
HA asymmetry	−0.0232	+0.0200
gluon splitting	−0.0048	+0.0055
total	−0.0271	+0.0312

Table 7.2: Listing of uncertainties.

The estimate of the systematic error obtained in this way takes into account the correlations between the different fit parameters, so we name it the "correlated" systematic error. This error is only a part of the total systematic uncertainty, though. To calculate the total error we have to add the "uncorrelated" contributions, namely the uncertainty in our estimate of the hadronization asymmetry and the presence of gluon splitting (section 6.6.1).

Table 7.4 lists all the measurement errors. To get the total systematic error we add in quadrature the correlated and the uncorrelated contributions.

The statistical error is split into three contributions. The "sample size" part is the pure statistical error—the hard limit resulting from the finite number of B mesons in the sample. The "algorithm" part is the statistical error that is a result of not using the shape of the hadronization component from other sources but rather measuring it in the fit; this error also depends on the size of the sample and is therefore statistical, but could conceivably be reduced by using other measurements or theoretical predictions to constrain this background. The same comment applies to the third part, which is due to the two fit parameters we measure in the same data sample, the R^* and the P_V.

Tables 7.3 and 7.4 contain more details of the fit: the input and output values of the parameters and the sample composition. The fitted fraction of B_s^{**} mesons in the sample is 3.7%.

7.4.1 Significance of the B^{**} Signal

Toy Monte Carlo

One of the main concerns of this analysis is the possibility that the backgrounds fluctuated to fake the signal. This fear is aggravated by the fact that the large difference between the asymmetries of the hadronization background and the signal is reduced by the unavoidable flavor mixing in the semileptonic B sample, so the observed difference is expected to be more modest.

To test the probability that the entire excess seen in the data is the result of a fluctuation of backgrounds, and as a further test of the sensitivity of the fitter, we set up a "toy" Monte Carlo generator which feeds randomized observations expected from a sample with known composition into the fitter. This procedure and the various tests we performed are described below.

Parameter	input value	input error	output value	output error	correlation with h^{**}
N_u			0.951	0.128	-0.670
N_d			0.919	0.124	-0.750
W			0.233	0.010	0.668
R	1.10				
P_V	0.331	0.282	0.425	0.240	0.187
ϵ_{π_s}	0.74	0.02	0.855	0.070	-0.074
R_f	2.5	0.6	2.334	0.626	0.046
f^{**}	0.36	0.12	0.321	0.106	0.157
τ_{B^+}/τ_{B^0}	1.02	0.05	1.033	0.049	-0.036
χ_{eff}	0.21	0.01	0.212	0.010	0.010
ϵ_B^{**}	0.763	0.012	0.764	0.012	-0.054
ϵ_π^{**}	0.531	0.015	0.532	0.015	-0.097
ϵ_D^{**}	0.160	0.009	0.160	0.009	-0.022
ϵ_s^{**}	0.623	0.025	0.623	0.025	-0.031
ϵ_K^{**}	0.664	0.064	0.666	0.063	-0.078
f_s/f_d	0.30	0.07	0.292	0.066	-0.215

Table 7.3: Details of the fit. The parameters in the upper part of the table contribute to the statistical uncertainty, the ones in the lower to the systematic. The latter are being floated in the fit so the correlations between them are accounted for when calculating the total systematic uncertainty.

Signature	$K\pi$	$K3\pi$	$K\pi\pi$	$K\pi\pi_s$	$K3\pi\pi_s$	$K\pi\pi^0\pi_s$
α_u	0.821	0.826	0.195	0.066	0.072	0.077
α_d	0.179	0.174	0.805	0.934	0.928	0.923

Table 7.4: Fitted sample composition.

Fitting the Background Only

The first step in the construction of a toy Monte Carlo generator is to make sure that the freely floating backgrounds (*i.e.* the hadronization tracks) are fitted correctly. To do this we calculate the expected shapes of all backgrounds and no signal, randomize these expectations according to the statistics of our data samples to get one "CDF experiment," fit many of these experiments and compare the outputs of the fitter with the inputs that went into the calculation of the background shapes.

At this stage we are interested in the statistical effects only, so all the constrained fit parameters are fixed to their central values in both the generator and the fitter.

Looking at all the backgrounds, the uncorrelated ones have already been subtracted and enter into the fit only through their contribution to the uncertainties, the B_s^{**} production is turned off since it is assumed to scale with the B^{**} production fraction, and B decay products are constant since the sample composition is fixed. What remains is the hadronization component and the three parameters controlling its shape: N_u, N_d and W (see section 6.6.1).

When fitting the data, we try to use as little information from the Monte Carlo as possible: recalling section 6.6.1, we only use the expectation of the asymmetry of the hadronization component and let the overall shape be constrained by the data. Here, however, we have to make a choice of the shape as well, since our goal is only to make sure the output values agree with the input values. We use the shape produced by the "tuned" Pythia Monte Carlo (see section 6.6.1 and reference [44]).

Knowing the contribution from all the background components, we perform the arithmetic of flavor mixing described in section 6 to get the twelve Q histograms: right-sign and wrong-sign tracks in each of the six signatures. These histograms are assigned uncertainties calculated in the respective data histograms, since these already take into account the sample size in the particular signature and the contributions from uncorrelated backgrounds (which are not simulated in the Monte Carlo); the only error being made in using the uncertainties from the data is in including the contribution of signal (if present) to the uncertainty, which is irrelevant for this step

Entries	10000
Mean	0.7080
RMS	0.6683E-01

input
0.707

Entries	10000
Mean	-0.4137E-01
RMS	1.006
χ^2/ndf 108.2	/ 87
Constant	319.4 ±	3.969
Mean	-0.3665E-01 ±	0.1013E-01
Sigma	0.9882 ±	0.7172E-02

Entries	10000
Mean	0.6678
RMS	0.5688E-01

input
0.668

Entries	10000
Mean	-0.5656E-01
RMS	1.001
χ^2/ndf 167.0	/ 86
Constant	322.7 ±	4.016
Mean	-0.5231E-01 ±	0.1014E-01
Sigma	0.9724 ±	0.7043E-02

Entries	10000
Mean	0.2514
RMS	0.8992E-02

input
0.251

Entries	10000
Mean	0.7677E-02
RMS	1.002
χ^2/ndf 108.4	/ 86
Constant	321.0 ±	3.976
Mean	0.6739E-02 ±	0.9997E-02
Sigma	0.9840 ±	0.7087E-02

Figure 7-13: Results of the toy Monte Carlo generation of backgrounds only. The three rows show the output distributions and pulls of the three parameters that are left floating in the fit. The solid vertical lines are the means of the output distributions; the dashed vertical lines are the input values.

143

and only results in a conservative estimate of the significance in the steps that follow.

Figure 7-13 shows the results of this exercise. The three rows of plots show the three parameters controlling the shape of the hadronization background. The left column are the distributions of the output values, with the means and the inputs values shown for each parameter; the means of the output distributions are in very good agreement with the input values. The right column are the distributions of the "pull," the difference between the input value and the output value divided by the output error, which show that the error estimates returned by the fitter are in good agreement with the output distributions (*i.e.* the widths of the pull distributions are consistent with 1).

Fitting with the Signal Included

After we have convinced ourselves that the backgrounds are being fit correctly, we want to show that the same is true of the expected signal. We perform the same procedure, but this time assume a certain probability for B^{**} production and mix in the signal and B_s^{**} background accordingly. In this series of fits the parameter describing the B^{**} production fraction, h^{**}, is left floating along with the three parameters from the previously described run. The distributions of output values and pulls of h^{**} are given in figure 7-14 for a number of different signal fractions. We see that the agreement is adequate, except for very low signal fractions where the constraint that h^{**} be positive biases the fit.

Significance of h^{**} Measurement

We can now esimate the significance of the signal we measure in the data. To do this, we use the toy Monte Carlo to generate backgrounds only, but perform the fit including a B^{**} component. This exercise tells us how often the background distributions fluctuate so that we get a B^{**} component equal to or greater than the one seen in the data. For this step, again, h^{**} is left free to float in the fit.

The distribution of fitted values of h^{**} from this series of fits is shown in figure 7-

144

Row 1 (left):
Entries 13000
Mean 0.2296E-01
RMS 0.2993E-01
input 0.00

Row 1 (right):
Entries 13000
Mean 0.4086
RMS 0.5978
χ^2/ndf 6429. / 40
Constant 540.2 ± 48.33
Mean −0.3765 ± 0.1859
Sigma 1.146 ± 0.6568E-01

Row 2 (left):
Entries 13000
Mean 0.1005
RMS 0.5545E-01
input 0.10

Row 2 (right):
Entries 13000
Mean 0.7793E-01
RMS 0.9136
χ^2/ndf 963.8 / 71
Constant 514.3 ± 6.033
Mean 0.1388 ± 0.8805E-02
Sigma 0.8347 ± 0.5931E-02

Row 3 (left):
Entries 13000
Mean 0.1993
RMS 0.5794E-01
input 0.20

Row 3 (right):
Entries 13000
Mean 0.6484E-02
RMS 1.008
χ^2/ndf 58.41 / 73
Constant 461.1 ± 5.046
Mean 0.1358E-02 ± 0.8951E-02
Sigma 1.008 ± 0.6617E-02

Row 4 (left):
Entries 13000
Mean 0.2993
RMS 0.5812E-01
input 0.30

Row 4 (right):
Entries 13000
Mean 0.1193E-01
RMS 1.007
χ^2/ndf 66.74 / 73
Constant 460.6 ± 5.048
Mean 0.5539E-02 ± 0.8954E-02
Sigma 1.008 ± 0.6637E-02

Row 5 (left):
Entries 13000
Mean 0.3997
RMS 0.5726E-01
input 0.40

Row 5 (right):
Entries 13000
Mean 0.1513E-01
RMS 1.008
χ^2/ndf 56.37 / 73
Constant 458.8 ± 5.052
Mean 0.1005E-01 ± 0.8989E-02
Sigma 1.013 ± 0.6760E-02

Row 6 (left):
Entries 13000
Mean 0.5000
RMS 0.5691E-01
input 0.50

Row 6 (right):
Entries 13000
Mean 0.2067E-01
RMS 1.012
χ^2/ndf 69.46 / 73
Constant 457.4 ± 5.046
Mean 0.1328E-01 ± 0.9012E-02
Sigma 1.015 ± 0.6804E-02

x-axis left: h^{**} (0, 0.2, 0.4, 0.6)
x-axis right: h^{**} pull (−2, 0, 2, 4, 6)

Figure 7-14: Output values and pulls of h^{**} if the signal is generated along with the backgrounds in the toy Monte Carlo generator. The rows correspond to different input values of h^{**}. The solid vertical lines are the means of the output distributions; the dashed vertical lines are the input values.

145
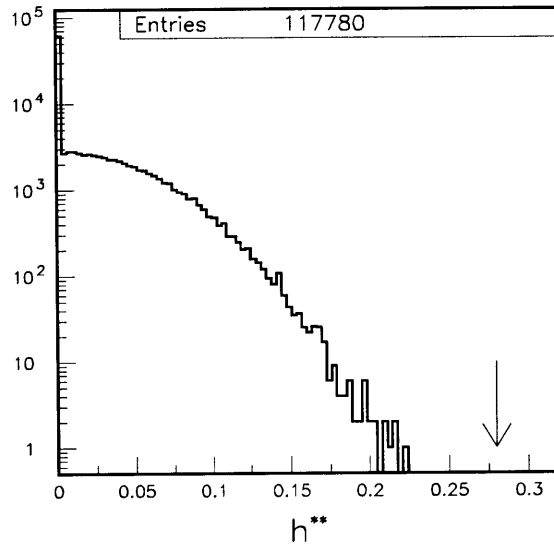
Figure 7-15: Output distribution of the fitted B^{**} fraction with only backgrounds generated. The arrow marks the value measured in the data.

15. The probability we seek is the fraction of fits that return h^{**} greater than the measured value. We see from the figure that none of the fits so far fluctuated as high as the data value; by fitting a gaussian function centered at zero to the returned h^{**} distribution excluding the first bin, we can estimate the probability that the backgrounds fake the measured signal to be 6×10^{-8}.

Systematic Effects

To test the worst-case scenario, we also have to take into account the systematic effects when calculating the significance of the excess: first we shift the value of every relevant parameter at the generation stage by one error in both directions and note how the probability of fluctuation changes if the fit is done with the central value; then we shift all the parameters in the direction that increases this probability and estimate the pessimistic significance from such a run.

Table 7.5 lists the values of the parameters used for the generation and for the fitting in the worst-case scenario; the corresponding distribution of returned B^{**} frac-

146
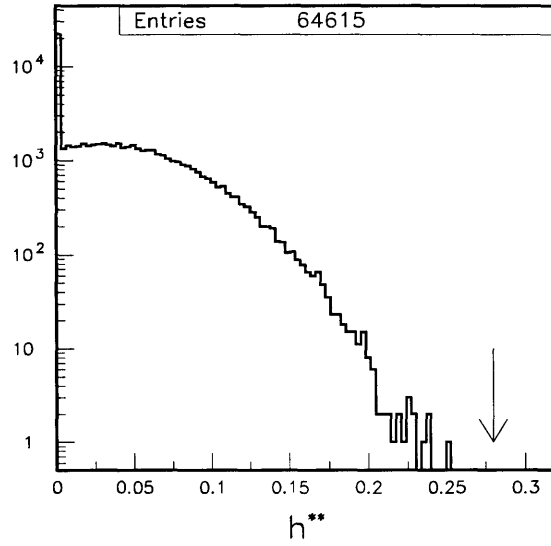
Figure 7-16: Output distribution of the fitted B^{**} fraction with only backgrounds generated. The parameters in this run have been shifted by one error in the generator so that the probability of background fluctuation is maximized. The arrow marks the value measured in the data.

tions is shown in figure 7-16. Extrapolating the distribution to the fraction measured in the data, we get the value 10^{-6} for the probability of background fluctuation.

Parameter	generator value	fitter value
P_V	0.049	0.331
R_f	1.9	2.5
f^{**}	0.24	0.36
τ_{B^+}/τ_{B^0}	1.07	1.02
χ_{eff}	0.20	0.21
ϵ_D^{**}	0.17	0.16
Asymmetry	default	tuned

Table 7.5: Parameter values used for the generation and for the fitting in the worst-case scenario toy Monte Carlo run.

Chapter 8

Conclusion

This work has established the feasibility of studying oribtally excited states of B mesons through semileptonic B decays in the complex environment of a hadron collider.

The most important building blocks of this analysis were:

- extracting a large sample of B events by using many partially reconstructed signatures of decays with large branching fractions, instead of using a much smaller sample of fully reconstructed mesons;

- looking for the excess in the mass difference between the partially reconstructed B meson and its composite with a pion, instead of looking for a B^{**} mass peak; using a corrected B momentum to improve the resolution on this mass difference;

- decomposing the prompt background into several components, and separating the components according to the type of their correlation with the B meson;

- deriving the magnitude of flavor mixing from measured quantities;

- recognizing that the signal can be distinguished from the b hadonization background by the different charge-flavor correlation with the B meson;

- constructing the procedure for simultaneous fitting of the signal and the hadronization background, which reduces the dependence on the parameters of the hadronization model and thereby diminishes the systematic uncertainty.

The most important (and the least plausible) assumptions we had to make in order to carry out the measurement are:

- the region of space between $\Delta\phi = 1$ and $\Delta\phi = 2$ with respect to the B meson direction is populated only with the underlying event tracks, which are not correlated with the properties of the meson;

- the B^{**} meson hadronizes in the same way as its ground state;

- the shape of the hadronization background is the same around neutral and charged mesons (but the normalizations and the asymmetries may be different).

The measured production fraction and mass of B^{**} mesons are summarized in table 8.1. The probability that the backgrounds fluctuated to fake the measured fraction is estimated at less than 10^{-6}.

Model	EHQ	EGF
$m(B_1)$ (J= 1, $J_q = \frac{3}{2}$)	$5732 \pm 22\,\mathrm{MeV/c^2}$	$5709 \pm 20\,\mathrm{MeV/c^2}$
h^{**}	$0.287^{+0.053}_{-0.057}stat^{+0.040}_{-0.034}syst$	$0.278^{+0.054}_{-0.057}stat^{+0.031}_{-0.027}syst$

Table 8.1: Summary of the measured B^{**} properties.

Besides improved measurements of the production fractions and masses, probably the most important goal of the future B^{**} and D^{**} analyses is the observation of the still unobserved broad states, *i.e.* resolving the four resonances. The intrinsic limitations on the B^{**} mass resolution in the semileptonic B samples make them an unlikely candidate for such an observation. Fortunately, the fully reconstructed B samples offer an order of magnitude better mass resolution, and will grow significantly in the near future.

It is obvious from this work that study of excited B mesons relies heavily on understanding the non-perturbative process of hadronization of b quarks, and *vice versa*. While we have treated the latter as a background, it is likely that significant further improvements lie in understanding exactly the interplay between these two sources of prompt tracks. This is especially important for the construction of better B flavor taggers, where the goal is to find the quantity with the maximal correlation with the B flavor.

Appendix A

Monte Carlo Tuning Procedure

In chapter 5 we discussed the different sources of background particles B mesons are immersed in. Some of these tracks (expected to be near the observed mesons) originate in the hadronization of the b quarks, while others are simply labeled as "underlying event" and encompass the rest of the $p\bar{p}$ interaction that produced the $b\bar{b}$ system.

In this analysis we rely on the Monte Carlo calculation to predict the relative abundance of right-sign and wrong-sign particles coming from b hadronization. More generally, the analyses [12, 40] that utilize the Same-Side Tagging technique, where the flavor of the B meson is determined by the charge of one or more tracks that accompany it, can benefit from an accurate Monte Carlo simulation of $p\bar{p}$ events.

We use the PYTHIA 5.7/JETSET 7.4 Monte Carlo to generate $b\bar{b}$ events. Unfortunately, the default PYTHIA settings do not describe the data very well, so we invested a significant effort into tuning this generator to better agreement with our data. This appendix describes the tuning procedure; it is an abbreviated version of reference [44].

A.1 Dataset

The dataset used for the tuneup is the subset of the sample described in chapter 3, namely the $\bar{D}^0 \to K^+\pi^-$ signature. The main reason for this choice is that the ℓD^0

152

signatures contain predominantly charged B mesons, so we can avoid correcting for $B^0 - \bar{B}^0$ mixing to first order, and this particular signature was well understood at the time the exercise was done.

The D^0 mass peak, after the standard D^* subtraction, is shown in the first plot in figure 3.1.1. In all plots that follow the corresponding distributions from the D sidebands have been subtracted.

We only look at prompt tracks that pass the following cuts:

- not an identified B decay product;

- $p_T > 400\,\text{MeV}/c$;

- three or four SVX hits;

- originate less than $5\,\text{cm}$ in z away from the ℓD vertex;

- CTC exit radius $> 130\,\text{cm}$;

- $d_0/\sigma(d_0) < 3.0$.

Figure 5-2 shows the $dN/d\Delta\phi$ distribution with respect to the B direction of tracks that pass all of these cuts and are within $|\Delta\eta| < 1$ of the ℓD direction. In the distribution we can clearly see an excess of tracks (presumably from hadronization) near the B, and a separate component, independent of the direction relative to the B axis (the solid line marks the fitted region; the dotted line is the continuation of the fit, and shows the expected contribution of this component to the region close to the B direction). We call this flat component the "underlying event." Its isotropy in the transverse plane is verified in the same distribution for tracks far in η ($|\Delta\eta| > 1$) from the B axis. Figure 5-3 shows that there is no significant angular dependence. The difference between the total track multiplicities observed in the $|\Delta\eta| < 1$ and $|\Delta\eta| > 1$ regions is a consequence of a rapid drop in acceptance for tracks at high $|\eta|$, caused mainly by the exit radius cut.

Guided by these observations, we define the "near" region to be the part of phase-space in a cone of $\Delta R < 1$ with respect to the ℓD axis, and the "far" region to be the

region $1 < \Delta R < 2$. This definition is the same as the one used in the underlying event-subtraction procedure described in chapter 5. The near region contains most of the B jet, and the far region is dominated by the transverse-angle-independent distribution of tracks from the underlying event.

Figure A-1 shows a comparison of spatial distributions of tracks in the data and the Monte Carlo with the default settings. Clearly, there are too few tracks far away from the B direction, in the $\Delta R > 0.3$ region. A closer look at the transverse momentum distribution of tracks reveals that the Monte Carlo produces a much softer distribution than the one observed in the data (figure A-2). The latter problem is even more pronounced far away from the B direction (figure A-3), so we conclude that the improper modelling of the underlying event is the main cause for the observed discrepancy.
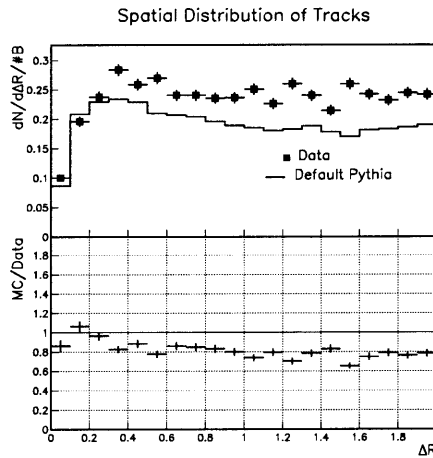
Figure A-1: Comparison of the multiplicity of charged tracks (per B meson) in the data (points) and the Monte Carlo (histogram) as a function of the distance in η-ϕ from the B meson direction. The bottom plot is the ratio of the Monte Carlo and data histograms from the top plot. It shows that the default Monte Carlo generates too few charged tracks more than 0.3 in ΔR away from the B meson.

154

Near Region (ΔR<1)
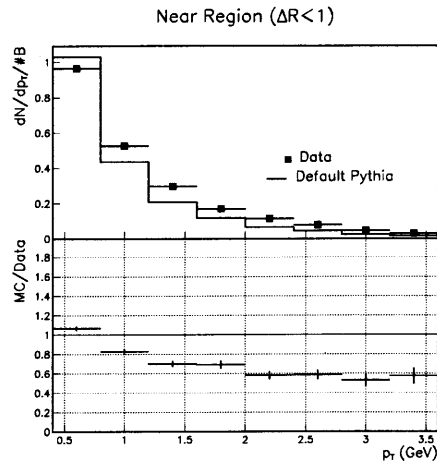
Figure A-2: Comparison between data and Monte Carlo of the p_T spectra of charged tracks within $\Delta R<1$ of the B meson. The bottom plot is the ratio of the Monte Carlo and data histograms from the top plot. It shows that the Monte Carlo with the default settings generates too soft a track p_T distribution.

Far Region (1<ΔR<2)
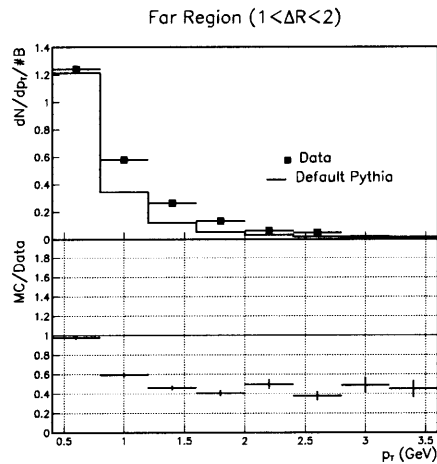
Figure A-3: Comparison between the data and the Monte Carlo of the p_T spectra of charged tracks far away in ΔR from the B. The discrepancy seen in the previous plot is even more pronounced in this region than near the B, suggesting that the main reason for the disagreement is inadequate modelling of the underlying event.

155

A.1.1 The Plan

Our plan of action is as follows (see figure 5-2):

1. Concentrate on the far region and tune the p_T and $dN/d\Delta\phi$ distributions of underlying event tracks to agree with the data.

2. Armed with a better underlying event, turn to the near region. The underlying event component of tracks in the near region should now be modelled well (see figure 5-3), so we can tune the hadronization part.

3. Choose the b fragmentation parameters so that the multiplicity in the near region agrees with the data. Count only tracks of wrong sign (*i.e.* $B^+\pi^+$) since the (still undetermined) fraction of wrong sign pions from B^{**} decays is very much smaller than that of right sign pions. Verify that the p_T distribution of tracks in the near region still agrees with the data.

4. Go back to step 1 if step 3 affects the far region.

5. Repeat steps 1–4 after measuring the fraction of B^{**} production.

A.2   Structure of Underlying Event

The prompt particles generated by PYTHIA come from three main sources:

- **beam remnants** are colored leftovers of the proton and the antiproton that hosted the primary hard scattering; the breakup of the color string leads to the production of charged particles that occasionally end up in the region of space that we are interested in;

- **multiple interactions** are independent secondary (tertiary, *etc.*) "semi-hard" scatterings *in the same* p$\bar{\text{p}}$ *collision*, unlike

- **pile-up events** which are additional hard scatterings in other p$\bar{\text{p}}$ pairs that interact in the same beam crossing; these are relevant only when they occur so

close in z to the primary hard interaction that the tracking cannot distinguish between the two primary vertices.

(Note that in PYTHIA language, "multiple interactions" are what is sometimes referred to as double-parton scattering. This naming convention is confusingly different from the widely accepted practice of referring to multiple p$\bar{\text{p}}$ collisions in the same beam crossing as multiple interactions—these are called "pile-up events" in PYTHIA.)

A.2.1   Pile-ups and Luminosity Effects

The default PYTHIA settings do not include a simulation of pile-ups. The magnitude of this contribution depends directly on the average number of collisions in a crossing, so we investigated the dependence of the properties of the underlying event on instantaneous luminosity.

To measure the pollution from tracks coming from other p$\bar{\text{p}}$ collisions, we plot the distance in z from the B vertex of tracks that pass all of our track cuts except the $|\Delta z| < 5\,\text{cm}$ cut (figure 5-1). We look at both the near and the far region. The narrow peak ($\approx 1\,\text{cm}$ wide) at $\Delta z = 0$ are tracks from the B vertex—its shape characterizes our z resolution. The shape is not described well by a single Gaussian, so we fit a sum of two Gaussian functions to measure the number of tracks in the peak. The wide distribution under the peak is attributed to tracks from other p$\bar{\text{p}}$ collisions. It has a Gaussian shape with $\sigma \approx 20\,cm$. From the fit we calculate the total contribution from pile-ups to be $5.1 \pm 0.1\%$.

Instead of trying to simulate this background in the Monte Carlo (which would require an independent tuning of minimum bias events), we do a simple Δz sideband subtraction in a manner similar to the subtraction of sidebands of the D mass peak. The sidebands are shown as shaded areas in figure 5-1. The multiplicity of tracks in these sidebands is expected to depend on the instantaneous luminosity. Indeed, the shaded histogram in figure A-4 confirms that the fraction of tracks from other primary vertices rises with luminosity.

Effect of Luminosity on Track Multiplicity (Data)
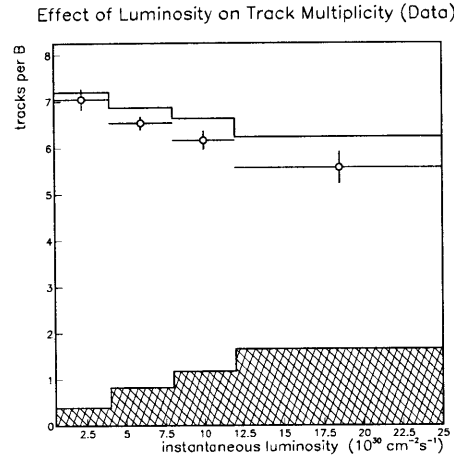
Figure A-4: The dependence of the track multiplicity in B events from Run 1b on instantaneous luminosity. The solid histogram is the multiplicity in the $|\Delta z| <$ 5 cm region. The shaded histogram is the multiplicity in Δz sidebands as shown in figure 5-1. The points are the resulting sideband-subtracted multiplicity of tracks that originated at the $b\bar{b}$ primary vertex.

Another effect is evident from figure A-4: after subtracting the D and the Δz side-bands, the total multiplicity of tracks in B events drops with increasing instantaneous luminosity. This is presumably an inefficiency in track reconstruction caused by high CTC and SVX occupancies. To correct for this inefficiency, we fit a linear function to the observed dependence and weigh each data event based on this fit. With the luminosity profile of the B sample taken into account, the run-averaged track-finding efficiency from this effect alone is calculated to be $85 \pm 5\%$ in Run 1b (the Run 1a B sample has been left out of the calculation because the SVX efficiency was different from that of SVX', the range of instantaneous luminosity was smaller, and the number of collected B events is too small to make a useful measurement). To reduce the error on this efficiency, we measure the same dependence in the much larger W sample (see reference [44]), and use that parametrization instead—the $89 \pm 2\%$ seen in the Run 1b W data is in agreement with the B result.

Comparison of Track p_T Spectra

The Δz sidebands give us the opportunity to compare the properties of the underlying event in $b\bar{b}$ events with the properties of tracks produced in minimum bias collisions. Figure A-5 shows the ratio of the p_T spectra of tracks in the Δz "signal" and "sideband" regions that are in the far region with respect to the B direction. Evidently the spectra are different (the $b\bar{b}$ underlying event is harder), so we conclude that minimum bias events cannot be used as a model of the underlying event in $b\bar{b}$ events.
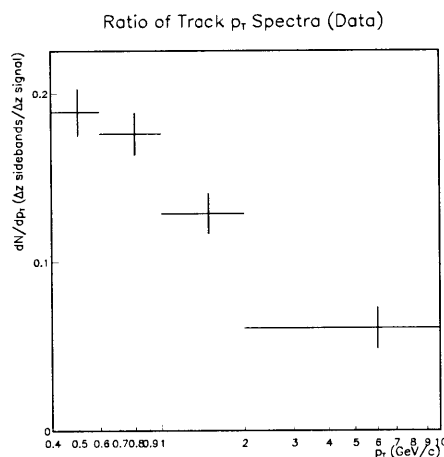
Figure A-5: The ratio of p_T spectra of tracks coming from minimum bias collisions (Δz sidebands from figure 5-1) and tracks from the underlying event of the primary vertex that produced the b quarks. Tracks coming from the $b\bar{b}$ vertex are harder, which implies that minimum bias events cannot be used to model the underlying event in heavy-flavor production.

A.2.2 Multiple Interactions and Beam Remnants

The default behavior of PYTHIA is to include multiple interactions simulated according to a "simple" model: in all events the probability of a secondary hard scattering is the same. These can be turned off, and also the model that determines their properties can be changed. They are a necessary ingredient—without multiple interactions the generated track multiplicity is more than a factor of two lower than the observed

one.

Three kinds of secondary hard interactions are supported by PYTHIA: connected gluon pairs, disconnected gluon pairs, and disconnected quark pairs.[1] By default these three contributions are generated in equal proportions, but their relative abundance is not known from first principles or from measurements, so we ended up using only connected gluon pairs as they require less "stretching" of other parameters to reproduce the distributions seen in the data.

The properties of particles originating from beam remnants are influenced indirectly by a very large subset of PYTHIA parameters, since b quarks (and occasionally the products of multiple interactions) are connected to them by color strings. The few parameters that directly control *only* the behavior of beam remnants, such as MSTP(94) and PARP(94–98), we left at their default values.

A.2.3 Detector Simulation

The number of events we are able to generate and reconstruct using the full detector simulation is severely limited by the available CPU resources, so we resort to a "fast" Monte Carlo generator which can show us the trends of various properties of generated events as we change the input parameters. This fast generator doesn't have any detector simulation in it, so before we look at the results we have to run all the numbers through a crude acceptance×efficiency parametrization. The acceptance and efficiency are determined by generating a sample of events using the full Monte Carlo and comparing the numbers of generated and reconstructed tracks. Figure A-6 shows the coarse structure of our code; the fast Monte Carlo is outlined by the dotted ellipse.

A typical use for the fast Monte Carlo is shown in figure A-7. This is a set of runs investigating the effect of the $\sigma_{p_T}^{frag}$ parameter (explained below) on the resulting

---

[1] "Connectedness" here refers to whether the products of the secondary scattering are connected by color strings to the rest of the event. Connected pairs result in events with fewer soft tracks transverse to the beam line.
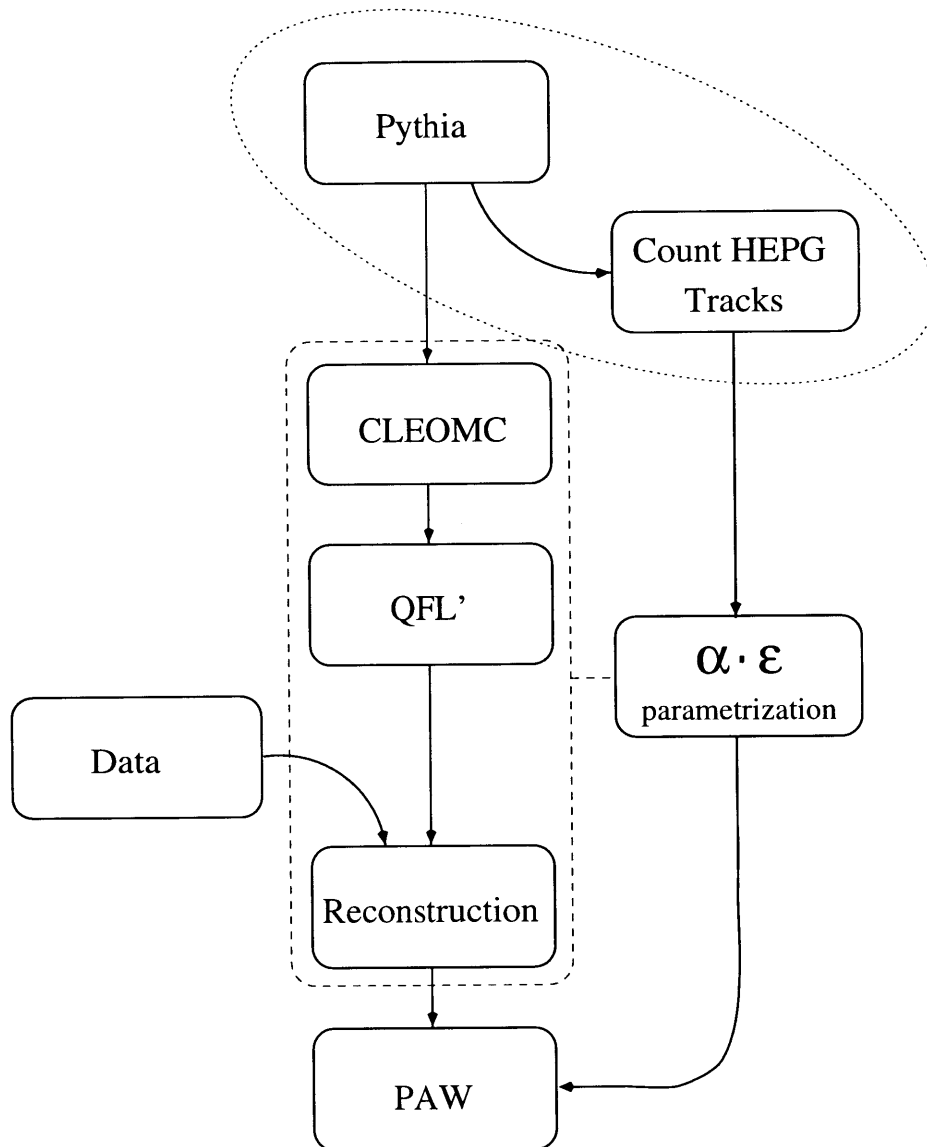
Figure A-6: Structure of the Monte Carlo generator. The dotted ellipse is the "fast" generator we use to test changes in distributions as we vary parameters; the code in the dashed box is replaced by a crude $\alpha \cdot \epsilon$ parametrization for this purpose.

inclusive particle p_T spectra. One expects that increasing the value of this parameter would result in production harder tracks. First we identify a B, remove all its decay products from the HEPG bank, and count all the tracks in the far region whose transverse momentum falls in one of the four p_T ranges shown in figure A-7. Then we plot the number of tracks found as a function of that parameter in those four p_T bins, fit polynomials to those distributions, and divide them by the respective counts seen in the data. The feature we are looking for is an intersection of all four fits, which would indicate good agreement between data and Monte Carlo in all p_T ranges.

While crude, this procedure is very efficient in pointing to the direction in which things move for every change in the (very large!) set of PYTHIA parameters. Needless to say, the procedure is iterative and very time consuming.

A.2.4 Scan Through Pythia Parameters

The following table lists the parameters we varied, and their effect on the properties of tracks around B mesons:

Parameter	Default setting	Range tested	Comment
CKIN(3,5)	none	5–15	$\min(\hat{p}_T)$ of the primary hard scattering; negligible effect on underlying event; b jet properties depend mostly on the final p_T^B distribution after trigger
MSTP(82)	1	0–4	model for multiple interactions; changes mostly MI cross-section, small effect on individual track properties
PARP(81)	1.40	1.20–5.10	$\min(\hat{p}_T)$ cutoff for MI (model-dependent);
PARP(82)	1.55	1.35–5.25	only affects tracks that are below the cutoff value
PARP(31)	1.50	0.90–3.00	K factor for cross-sections; multiplicative factor for all
MSTP(33)	0	0, 1	used cross-sections, useful for tuning underlying event

MSTP(2)	1	1, 2	α_s calculated to this order; affects every strong interaction in the event; changes MI cross-section; hardly any effect on final track p_T spectrum
PARP(62)	1.0	1.0–2.0	minimal Q for evolution of space-like parton showers; negligible effect
PARJ(82)	1.0	1.0–2.0	$\min(m)$ for parton showers, below which partons do not radiate; negligible effect
PARP(67)	4.0	4.0–8.0	maximum parton virtuality in space-like showers; increases multiplicity of high-p_T tracks ($> 2\,\mathrm{GeV}$) by $\approx 20\%$, little effect at low p_T
PARP(71)	4.0	4.0–8.0	maximum parton virtuality in time-like showers; negligible effect
PARP(91)	0.44	0.44–1.0	width of the Gaussian primordial k_T distribution of partons inside a proton; negligible effect
PARP(85)	0.33	0.1–1.0	probability that a multiple interaction gives two gluons with color connections to nearest neighbors in momentum space; high values give 30% fewer tracks below 0.6 GeV, negligible effect on high-p_T tracks
PARP(86)	0.66	0.1–1.0	probability that a multiple interaction gives two gluons as opposed to two quarks; lower values produce harder track p_T spectrum, $< 10\%$ effect on total multiplicity
PARJ(21)	0.36	0.10–1.90	fragmentation p_T width—$\sigma_{p_T}^{frag}$; dramatic effect on p_T spectrum of all particles produced by string fragmentation

163

Of all the tested parameters, the one that has the biggest effect on the properties of underlying event tracks is PARJ(21), the already mentioned "fragmentation p_T width" ($\sigma_{p_T}^{frag}$). Particles produced in the breakup of a color string are assigned transverse momenta relative to the string direction with a Gaussian distribution; $\sigma_{p_T}^{frag}$ is the width of that distribution. This is a fundamental parameter of the string fragmentation model, and does not depend on the masses or momenta of the string endpoints. The default value of 360 MeV was chosen on the basis of LEP measurements. More recent LEP results [48, 49] show that slightly higher values (around 400 MeV) give a better agreement with the LEP data (the best value depends on other settings, like Λ_{QCD}).

Figure A-7 shows the effect of $\sigma_{p_T}^{frag}$ on the track p_T distribution in the far region after several rounds of tuning along with other parameters described below. The plot indicates remarkably good agreement with the data at the value $\sigma_{p_T}^{frag} \approx 600$ MeV. Figure A-8 quantifies the agreement by taking into account the statistical errors on the data values. The tuned value of $\sigma_{p_T}^{frag}$ determined in this way is shown if table A.3.1.

The same procedure for another parameter, the cross-section multiplication factor for multiple interactions (double-parton scattering) is shown in figures A-9 and A-10.

A.2.5 The Near Region

We can now turn our attention to the near region. The track multiplicity of the B jet is directly affected by the energy available for creating fragmentation tracks, which is related to the shape of the longitudinal fragmentation function (Peterson *et al.*), which is in turn controlled by one parameter—ϵ_B. The change in the multiplicity of wrong-sign tracks in the cone of $\Delta R < 0.6$ around the B axis as a function of ϵ_B is plotted in in figure A-11 with the tuned underlying event settings. The data count is again corrected for the total acceptance and efficiency for reconstructing generated particles (this correction is different from the one for the far region; tracks near a reconstructed B are more likely to be fiducial). Note that here we only look at the total wrong-sign count; the momentum distribution of hadronization tracks is

164

Complex MI, Connected Gluons, Varying σ_{pt}^{frag}
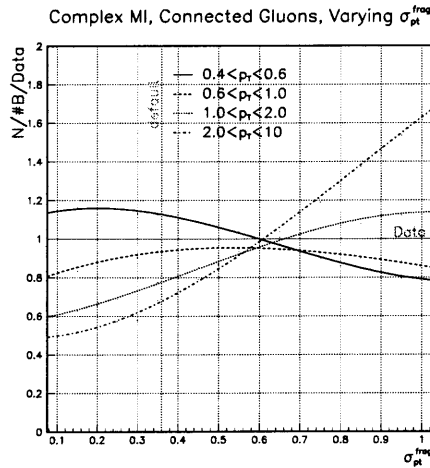
Figure A-7: The track multiplicity in the far region as a function of the fragmentation p_T width. The Monte Carlo shown in this plot includes multiple interactions which consist solely of color-connected gluon pairs. The cross-section for multiple interactions is 1.69 times the default value, and the model takes into account the structure of the proton. The shape of the generated p_T spectrum and the total multiplicity agree very well with the ones observed in the data for $\sigma_{p_T}^{frag} \approx 600\,\mathrm{MeV}$.
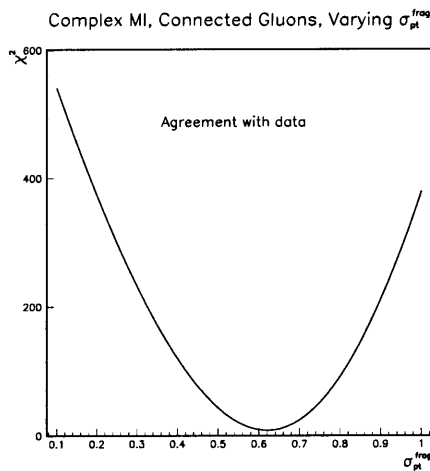
Complex MI, Connected Gluons, Varying σ_{pt}^{frag}

Figure A-8: χ^2 of the agreement with the data for the Monte Carlo runs shown in the previous figure. The total χ^2 is the sum of the χ^2 values for each of the four p_T ranges.

Complex MI, Connected Gluons, σ_{pt}=0.6, Varying σ_M

Data

— total track multiplicity in the far region (fit to MC)

$\sigma_M/\sigma_M^{default}$
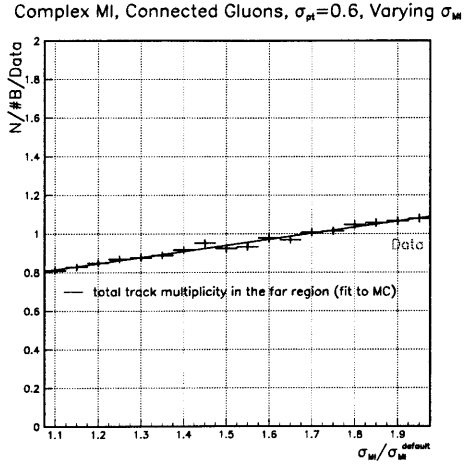
Figure A-9: The total track multiplicity in the far region as a function of the cross-section of multiple interactions.
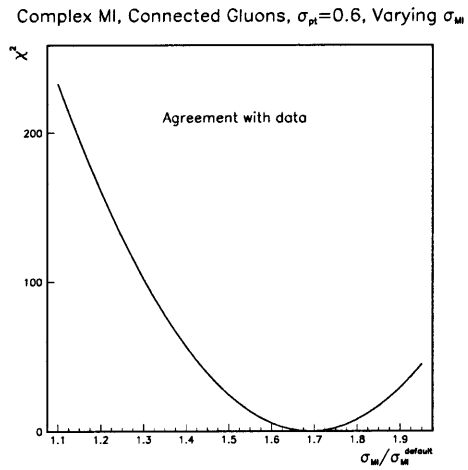
Complex MI, Connected Gluons, σ_{pt}=0.6, Varying σ_M

Agreement with data

$\sigma_M/\sigma_M^{default}$

Figure A-10: χ^2 of the agreement with the data for the Monte Carlo runs shown in the previous figure.

controlled by the same parameters that control the underlying event, so we do not attempt to tune it separately for the hadronization.

We measure an optimal value for ϵ_B from figure A-12, which shows the agreement with the data calculated in the way similar to figures A-8 and A-10.

We then generate a large Monte Carlo sample with the full detector simulation using these settings, and proceed to compare the results.
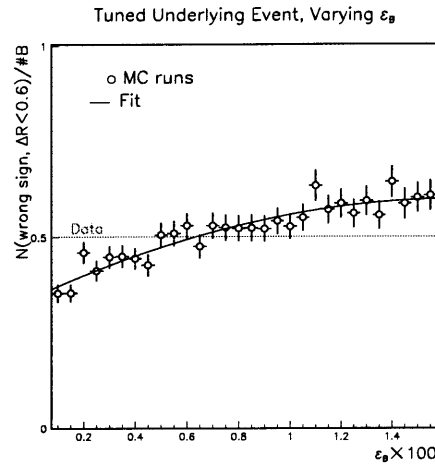
Figure A-11: The multiplicity of wrong sign tracks near the B meson as a function of ϵ_B for optimal values of parameters affecting underlying event. The intersection with the line marking the observed value determines our optimal value for ϵ_B.
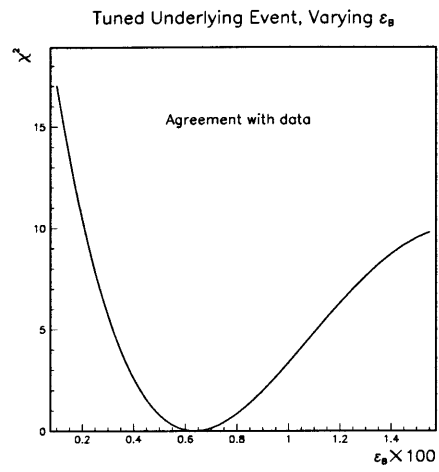
Tuned Underlying Event, Varying ε_B

Agreement with data

χ^2

$\varepsilon_B \times 100$

Figure A-12: χ^2 of the agreement with the data for the Monte Carlo runs shown in the previous figure.

A.3 The Result

Figures A-13, A-14, A-15, A-16 and A-17 show the comparison of dN/dΔR, dN/dΔφ, near and far p_T distributions, and multiplicities of tracks generated by PYTHIA with the default settings (dashed histograms), generated by PYTHIA with tuned settings (solid histograms), and observed in the data (points). The relevant settings used in generating the two Monte Carlo samples are:

Parameter	Default	Tuned	Comment
MSTP(61)	1	1	initial state radiation on
MSTP(71)	1	1	final state radiation on
MSTP(81)	1	1	multiple interactions on
MSTP(82)	1	3	model of multiple interactions
PARP(85)	0.33	1.0	fraction of color-connected gg multiple interactions
PARP(86)	0.66	1.0	total fraction of gg multiple interactions
MSTP(33)	0	1	multiply cross-sections by PARP(31)
PARP(31)	1.50	1.69	increase cross-sections by 69%
PARJ(21)	0.36	0.613	$\sigma_{p_T}^{frag}$
MSTJ(11)	4	3	use Peterson fragmentation for b, c
PARJ(55)	-0.005	-0.0063	$-\epsilon_b$

It is evident from the figures that the tuned PYTHIA reproduces the properties of prompt tracks in B events much better than the one with the default settings. Our main goal was to model accurately the background for charged pions from B^{**} decays, and that we have achieved: since the kinematic properties, multiplicity and topology with respect to the meson of background tracks closely match those seen in the data, we can use the dN/dQ distribution predicted by the Monte Carlo as a background estimate in our B^{**} search. This is illustrated in figure A-18, which shows the comparison of dN/dQ distribution between the data (points) and the two Monte

169

Carlo samples (the dashed histogram are the default settings, the solid are the tuned settings). The two Monte Carlo distributions shown in the figure do not include the B^{**} signal. As expected, the tuned Monte Carlo is in excellent agreement with the data in the $Q> 1\,\mathrm{GeV}$ region, unlike the one with default parameters. The excess seen in the data in the low-Q region is presumably the B^{**} signal.

A.3.1 Uncertainty on the Tuned Parameters

Studies that rely on the tuned PYTHIA generator for a description of certain properties of B events could potentially suffer from large systematic effects caused by the uncertainty in the choice of the tuned parameters. To estimate this uncertainty, we have quantified the agreement between the data and the Monte Carlo by calculating

$$\chi^2 = \left(\frac{D - M}{\sigma_D}\right)^2 \tag{A.1}$$

where D is the track count observed in the data, σ_D is the statistical uncertainty on its value, and M is the Monte Carlo value. The statistical uncertainty on the data value is calculated as $\mathrm{RMS}/\sqrt{M}$, where M is the number of mesons in our sample (*i.e.* the number of uncorrelated "experiments"), and RMS is the square root of the variance of the quantity we are measuring (*i.e.* track count per event). When tuning the p_T spectrum, the total χ^2 is simply the sum of the χ^2 values for the four p_T bins.

The dependence of the χ^2 on the three parameters of interest is shown in figures A-8, A-10 and A-12. Table A.3.1 summarizes the parameters and their uncertainties. The quoted uncertainty is the variation that results in a χ^2 greater by one than the minimal value. We can use these variations to estimate the systematic errors on the results of the analyses relying on this Monte Carlo generator.

170

Parameter	Value	Uncertainty
PARJ(21)	0.613	0.020
PARP(31)	1.69	0.04
PARJ(55)	−0.0063	$^{-0.0018}_{+0.0015}$

Table A.1: The values of the tuned parameters that result in the best agreement with the data and their uncertainties.
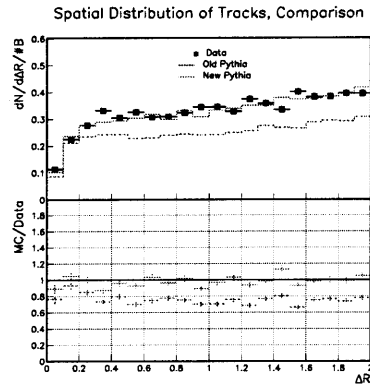
Figure A-13: Comparison between the tuned and the default Monte Carlo of the track multiplicity as a function of ΔR with respect to the B direction.
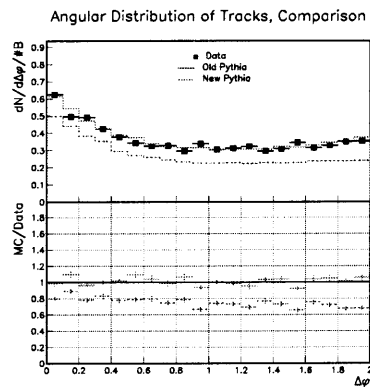
Figure A-14: Comparison between the tuned and the default Monte Carlo of the track multiplicity as a function of $\Delta\phi$ with respect to the B direction.
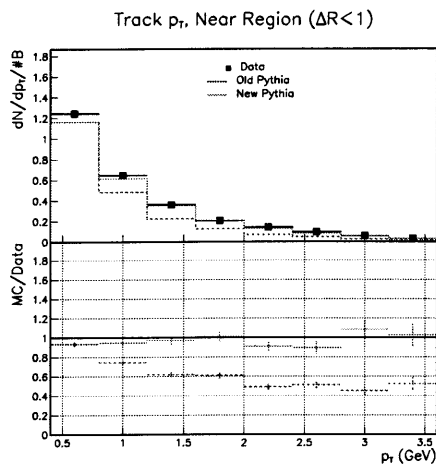
Figure A-15: Comparison between the tuned and the default Monte Carlo of the track p_T spectrum in the near region.
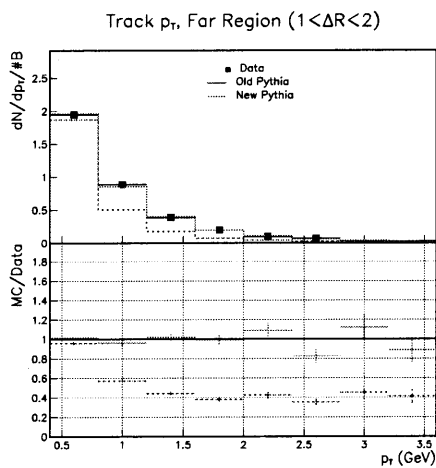
Figure A-16: Comparison between the tuned and the default Monte Carlo of the track p_T spectrum in the far region.
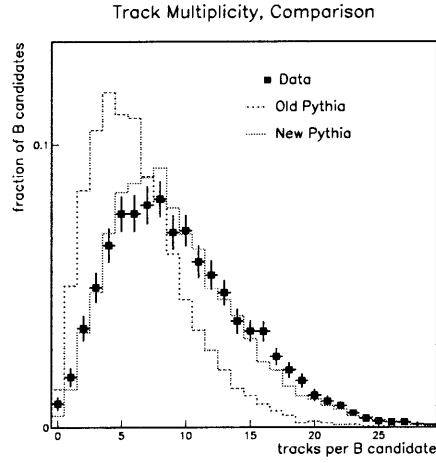
Figure A-17: Comparison between the tuned and the default Monte Carlo of the total multiplicity of tracks (near and far regions combined).
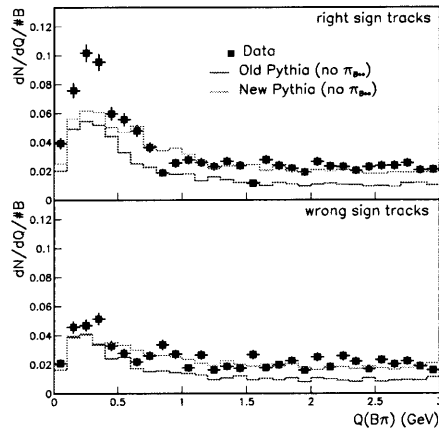
Figure A-18: Comparison between the tuned and the default Monte Carlo of the invariant mass distribution of tracks with the B meson.

174

A.4 Tuned Monte Carlo Parameters

Here is the complete PYTHIA talk_to used for generating the $b\bar{b}$ events with the tuned underlying event and hadronization tracks:

```
input module pythia
talk pythia
    run_number 13
    process
        set 5            ! b b=
        list
        return
    cut
        ckin 3 10.0      ! min pt_hat
        ckin 5 10.0      ! Minimum pt for 2->2 process. Used only
                         ! in the massless approximation.
                         ! The following four don't work for OS tagging:
        ckin 13 -1       ! min eta of max eta product
        ckin 14  1       ! max eta of max eta product
        ckin 15 -1       ! min eta of min eta product
        ckin 16  1       ! max eta of min eta product
        show
        return
    pythia_par
        mstp 61 1        ! initial state radiation on
        mstp 71 1        ! final state radiation on
        mstp 81 1        ! multiple interactions on
        mstp 82 3        ! model for multiple interactions
        parp 85 1.00     ! fraction of gg MI connected to nearest neighbors
        parp 86 1.00     ! fraction of MI that goes to gg
```

```
    mstp 33 1        ! multiply cross-sections by PARP(31)

    parp 31 1.69     ! myltiply cross-sections by this

    list mstp parp return

    return

jetset_par

    parj 21 0.613    ! fragmentation p_T width

    mstj 11 3        ! use Peterson fragmention for b, Lund for light q's

    parj 55 -0.0063 ! Peterson fragmentation parameter for b

    list mstj parj return

    return

genp

    genp_switch on   ! Convert HEPEVT to GENP

    return

jetset              !   B(2P) states

    parj 13 0.7625

    parj 14 0.32

    parj 15 0.033

    parj 16 0.099

    parj 17 0.165

    return

jetset

    particle

        mass 10513 5.76 width 10513 0.020 max_mass_dev 10513 0.05

        mass 10511 5.65 width 10511 0.100 max_mass_dev 10511 0.20

        mass 20513 5.65 width 20513 0.100 max_mass_dev 20513 0.20

        mass   515 5.77 width   515 0.024 max_mass_dev   515 0.05

        mass 10523 5.76 width 10523 0.020 max_mass_dev 10523 0.05

        mass 10521 5.65 width 10521 0.100 max_mass_dev 10521 0.20

        mass 20523 5.65 width 20523 0.100 max_mass_dev 20523 0.20
```

```
        mass    525 5.77 width    525 0.024 max_mass_dev    525 0.05

        return

    return

return
```

Appendix B

Event Selection Cuts

B.1 Cuts Common to All Signatures

The following requirements are common to all decay signatures:

- All tracks have SVX information.

- All tracks originate at less than 5 cm in z away from the lepton.

- The D vertex fit probability greater than 1%.

- $L_{xy}^D / \sigma(L_{xy}^D) > 1$.

- For the B signal, K and ℓ have the same charge.

- The invariant mass of $\ell D^{(*)}$ less than $M(B)$.

B.2 Signature-Specific Cuts

$\bar{D}^0 \to K^+ \pi^-$ Signature

- The K and π candidates have the opposite charge.

- The impact parameter significance of the K and π candidates greater than 3.

- D^* veto (reject candidates with $|\mathrm{m}(K\pi\pi_s) - \mathrm{m}(K\pi) - \Delta_\mathrm{m}(D, D^*)| < 3\,\mathrm{MeV}$).

- The D decay length significance greater than 3.

- The L_{xy} between the B and D vertices from $-0.5\,mm$ to $1\,mm$.

- $\mathrm{p}_\mathrm{T}^D > 2\,\mathrm{GeV}$.

- $\mathrm{p}_\mathrm{T}^K > 700\,\mathrm{MeV}$, $\mathrm{p}_\mathrm{T}^\pi > 500\,\mathrm{MeV}$.

- The invariant mass of the D decay products:

  - signal from 1.850 to 1.880 GeV,

  - sidebands from 1.800 to 1.830 GeV and from 1.900 to 1.930 GeV.

There are 3141 candidates including a predicted background of 473 ± 22.

$\bar{D}^0 \to K^+\pi^-\pi^+\pi^-$ Signature

- The K and one π candidate have the same charge.

- At least one $\pi^+\pi^-$ pair is compatible with a ρ^0: $0.6178 < m(\pi^+\pi^-) < 0.9192$.

- D^* veto (reject candidates with $|\mathrm{m}(K3\pi\pi_s) - \mathrm{m}(K3\pi) - \Delta_\mathrm{m}(D, D^*)| < 3\,\mathrm{MeV}$).

- The D decay length significance greater than 3.

- The L_{xy} between the B and D vertices from $-0.5\,mm$ to $1\,mm$.

- The χ^2 of the B vertex fit less than 20.

- $\mathrm{p}_\mathrm{T}^D > 3\,\mathrm{GeV}$.

- $\mathrm{p}_\mathrm{T}^K > 800\,\mathrm{MeV}$, $\mathrm{p}_\mathrm{T}^\pi > 600\,\mathrm{MeV}$.

- The invariant mass of the D decay products:

  - signal from 1.850 to 1.880 GeV,

− sidebands from 1.800 to 1.830 GeV and from 1.900 to 1.930 GeV.

There are 3404 candidates including a predicted background of 1870 ± 43.

$D^- \to K^+\pi^-\pi^-$ Signature

- The K and π candidates have the opposite charge.

- The impact parameter significance of the K and π candidates greater than 4.

- The χ^2 of the B vertex fit less than 20.

- $p_T^D > 3$ GeV.

- The invariant mass of the D decay products:

    − signal from 1.855 to 1.885 GeV,

    − sidebands from 1.805 to 1.835 GeV and from 1.905 to 1.935 GeV.

There are 2275 candidates including a predicted background of 821 ± 29.

$D^{*-} \to \bar{D}^0\pi_s^-$, $\bar{D}^0 \to K^+\pi^-$ Signature

- The K and π candidates have the opposite charge.

- The K and π_s candidates have the opposite charge.

- $|\text{m}(K\pi\pi_s) - \text{m}(K\pi) - \Delta_{\text{m}}(D, D^*)| < 3$ MeV.

- The χ^2 of the B vertex fit less than 60.

- The L_{xy} between the B and D vertices from $-0.5\,mm$ to $1\,mm$.

- The invariant mass of the D decay products:

    − signal from 1.850 to 1.880 GeV,

    − sidebands from 1.800 to 1.830 GeV and from 1.900 to 1.930 GeV.

There are 891 candidates including a predicted background of 56 ± 7.

$D^{*-} \to \bar{D}^0 \pi_s^-$, $\bar{D}^0 \to K^+ \pi^- \pi^+ \pi^-$ Signature

- The K and one π candidate have the same charge.

- The K and π_s candidates have the opposite charge.

- The impact parameter significance of the K and π candidates greater than 1.

- $|\mathrm{m}(K 3\pi\pi_s) - \mathrm{m}(K3\pi) - \Delta_{\mathrm{m}}(D, D^*)| < 3\,\mathrm{MeV}$.

- The χ^2 of the B vertex fit less than 20.

- The invariant mass of the D decay products:

    - signal from 1.850 to 1.880 GeV,

    - sidebands from 1.800 to 1.830 GeV and from 1.900 to 1.930 GeV.

There are 618 candidates including a predicted background of 94 ± 10.

$D^{*-} \to \bar{D}^0 \pi_s^-$, $\bar{D}^0 \to K^+ \pi^- \pi^0$ Signature

- The K and π candidates have the opposite charge.

- The invariant mass of the visible D decay products from 1.3 GeV to 1.7 GeV.

- The impact parameter significance of the K and π candidates greater than 1.

- $\mathrm{p}_\mathrm{T}^K > 1\,\mathrm{GeV}$, $\mathrm{p}_\mathrm{T}^\pi > 800\,\mathrm{MeV}$.

- The χ^2 of the D vertex fit less than 10.

- The χ^2 of the B vertex fit less than 10.

- The D decay length significance greater than 1.

- The difference between the invariant masses of the visible D and D^* decay products:

    - signal from the threshold to 165 MeV,

– sideband from 175 to 205 MeV.

There are 4288 candidates including a predicted background of 1610 ± 40.

Appendix C

The m_{T} Correction

We have studied the possibility of calculating the momentum of the neutrino using all the available track information (i.e., the tracks and the vertices they form). Since the resolution in z of B vertex position measurement is much worse than the typical B decay length, we have narrowed the scope of the problem down to the two dimensions transverse to the beam axis. Obviously, the lack of useful z information forces us to make the approximation $\eta_{\ell D} \approx \eta_B$.

Figure C-1 shows a diagram of the momenta involved. The position of the ℓD vertex determines the initial direction of the B meson. After tilting the coordinate system so that the x axis coincides with the B direction, we get the following set of equations:

$$E_{\mathrm{T}}^{\nu 2} = p_x^{\nu 2} + p_y^{\mathrm{R} 2} \tag{C.1}$$

$$p_{\mathrm{T}}^{B} = p_x^{\mathrm{R}} + p_x^{\nu} \tag{C.2}$$

$$E_{\mathrm{T}}^{B} = E_{\mathrm{T}}^{\mathrm{R}} + E_{\mathrm{T}}^{\nu} \tag{C.3}$$

$$E_{\mathrm{T}}^{B 2} = p_{\mathrm{T}}^{B 2} + m_{\mathrm{T}}^{B 2} \tag{C.4}$$

Where m_{T}^{B} is calculated from $\eta_{\ell D}$, and superscript R denotes all B decay products other than the neutrino. The solutions for p_{T}^{B} are

183
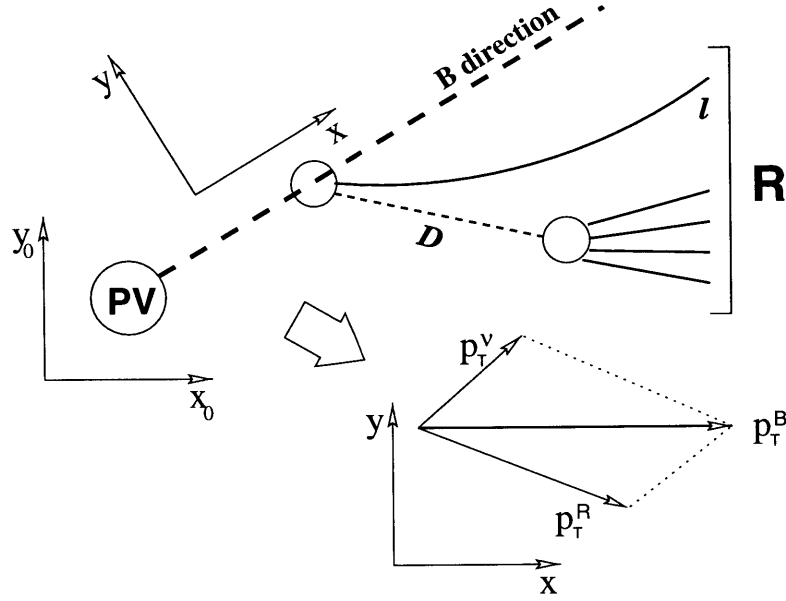
Figure C-1: A diagram of the momenta involved in m_T correction.

$$p_T^B = p_x^R + \frac{p_T^{R^2} p_x^R + E_T^{R^2} p_x^R - m_T^{B^2} p_x^R - 2p_x^{R^3} \pm E_T^R \Delta}{2(p_x^{R^2} - E_T^{R^2})}, \quad (C.5)$$

$$\Delta = \sqrt{p_T^{R^4} + m_T^{B^4} + E_T^{R^4} + 4p_x^{R^2} m_T^{B^2} - 2p_T^{R^2} m_T^{B^2} - 2E_T^{R^2} m_T^{B^2} - 2p_T^{R^2} E_T^{R^2}}. \quad (C.6)$$

Mathematically, these two solutions are on equal footing. In practice, the triger favors the lower-momentum solution by a large margin. This can be seen from the bottom plot in figure 3-7, where "$\beta\gamma_{++}$" shows the smaller p_T^B solution, and "$\beta\gamma_{--}$" the larger p_T^B solution. It is also apparent from the plots that the better solution doesn't correct the $\beta\gamma$ factor very well. It comes as a surprise, then, that the Q resolution for B^{**} candidates calculated in this way is much better than after just the previously described $\beta\gamma$ correction (see figure 3.4.3). The effect on the reconstructed B^{**} mass is shown in figure C-2.

Upon closer inspection we concluded that the reason for this behavior lies partly in correcting the B **direction** using the secondary vertex information, and partly in
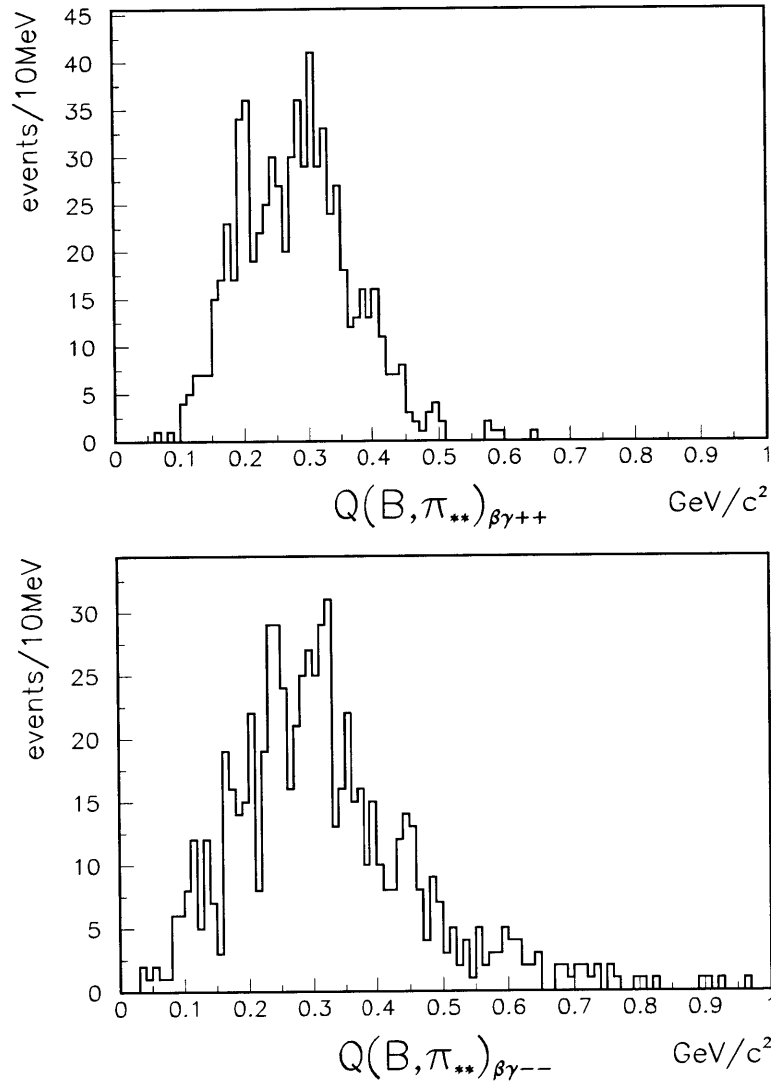
Figure C-2: Reconstructed B^{**} invariant mass after the m_T correction. The top (bottom) plot shows the lower (higher) p_T solution.

implicit cutting on the quality of the reconstruction of the B vertex position. The former is a kinematic property of the Q quantity: Q is a junction of the particles' momenta and the opening angle between them, so a large error in measuring the opening angle has a considerable effect on the Q resolution. The latter is a consequence of the fact that the vector passing through the secondary vertex sometimes doesn't intersect with the set of allowed solutions of the equations C.1 through C.4; it is also the reason we decided not to use this correction—rejecting all the candidates without a solution significantly decreases the size of our sample.

We also tried applying a suitable $\beta\gamma$ correction to the better solution of the m_T correction ("$\beta\gamma$b" in figure 3.4.3), but it didn't result in much additional improvement.

A correction analogous to the one described here but applied in three dimensions (using the accurate z information from the SVX replacement planned for the upcoming Run II for example) may be considerably more effective.

Appendix D

List of all B Decay Chains

In the discussion of sample composition in chapter 4 we use a numbering scheme to represent various B decay chains. This appendix explains the numbering scheme and explicitly lists all the decay chains we take into account in this analysis.

D.1   Numbering Scheme

To avoid explicitly writing out the complete decay chain from the B to the D meson, we use a more compact numbering scheme. Looking at figure 6-1, we see that that portion of the decay can consist of at most six particles: B, D^{**}, $\pi_{D^{**}}$, D^*, π_s and D. To uniquely determine the chain, we need to know only whether each of these particles existed, and, if so, whether it was charged or neutral. The number denoting a particular decay chain is therefore constructed by stringing together six digits, one for each particle in the above order, where a 0 means that the particle was not present, 1 that it was neutral, and 2 that it was charged. For example:[1]

- 100.002 means that there were a neutral B and a charged D, thus $B^0 \to D^-$;

- xxx.221 means that there were D^{*-}, π_s^-, $\bar{D}^0$, thus the channel involves $D^{*-} \to \bar{D}^0 \pi_s^-$;

---

[1]The dot in the middle serves to improve readability.

- xxx.202 means that there were D^{*-} and D^-, but *not* π^0; the only remaining possibility is a photon, so the channel involves $D^{*-} \to D^- \gamma$.

D.2 List of Chains

D^{*-} signatures:

- ### $\underline{B^0\ \text{contribution:}}$

  $B^0 \to \nu \ell^+ D^{*-}$ .... f^*

  [100.221]

  and

  $B^0 \to \nu \ell^+ D^{**-}$

  $D^{**-} \to D^{*-} \pi^0_{**}$ (didn't detect π^0_{**}) .... $f^{**} P_V(1/3)$

  [121.221]

- ### $\underline{B^+\ \text{contribution:}}$

  $B^+ \to \nu \ell^+ \bar{D}^{**0}$

  $\bar{D}^{**0} \to D^{*-} \pi^-_{**}$ (missed π^-_{**})

  (a fraction ξ_{D^*} of these has $\mathcal{D} = +1$) .... $f^{**} P_V(2/3)$

  [212.221]

D^- signature:

- ### $\underline{B^0\ \text{contribution:}}$

  $B^0 \to \nu \ell^+ D^-$ .... f

  [100.002]

  and

188

$B^0 \rightarrow \nu \ell^+ D^{*-}$

$D^{*-} \rightarrow D^- \gamma$ (didn't detect γ) .... $f^*\mathrm{BR}(D^{*-} \rightarrow D^- \gamma)$

[100.202]

and

$B^0 \rightarrow \nu \ell^+ D^{*-}$

$D^{*-} \rightarrow D^- \pi_s^0$ (didn't detect π_s^0) .... $f^*\mathrm{BR}(D^{*-} \rightarrow D^- \pi^0)$

[100.212]

and

$B^0 \rightarrow \nu \ell^+ D^{**-}$

$D^{**-} \rightarrow D^{*-} \pi_{**}^0$(didn't detect π_{**}^0)

$D^{*-} \rightarrow D^- \gamma$ (didn't detect γ) .... $f^{**}P_V(1/3)\mathrm{BR}(D^{*-} \rightarrow D^- \gamma)$

[121.202]

and

$B^0 \rightarrow \nu \ell^+ D^{**-}$

$D^{**-} \rightarrow D^{*-} \pi_{**}^0$(didn't detect π_{**}^0)

$D^{*-} \rightarrow D^- \pi_s^0$ (didn't detect π_s^0) .... $f^{**}P_V(1/3)\mathrm{BR}(D^{*-} \rightarrow D^- \pi^0)$

[121.212]

and

$B^0 \rightarrow \nu \ell^+ D^{**-}$

$D^{**-} \rightarrow D^- \pi_{**}^0$ (didn't detect π_{**}^0) .... $f^{**}(1 - P_V)(1/3)$

[121.002]

189

- **B^+ contribution:**

  $B^+ \to \nu\ell^+ D^{\overline{**}0}$

  $D^{\overline{**}0} \to D^-\pi^-_{**}$ (missed π^-_{**})

  (a fraction ξ_{D^-} of these has $\mathcal{D} = +1$) .... $f^{**}(1 - P_V)(2/3)$

  [212.002]

  and

  $B^+ \to \nu\ell^+ D^{\overline{**}0}$

  $D^{\overline{**}0} \to D^{*-}\pi^-_{**}$ (missed π^-_{**})

  $D^{*-} \to D^-\gamma$ (didn't detect γ)

  (a fraction ξ_{D^-} of these has $\mathcal{D} = +1$) .... $f^{**}P_V(2/3)\mathrm{BR}(D^{*-} \to D^-\gamma)$

  [212.202]

  and

  $B^+ \to \nu\ell^+ D^{\overline{**}0}$

  $D^{\overline{**}0} \to D^{*-}\pi^-_{**}$ (missed π^-_{**})

  $D^{*-} \to D^-\pi^0_s$ (didn't detect π^0_s)

  (a fraction ξ_{D^-} of these has $\mathcal{D} = +1$) .... $f^{**}P_V(2/3)\mathrm{BR}(D^{*-} \to D^-\pi^0)$

  [212.212]

$\overline{D}^0$ signatures:

- **B^+ contribution:**

  $B^+ \to \nu\ell^+ \overline{D}^0$ .... f

  [200.001]

  and

190

$B^+ \rightarrow \nu \ell^+ \bar{D}^{*0}$

$\bar{D}^{*0} \rightarrow \bar{D}^0 \gamma$ (didn't detect γ) .... $f^* \text{BR}(\bar{D}^{*0} \rightarrow \bar{D}^0 \gamma)$

[200.101]

and

$B^+ \rightarrow \nu \ell^+ \bar{D}^{*0}$

$\bar{D}^{*0} \rightarrow \bar{D}^0 \pi_s^0$ (didn't detect π_s^0) .... $f^* \text{BR}(\bar{D}^{*0} \rightarrow \bar{D}^0 \pi^0)$

[200.111]

and

$B^+ \rightarrow \nu \ell^+ \bar{D}^{**0}$

$\bar{D}^{**0} \rightarrow \bar{D}^{*0} \pi_{**}^0$ (didn't detect π_{**}^0)

$\bar{D}^{*0} \rightarrow \bar{D}^0 \gamma$ (didn't detect γ) .... $f^{**} P_V (1/3) \text{BR}(\bar{D}^{*0} \rightarrow \bar{D}^0 \gamma)$

[211.101]

and

$B^+ \rightarrow \nu \ell^+ \bar{D}^{**0}$

$\bar{D}^{**0} \rightarrow \bar{D}^{*0} \pi_{**}^0$ (didn't detect π_{**}^0)

160 $\bar{D}^{*0} \rightarrow \bar{D}^0 \pi_s^0$ (didn't detect π_s^0) .... $f^{**} P_V (1/3) \text{BR}(\bar{D}^{*0} \rightarrow \bar{D}^0 \pi^0)$

[211.111]

and

$B^+ \rightarrow \nu \ell^+ \bar{D}^{**0}$

$\bar{D}^{**0} \rightarrow D^o \pi_{**}^0$ (didn't detect π_{**}^0) .... $f^{**} (1 - P_V)(1/3)$

[211.001]

and

191

$B^+ \to \nu\ell^+ D^{\overline{**}0}$

$D^{\overline{**}0} \to D^{*-}\pi_{**}^-$ (missed π_{**}^-)

$D^{*-} \to \bar{D}^0\pi_s^-$ (didn't reconstruct π_s^-)

(a fraction $\zeta_{\bar{D}^0}$ of these has $\mathcal{D} = -1$!)

.... $f^{**}P_V(2/3)\mathrm{BR}(D^{*-} \to \bar{D}^0\pi^-)(1 - \epsilon(\pi_s))$

[212.221]

- **B^0 contribution:**

$B^0 \to \nu\ell^+ D^{*-}$

$D^{*-} \to \bar{D}^0\pi_s^-$ (didn't reconstruct π_s^-)

.... $f^*\mathrm{BR}(D^{*-} \to \bar{D}^0\pi^-)(1 - \epsilon(\pi_s))$

[100.221]

and

$B^0 \to \nu\ell^+ D^{**-}$

$D^{**-} \to D^{*-}\pi_{**}^0$ (didn't detect π_{**}^0)

$D^{*-} \to \bar{D}^0\pi_s^-$ (didn't reconstruct π_s^-)

.... $f^{**}P_V(1/3)\mathrm{BR}(D^{*-} \to \bar{D}^0\pi^-)(1 - \epsilon(\pi_s))$

[121.221]

and

$B^0 \to \nu\ell^+ D^{**-}$

$D^{**-} \to \bar{D}^0\pi_{**}^-$ (missed π_{**}^-)

(a fraction $\xi_{\bar{D}^0}$ of these has $\mathcal{D} = +1$) .... $f^{**}(1 - P_V)(2/3)$

[122.001]

and

$B^0 \rightarrow \nu \ell^+ D^{**-}$

$D^{**-} \rightarrow \bar{D}^{*0} \pi_{**}^-$ (missed π_{**}^-)

$\bar{D}^{*0} \rightarrow \bar{D}^0 \gamma$ (didn't detect γ)

(a fraction $\xi_{\bar{D}^0}$ of these has $\mathcal{D} = +1$)

.... $f^{**} P_V (2/3) \mathrm{BR}(\bar{D}^{*0} \rightarrow \bar{D}^0 \gamma)$

[122.101]

and

$B^0 \rightarrow \nu \ell^+ D^{**-}$

$D^{**-} \rightarrow \bar{D}^{*0} \pi_{**}^-$ (missed π_{**}^-)

$\bar{D}^{*0} \rightarrow \bar{D}^0 \pi_s^0$ (didn't detect π_s^0)

(a fraction $\xi_{\bar{D}^0}$ of these has $\mathcal{D} = +1$)

.... $f^{**} P_V (2/3) \mathrm{BR}(\bar{D}^{*0} \rightarrow \bar{D}^0 \pi^0)$

[122.111]

Appendix E

Relative Charm Reconstruction Efficiencies

This appendix lists the relative charm reconstruction efficiencies calculated from the Monte Carlo for all the B decay chains we consider when calculating the sample composition. The word "relative" stems from the fact that the efficiencies are measured relative to the efficiency for reconstructing the direct decay chain, which is listed first for each signature.

decay chain	ϵ_{kl}^D
200.001	1.00 ± 0.03
200.101	1.55 ± 0.04
200.111	1.51 ± 0.04
211.001	0.83 ± 0.04
211.101	0.56 ± 0.04
211.111	0.59 ± 0.03
212.221	0.39 ± 0.05
100.221	1.41 ± 0.06
121.221	0.44 ± 0.07
122.001	0.87 ± 0.03
122.101	0.59 ± 0.03
122.111	0.57 ± 0.02

Table E.1: Relative charm reconstruction efficiencies for the decay signature $\ell^+ \bar{D}^0$, $\bar{D}^0 \to K\pi$.

decay chain	ϵ_{kl}^D
200.001	1.00 ± 0.04
200.101	1.32 ± 0.05
200.111	1.29 ± 0.04
211.001	0.83 ± 0.06
211.101	0.52 ± 0.05
211.111	0.58 ± 0.04
212.221	0.65 ± 0.09
100.221	0.46 ± 0.04
121.221	0.26 ± 0.08
122.001	0.93 ± 0.05
122.101	0.64 ± 0.04
122.111	0.66 ± 0.04

Table E.2: Relative charm reconstruction efficiencies for the decay signature $\ell^+ \bar{D}^0$, $\bar{D}^0 \to K\pi\pi\pi$.

decay chain	ϵ^D_{kl}
100.002	1.00 ± 0.04
100.202	1.57 ± 0.19
100.212	1.32 ± 0.05
121.002	0.85 ± 0.06
121.202	0.78 ± 0.32
121.212	0.61 ± 0.06
212.002	0.76 ± 0.04
212.202	0.19 ± 0.11
212.212	0.54 ± 0.04

Table E.3: Relative charm reconstruction efficiencies for the decay signature $\ell^+ D^-$, $D^- \to K\pi\pi$.

decay chain	ϵ^D_{kl}
100.221	1.00 ± 0.02
121.221	0.38 ± 0.02
212.221	0.37 ± 0.01

Table E.4: Relative charm reconstruction efficiencies for the decay signature $\ell^+ D^{*-}$, $D^{*-} \to \bar{D}^0 \pi_s$, $\bar{D}^0 \to K\pi$.

decay chain	ϵ^D_{kl}
100.221	1.00 ± 0.03
121.221	0.44 ± 0.03
212.221	0.41 ± 0.02

Table E.5: Relative charm reconstruction efficiencies for the decay signature $\ell^+ D^{*-}$, $D^{*-} \to \bar{D}^0 \pi_s$, $\bar{D}^0 \to K\pi\pi\pi$.

decay chain	ϵ^D_{kl}
100.221	1.00 ± 0.03
121.221	0.37 ± 0.03
212.221	0.44 ± 0.03

Table E.6: Relative charm reconstruction efficiencies for the decay signature $\ell^+ D^{*-}$, $D^{*-} \to \bar{D}^0 \pi_s$, $\bar{D}^0 \to K\pi\pi^0$.

Bibliography

[1] The immense theory we presently call the Standard Model is not the work of any single person, but rather the product of nearly a century of theoretical and experimental work by an army of scientists. The relativistic quantum theory of electromagnetic interaction was first developed in: P. A. M. Dirac, Proc. Roy. Soc. **A117**, 610 (1928), Proc. Roy. Soc. **133**, 60 (1931); the crucial concept of electroweak unification in: S. Glashow, Nucl. Phys. **22**, 579 (1961); S. Weinberg, Phys. Rev. Lett. **19**, 1264 (1967); A. Salam, *Elementary Particle Theory*, ed. N. Svartholm (Almquist and Wiksells, Stockholm, 1969), p. 367; the unification with the strong interaction in: H. Fritzsch, M. Gell-Mann and H. Leutwyler, Phys. Lett. **B47**, 365 (1973); D. J. Gross and F. Wilczek, Phys. Rev. **D8**, 3633 (1973); S. Weinberg, Phys. Rev. Lett. **31**, 494 (1973); the formalism of inter-generational mixing in: N. Cabibbo, Phys. Rev. Lett. **10**, 531 (1963); M. Kobayashi and T. Maskawa, Progr. Theor. Phys. **49**, 652 (1973). A modern account with extensive references and historical notes can be found in D. Griffiths, *Introduction to Elementary Particles* (John Wiley & Sons, 1987); for a more in-depth treatment see for example: C. Itzykson and J. Zuber, *Quantum Field Theory* (McGraw-Hill, 1980); F. Halzen and A. D. Martin, *Quarks and Leptons* (John Wiley & Sons, 1984).

[2] N. Cabibbo, Phys. Rev. Lett. **10**, 531 (1963); M. Kobayashi and T. Maskawa, Progr. Theor. Phys. **49**, 652 (1973).

[3] L. Wolfenstein, Phys. Rev. Lett. **51**, 1915 (1983).

[4] M. Gell-Mann, A. Pais, Phys. Rev. **97**, 1387 (1955).

[5] E. E. Landé *et al.*, Phys. Rev. **103**, 1901 (1956).

[6] H. Albrecht *et al.* (ARGUS Collaboration), Phys. Rev. **D10**, 245 (1987).

[7] D. Buskulic *et al.* (ALEPH Collaboration), Phys. Lett. **B313**, 498 (1993).

[8] T. D. Lee and C. N. Yang, Phys. Rev. **104**, 254 (1956); C. S. Wu *et al.*, Phys. Rev. **105**, 1413 (1957).

[9] J. H. Christenson *et al.*, Phys. Rev. Lett. **13**, 138 (1964).

[10] A. Schopper, *Results from CPLEAR on Tests of CP, T, and CPT using K^0 and $\bar{K}^0$*, 2nd Internation Conference on B Physics and CP Violation, Honolulu, Hawaii, March 24–27, 1997.

[11] K. Ackerstaff *et al.*, CERN-EP-98-001 (1998), submitted to Phys. Lett. **B**, hep-ex/9801022.

[12] K. Kelley, Ph.D. dissertation, Massachusetts Institute of Technology, 1998 (unpublished).

[13] N. Isgur and M. B. Wise, Phys. Lett. **B232**, 113 (1989); Phys. Lett. **B237**, 527 (1990).

[14] E. Eichten, C. Hill, C. Quigg, "Properties of Orbitally Excited Heavy-Light Mesons," Phys. Rev. Lett. **71**, 25 (1993); "Orbitally Excited Heavy-Light Mesons Revisited," FERMILAB-CONF-94/118-T (1994).

[15] N. Isgur, "Spin-Orbit Inversion of Excited Heavy Quark Mesons," JLAB-THY-97-26.

[16] D. Ebert, V. O. Galkin, R. N. Faustov, "Mass spectrum of orbitally and radially excited heavy-light mesons in the relativistic quark model," hep-ph/9712318, HUB-EP-97/90 (1997), and references therein.

[17] Private correspondence with C. Quigg.

[18] ALEPH Collaboration, "Resonant Structure and Flavor-tagging in the $B\pi^\pm$ System Using Fully Reconstructed B Decays," contribution to the International Europhysics Conference on High Energy Physics, Brussels, Belgium (1995).

[19] DELPHI Collaboration, "Observation of Orbitally Excited B and B_s Mesons," DELPHI 95-105 PHYS 540 (1995).

[20] DELPHI Collaboration, "Observation of Orbitally Excited B Mesons," CERN-PPE/94-210 (1994).

[21] OPAL Collaboration, "Observations of π-B charge-flavor correlations and resonant $B\pi$ and BK production," CERN-PPE/94-206 (1994).

[22] D. Buskulic et al. (ALEPH Collaboration), Z. Phys. C73, 601 (1997); R. Anastassov et al. (CLEO Collaboration), hep-ex/9708035 (1997); P. Abreu et al. (DELPHI Collaboration), Phys. Lett. B345, 598 (1995).

[23] C. Peterson et al., Phys. Rev. D 27, 105 (1983).

[24] T. Sjöstrand, Int. J. Mod. Phys. A3, 751 (1988).

[25] B. Andersson, G. Gustafson, C. Peterson, Z. Physik C1, 105 (1979).

[26] F. Abe et al., FERMILAB-PUB-98-121-E (1998), hep-ex/9804014, submitted to Phys. Rev. D.

[27] F. Abe et al., Nucl. Inst. and Meth. Phys. Res., 271A, 387 (1988); FERMILAB-PUB-94/024-E, submitted to Nucl. Inst. and Meth. Phys. Res.; and references therein.

[28] S. van der Meer, "Stochastic Damping of Betatron Oscillations in the ISR," CERN/ISR-PO/72-31 (1994); F. Sacherer, "Stochastic Cooling Theory," CERN/ISR-TH/78-11 (1981).

[29] M. Mangano, P. Nason, G. Ridolfi, "Heavy-quark correlations in hadron collisions at next-to-leading order," Nucl. Phys. **B373**, 295–345 (1992).

[30] F. Abe *et al.*, Phys. Rev. Lett. **75**, 1451 (1995).

[31] F. Abe *et al.*, Phys. Rev. D **50**, 5550 (1994).

[32] Phys. Rev. **D54**, 1–720 (1996).

[33] T. Sjöstrand, Computer Physics Commun. **82** (1994) 74.

[34] P. Sphicas, "A $b\bar{b}$ Monte Carlo Generator," CDF Internal Note 2655 (1994).

[35] P. Nason, S. Dawson, R. K. Ellis, Nucl. Phys. **B 327**, 49 (1988).

[36] P. Avery, K. Read, G. Trahern, Cornell Internal Note CSN–212, March 25, 1985 (unpublished). We use code version 9.1.

[37] M. Shapiro *et al.*, "A User's Guide to QFL," CDF Internal Note 1810 (1992); A. Caner, "CDFSIM + QFL Simulation of the CDF Detector," CDF Internal Note 2177 (1993).

[38] R. Fulton *et al.*, Phys. Rev. **D43**, 651 (1991).

[39] F. DeJongh, "Lepton+Charm Data Sets," CDF Note 2935.

[40] P. Maksimovic, P. Sphicas, F. DeJongh, "Observation of $\pi - B$ meson Charge-flavor Correlations and Measurement of Time Dependent $B^0\bar{B}^0$ Mixing in $p\bar{p}$ Collisions," CDF Note 4106, and references therein.

[41] H. Keuteliann, "A Search for Resonant Structures in $B\pi$ systems," CDF Note 3641.

[42] M. Bailey, M. Gold, "Search for B^{**} Mesons," CDF Note 3299.

[43] K. Kelley, P. Sphicas, "Same-Side Tagging in Exclusive B Decays," CDF Note 3638.

[44] P. Sphicas, D. Vučinić, "On Using Pythia to Model Underlying Event in B and W Events," CDF Note 4097.

[45] F. Abe *et al.*, Phys. Rev. D **53**, 1051 (1996).

[46] C. Miao, J. Incandela, R. Snider, D. Stuart, M. Wang, W. Yao, "SVX′ Tracking Efficiency Study," CDF Note 2878.

[47] A. Warburton, "Run 1A and 1B Low-p_T Single- and Double-Track CTC Pattern Recognition Efficiencies," CDF Note 4139.

[48] See for example "Physics at LEP2," CERN 96–01 vol. 2 (1996), pages 125–133.

[49] The DELPHI Collaboration, "Tuning and Test of Fragmentation Models Based on Identified Particles and Precision Event Shape Data," CERN-PPE/96-120 (1996).